Low Gain Avalanche Detectors for Timing Applications in HADES

Low Gain Avalanche Detectors für Timingapplikationen in HADES

Master's thesis by Wilhelm Krüger
Date of submission: Dezember 08, 2020

1. Review: Prof. Dr. Tetyana Galatyuk
2. Review: Dr. Jerzy Pietraszko
Darmstadt

TECHNISCHE
UNIVERSITÄT
DARMSTADT

Physik
Institut für Kernphysik
AG Galatyuk

Eigenständigkeitserklärung

Hiermit versichere ich, die vorliegende Masterthesis ohne Hilfe Dritter nur mit den angegebenen Quellen und Hilfsmitteln angefertigt zu haben. Alle Stellen, die aus Quellen entnommen wurden, sind als solche kenntlich gemacht. Diese Arbeit hat in gleicher oder ähnlicher Form noch keiner Prüfungsbehörde vorgelegen.

Ort, Datum

Wilhelm Krüger

Contents

Abstract

In the HADES experiment a precise reaction time (T_0) determination is needed, in order to enable an optimal particle identification via time of flight measurements. Particle flux measurements and beam quality monitoring are necessary for the determination of reaction cross sections and ensuring stable detector operation and therefore efficient data taking. To fulfill these tasks, a timing precision below 50 ps, a position resolution better than 0.5 mm and low Z, to minimize nuclear reactions, are necessary.

Low Gain Avalanche Detectors (LGADs) are promising candidates to fulfill these requirements. In this document, an introduction to the LGAD technology will be given with a focus set on timing precision and radiation hardness. The timing precision reached with LGADs in experiments at COSY in Juelich, with a 1.92 GeV proton beam, and at SIS18 in Darmstadt, with a 2.5 GeV proton beam, with two different discriminator boards will be presented. The calibration procedure used to achieve the excellent timing precision will be described and small amplitude signals arising from capacitive coupling will be analyzed and discussed.

PaDiWa3 and PaDiWa4 boards were modified and tested in an experiment using a ^{90}Sr source, in order to improve the achievable timing precision of LGADs using PaDiWa discriminators. The modifications and resulting timing precisions as well as signal spectra will be presented.

Zusammenfassung

Um eine optimale Teilchenidentifikation über Flugzeitmessungen zu ermöglichen, ist eine präzise Reaktionszeit-Messung (T_0-Messung) notwendig. Desweiteren ist das Beobachten der Teilchenstrahl-Qualität und des Teilchenflusses notwendig, um zum einen Reaktionsquerschnitte zu bestimmen und zum anderen um zu verhindern, dass Spitzen in der Strahlintensität empfindliche Detektoren beschädigen. Dadurch kann eine effizientere Datenaufnahme sichergestellt werden. Um diese Aufgaben bewältigen zu können, sind eine Zeitauflösung von weniger als 50 ps und eine Positionsauflösung von weniger als 0.5 mm nötig. Desweiteren ist eine kleine Ladungszahl des Detektormaterials, um die Wahrscheinlichkeit von Kernreaktionen des Teilchenstrahls mit dem Detektormaterial so gering wie möglich zu halten, notwendig.

Low Gain Avalanche Detectors (LGADs) sind vielversprechende Anwärter, um diese Anforderungen zu erfüllen. In dieser Arbeit wird eine Einleitung in die Technologie von LGAD, mit einem Fokus auf Zeitauflösung und Strahlungsbeständigkeit, gegeben. Die Zeitauflösungen, die in einem Experiment am COSY in Jülich mit einem 1.92 GeV Protonenstrahl und in einem weiteren Experiment am SIS18 in Darmstadt mit LGADs, in Kombination mit verschiedenen Diskriminatortypen, erreicht wurden, werden präsentiert. Die Kalibrierung der aufgenommen Daten wird beschrieben und Signale mit kleinen Amplituden, von kapazitiver Kopplung zwischen den Auslesestreifen des Detektors stammend, werden analysiert und diskutiert.

PaDiWa3 und PaDiWa4 boards wurden modifiziert und in einem Experiment mit einer ^{90}Sr Quelle getestet, um die erreichbare Zeitauflösung von LGADs in Kombination mit PaDiWa-Diskriminatoren zu verbessern. Die Modifikationen sowie die erreichte Zeitauflösung als auch die Signalspektren werden präsentiert.

1 Introduction

The High Acceptance Di-Electron Spectrometer (HADES) [1] is operated at the SIS18, a heavy ion synchrotron with 18 Tm rigidity, at GSI Helmholzzentrum für Schwerionenforschung GmbH in Darmstadt, Germany. By measuring charged (and neutral) hadrons, leptons and photons, HADES investigates the microscopical properties of resonance matter formed in heavy ion collisions in the 1-2A GeV regime. Densities of the created matter in this type of collision reach up to $3 \cdot \rho_0$ with temperatures up to 80 MeV. Studying matter at these conditions could lead to a more fundamental understanding of the origin of matter in Supernovae and neutron star mergers [2].

Exploring the phase structure of strongly interacting matter in the baryon rich domain HADES lays a focus on the mechanisms of strangeness production, emissivity of resonance matter and the role of baryonic resonances herein [2]. Dileptons are emitted throughout the evolution of the fireball by the decay of virtual photons. As they do not interact strongly, dileptons are an ideal probe for the hot and dense matter [3]. At SIS18 energies, the production threshold of hadrons carrying strangeness lies mostly above the energy available in binary nucleon-nucleon collision. Therefore multi particle or multi step processes are required for strangeness production. These processes are enhanced in the dense medium and depend on in medium potentials [2, 4].

Important reference spectra to demonstrate true in medium effects are obtained by experiments using proton and secondary pion beams [4].

In the future HADES will continue its physics program at the SIS100, a heavy ion synchrotron with 100 Tm rigidity, at the Facility for Antiproton and Ion Research with the ultimate goal of providing a complete excitation function for (multi-)strangeness and dilepton production up to energies of 8A AGeV [5].

As Particle identification in HADES uses Time of Fight (TOF) information, a precise determination of the reaction time (T_0) is necessary. Particle flux measurements and beam quality monitoring are used for the determination of reaction cross sections and ensuring stable detector operation and therefore efficient data taking, respectively. The requirements for a T_0 detector used in upcoming experiments with proton and pion beams are therefore: an excellent timing precision with $\sigma_{T_0} < 60$ ps, a low material budget and low Z, to minimize the probability of nuclear reactions, a position resolution better than 0.5 mm and a detection probability for MIPs of close to 100% [6]. Additionally, the detector should be able to be operated in vacuum, have an active area of up to 8 cm^2 and have a high rate capability to be used in particle fluxes of J$>10^7$ p/(cm^{2}s) [6].

Although scCVD diamond detectors were successfully used as beam monitoring devices and T_0 detectors [7, 8], they are planned to be replaced by Low Gain Avalanche Detectors (LGAD) in the

scope of a T_0 detector upgrade. LGADs promise an excellent timing precision with $\sigma_{T_0}<50$ ps and great radiation hardness which is necessary for in beam operation. The precise position information can be achieved through fine segmentation.

2 HADES Experimental Set-Up

HADES is a fixed target experiment and consists of 6 identical sectors covering in total the full azimuthal angle and polar angles from 18° to 85°. The detectors making up the spectrometer, namely the Ring Imagig CHerenkov detector (RICH), the Mini Drift Chamber (MDC), the time-of-flight detectors, the Electromagnetic CALorimeter (ECAL) and the START detector, will be discussed in the following sections. A schematic overview of HADES is depicted in Fig. 2.1.
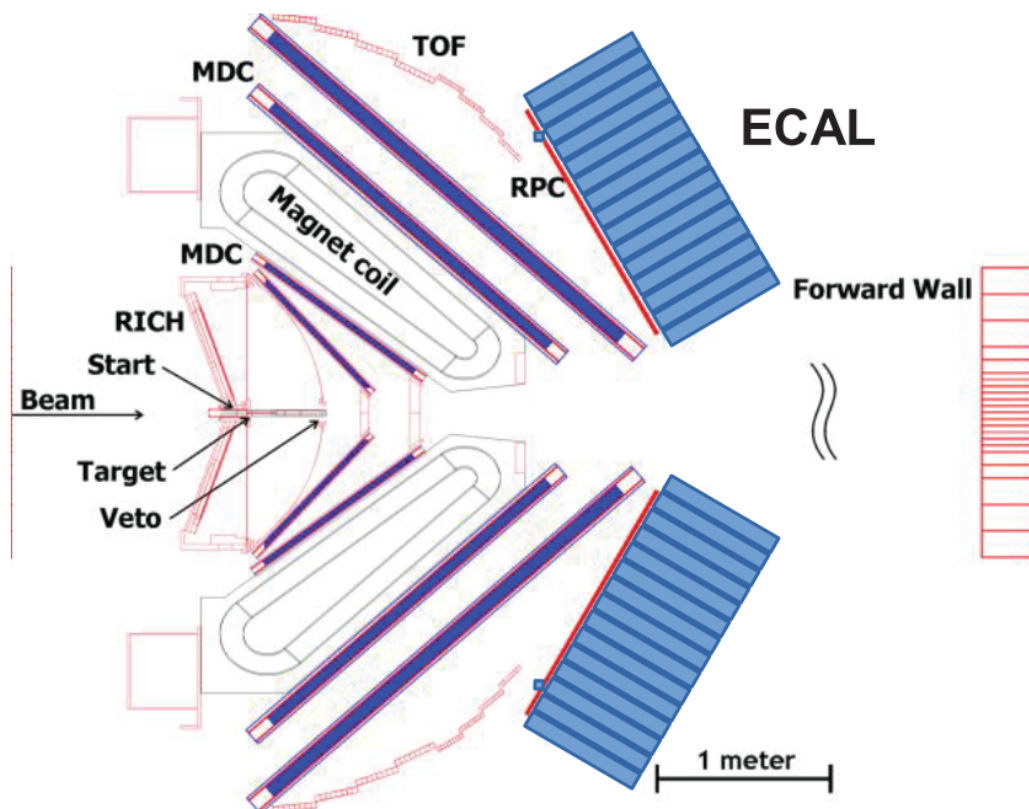

Figure 2.1: Schematic cross-sectional view of HADES with the important subdetectors. The beam enters the set-up from the left and goes through the Start detector before going through the target. Taken from [9].

2.1 Start and Veto Detector

In HADES two diamond based detectors are used. The first detector is located in front of the target and provides together with a T0 measurement a trigger signal. The other detector is located behind the target and provides a Veto signal to discard events where no interaction with the target took place.

A charged particle traversing the diamond material creates electron/hole pairs along its trajectory. These electrons and holes drift in the electric field, which is generated by applying a bias to the detector, to their respective electrodes and induce a signal in the metallized strips while doing so. The signal is then read out.

By measuring the hit time and hit position of particles important beam parameters such as the beam intensity, position during extraction and beam particle time structures [7] can be monitored. Timing precisions of about 117 ps for Minimum Ionizing Particles (MIP) [10] and 42 ps for a ^{197}Au beam at $1.25A$ GeV [11] have been reported.

Because of the complicated production process and limited sample size of detector grade diamond material a T0 detector upgrade is planned. The Low Gain Avalanche Detector (LGAD) technology is a promising new technology to be used as an upgrade. The working principle and properties of LGADs are described in a latter section.

Start Detector

The HADES Start detector (T0 detector) [7] is located 2 cm in front of the target. The T0 detector is made out of single crystal Chemical Vapor Deposited (scCVD) diamond material whose both surfaces are metallized with a 16 strip geometry with an active area of about $4.7{\times}4.7$ mm^2. The strips are 300 μm wide and are oriented vertically on one side and horizontally on the other side of the diamond material. A close up picture of the segmented T0 detector can be seen in Fig. 2.2 (a). To reduce the probability of nuclear reactions between the heavy ion beam and the T0 detector, a thickness of 70 μm was chosen. The segmentation of the detector surface as well as the orientation of the strips allows for a precise position measurement ($\sim$300 μm) simultaneous to a precise time measurement ($\sim$50 ps reached with a similar diamond detector) [11, 12].

2.1.1 Veto detector

The Veto detector [12] is a diamond based detector. It is made out of poly crystal Chemical Vapor Deposited (pcCVD) diamond material which is equipped with a box shaped matallization. The detector is positioned 70 cm behind the target. Using the Veto detector, events without any interaction with the target can be excluded from the HADES trigger generation. A close up picture of the veto detector can be seen in Fig. 2.2 (b).

2.1.2 Target

The target is positioned between the Start and Veto detectors. It is divided into 15 segments in order to reduce photon conversion. A picture of the Ag target used during the HADES Ag+Ag production beam time can be seen in Fig. 2.3.
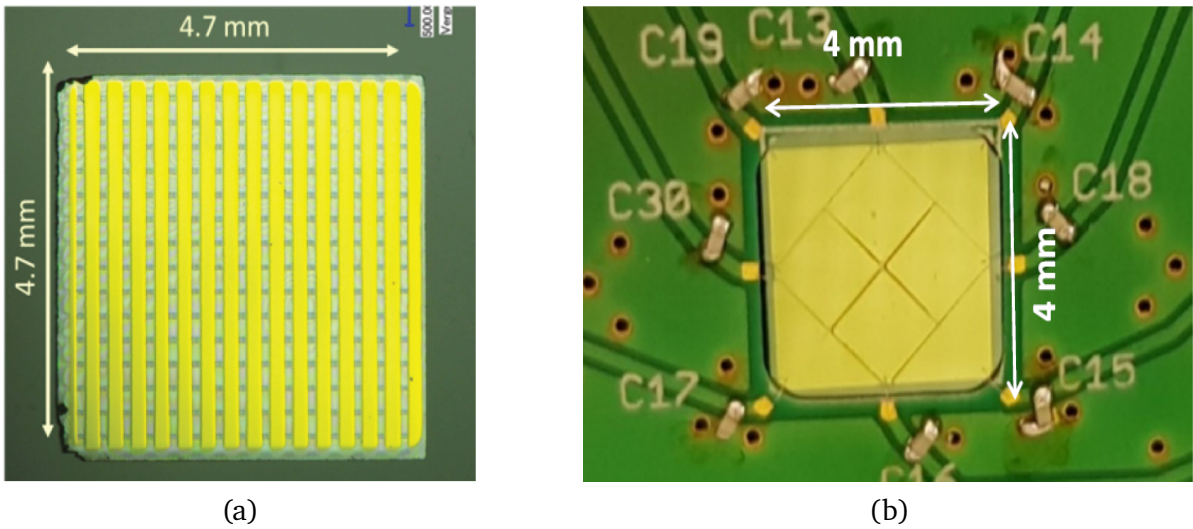

Figure 2.2: Close up photography of the T0 detector with 300 μm wide metallization strips on both sides (a). Taken from [7]. Close up photography of the Veto detector with a box shaped metallization (b). Taken from [12].
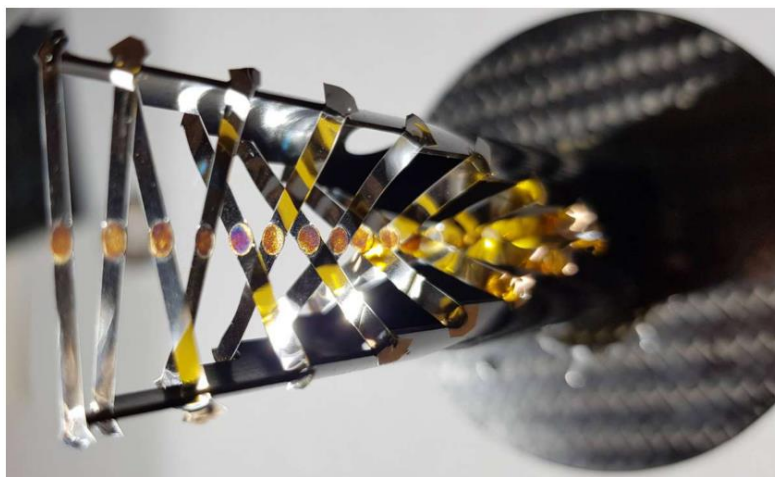

Figure 2.3: 15 times segmented silver target used during the HADES Ag+Ag production beam time in 2019. Taken from [12].

2.2 Ring Imaging Cherenkov Detector

The Ring Imaging CHerenkov (RICH) detector [13] exploits the Cherenkov effect to separate leptons from hadrons. Charged particles flying through the radiator medium, gaseous C_4F_{10}, with a velocity higher than the phase velocity of light in the medium emit photons, so called Cherenkov photons. These photons are emitted in a cone similar to a Mach cone which is created when the phase velocity of sound in a medium is surpassed.

A segmented spherical VUV-mirror, with a diameter of 145 cm and a curvature of 87 cm, reflects the photons onto a position sensitive photon detector. The photons impinge on the photon detection plane in circles of almost constant radius. A schematic view of the RICH detector can be seen in Fig. 2.4.

The threshold velocity in the gaseous C_4F_{10} is $\gamma_{thr} \approx 18$. While leptons with a momentum of 100 MeV$<$p$_{lepton}<$1500 MeV produce cherenkov photons, the velocity of hadrons in this momentum range is too low. This causes the RICH detector to be basically hadron blind. Designed for online lepton identification in the hadron rich environment of heavy ion collisions, RICH provides a second level trigger signal for the HADES set-up, which was not any longer used in recent beam times. By placing the RICH detector in the magnetic field free region close to the target, a compact design can be realized while sill covering the polar angles from 18°-85°. The photo detection plane was recently, in collaboration with the Compressed Baryonic Matter (CBM) experiment, replaced by PMTs in the scope of the FAIR phase 0 detector upgrade [14]. The upgraded RICH successfully operated during the last beam time in 2019 and showed factor of $\sim$10 improved performance in the electron detection efficiency, compared to the old photo detection plane.
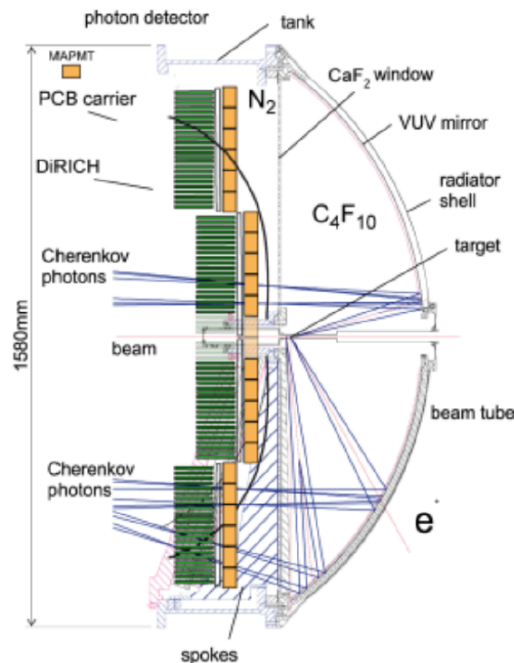

Figure 2.4: Schematic view of the upgraded RICH detector with the new PMTs. Taken from [14].

2.3 Mini Drift Chamber

Particle tracking in HADES is realized using a combination of Mini Drift Chambers (MDC) [15, 16] and a superconducting magnet. Four MDC planes are installed in each of the six sectors of HADES with two MDC planes placed in front of the magnet and two behind, as can be seen in Fig. 2.5 (a). Each MDC consists of six layers of field/sensing wires in different angular orientations ranging from -40° to +40° between a total of seven layers of cathode wires with a constant orientation of 90°. The different angular orientations of the field/sense wires are illustrated in Fig. 2.5 (b). The combination of sense, field and cathode wires form about 1100 drift cells per MDC. By increasing the active area of each drift cell from the outer to the inner MDCs, a constant granularity of the detectors is ensured. The definition of a drift cell is illustrated in Fig. 2.6 (a).

In normal operation, the chambers are filled with a gas mixture of $Ar:CO_2$ in a 70:30 ratio. While the field and cathode wires are kept at a negative potential, the sense wire is grounded.

Charged particles traversing the gas filled chamber ionize the gas along their trajectory and the resulting electrons drift to the closest sense wire. In the direct vicinity of the sense wire, the electric field is high enough to accelerate the electrons such that they carry sufficient energy to ionize the gas mixture and create secondary electrons and ions, producing an electron avalanche and thus a detectable signal. The movement of the primary electrons inside a drift cell is illustrated in Fig. 2.6 (b).

By measuring the arrival times of the signal, the position where the charged particle traversed the MDC can be reconstructed. To support particle identification, an energy loss information can be extracted by measuring the width (time over threshold) of the signals, which is a measure of the created number of primary electrons and thus of the energy lost by the ionizing particle.

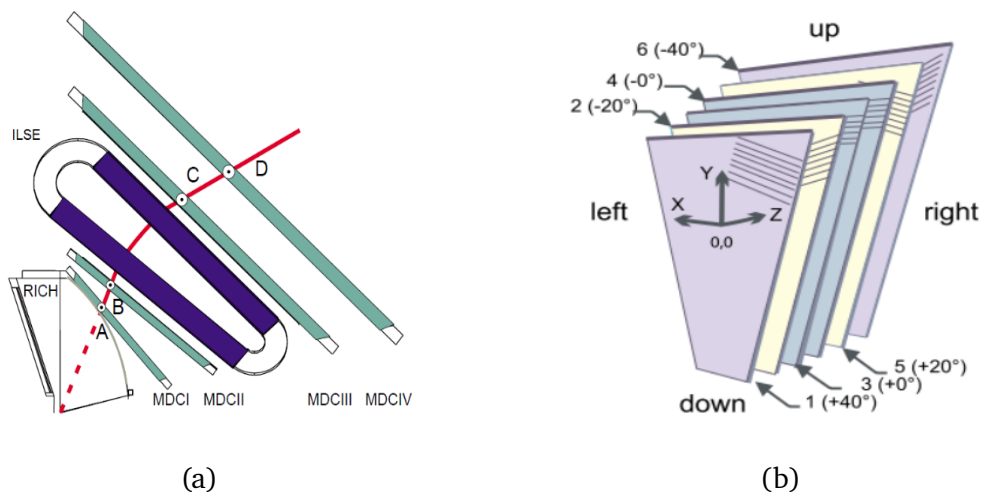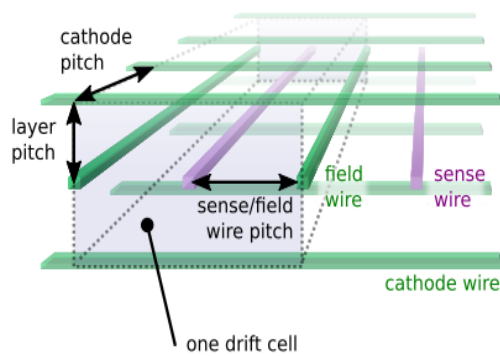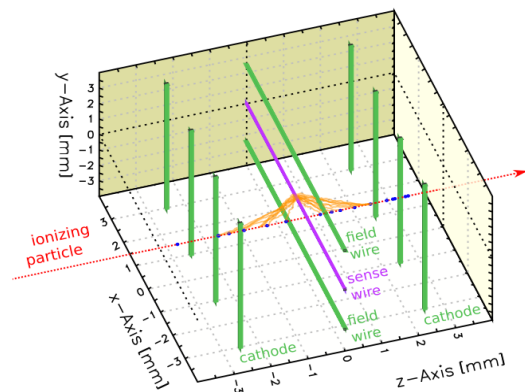(a)   (b)

Figure 2.5: Schematic view of the magnetic spectrometer used for tracking in HADES showing the two MDC planes in front and behind the superconducting magnet (ILSE) (a). Taken from [17]. Schematic view of the six layers of an MDC module showing the different angular orientation of the field/sensing wires (b). Taken from [1].

Figure 2.6: Schematic depiction of a drift cell formed by the cathode wires and field/sensing wires with a stereo angle of 0° (a). Schematic view of a drift cell showing the drift trajectory of primary electrons created by a traversing charged particle. Both Taken From [16].

2.4 Time of Flight Detectors

The time of flight measurement in HADES is realized by three detectors. The Start detector measures a T_0 which marks the start of the time of flight measurement. Two other detectors, the TOF and RPC detector, measure the needed second time for the time of flight measurement.

2.4.1 The RPC detector

Polar angles in the region of $12° < \theta < 45°$ are covered by the Resistive Place Chamber (RPC) detector [18]. Covering a total area of 8 m^2 with 1116 RPC modules, the RPC detector is divided into 6 sectors. Each sector consists of two partially overlapping layers with 31 rows and 3 columns of RPC modules with different lengths and widths.

An aluminum box is surrounding each RPC cell for shielding purposes. A cell itself consists of three aluminum electrodes and 2 glass electrodes (float glass) of 2 mm thickness with gaps of 270 μm in between them. The gap is filled with a gas mixture of $C_2H_2F_4$:SF_6 in the ratio of 90:10 [19]. While a high-voltage of around 6 kV is applied to the central aluminum electrode, the other two are grounded and the 2 glass electrodes are kept floating. Kapton insulation is used to insulate the electrodes from the shielding.

A charged particle traversing the detector ionizes the gas mixture and because of the applied high-voltage the primary electrons cause an electron avalanche and subsequently a discharge occurs. Due to the high resistivity of the electrode the electric field in the discharge region will be strongly

reduced thus limiting the discharge to a small region and keeping the other parts of the detectors operational [20].
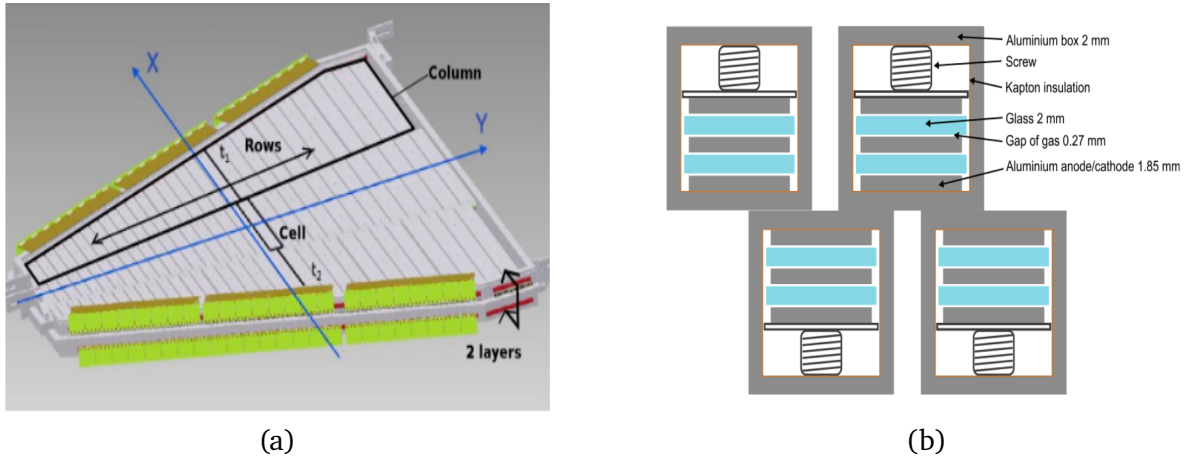

<div align="center">(a)   (b)</div>

Figure 2.7: Schematic view of an RPC module showing the two layers, three columns and 31 rows (a).
Cross-sectional view of RPC modules showing the most important components (b). Both Taken From [19].

2.4.2 The TOF detector

Polar angles in the region of $45°<\theta<88°$ are covered by the Time Of Flight (TOF) [21] wall. The TOF wall consists of a total of 384 scintillation rods, distributed among 6 sectors and 8 modules per sector. Each module consisting of 8 scintillator rods is packed in a carbon fiber case to increase mechanical stability with minimal additional thickness in terms of radiation length. The scintillator rods vary in length from 1 m to 2 m from the inner to the outer parts of detector, while the cross section is 2×2 cm^2 for the 192 innermost and 3×3 cm^2 for the 192 outermost rods. Two PhotoMulitplies Tubes (PMT) are connected via light guides which are bent in an angle of $67°$ to the rods on both ends.

A charged particle traversing a scintillation rod produces scintillation light which is guided to both ends of the rod to the PMTs. By combining the measurements at both PMTs the hit time and hit position can be reconstructed.

2.5 Electromagnetic Calorimeter

The Electromagnetic Calorimeter (ECAL) [12, 22] consists of 978 modules, distributed among six sectors and covers polar angles in the region of $16°<\theta<48°$. A technical drawing of ECAL is shown in Fig. 2.8 (a). Each module consists of a lead glass Cherenkov counter, a PhotoMultiplier Tube (PMT),

a high-voltage divider and an optical fiber encased in a brass case and weighs around 16 kg resulting in a total weight of about 15 t. The lead glass is borrowed from the OPAL [23] experiment and has a refraction index of $n=1.708$, a radiation length of 2.51 cm and dimensions of $92{\times}92{\times}420$ mm^3. An LED/Laser system is installed and enables monitoring and calibration applications for each individual module. A schematic view of an ECAL module without the brass case can be seen in Fig. 2.8 (b)

The measurement principle used it ECAL is based on a shower development inside the lead glass block. In the presence of a nucleus, highly energetic photons have a high chance to interact with the lead glass via pair production. Due to the pair production process, the energy of the highly energetic photon is converted into an e^+e^- pair which themselves are highly energetic. The produced electrons and positrons interact mainly via the Bremsstrahlung process and create additional highly energetic photons. This interplay of interactions creates an electromagnetic particle shower in the lead glass module and continues until the energies of the particles are too low and other interaction processes, such as Compton and photoelectric effects for photons and ionization processes for the electrons, dominate. An energy measurement is realized by using the Cherenkov effect. The created Cherenkov radiation is detected by the PMT and is proportional to the deposited energy inside the module. With the energy measurement for example, the electron/pion separation above p=400 MeV/c can be improved.

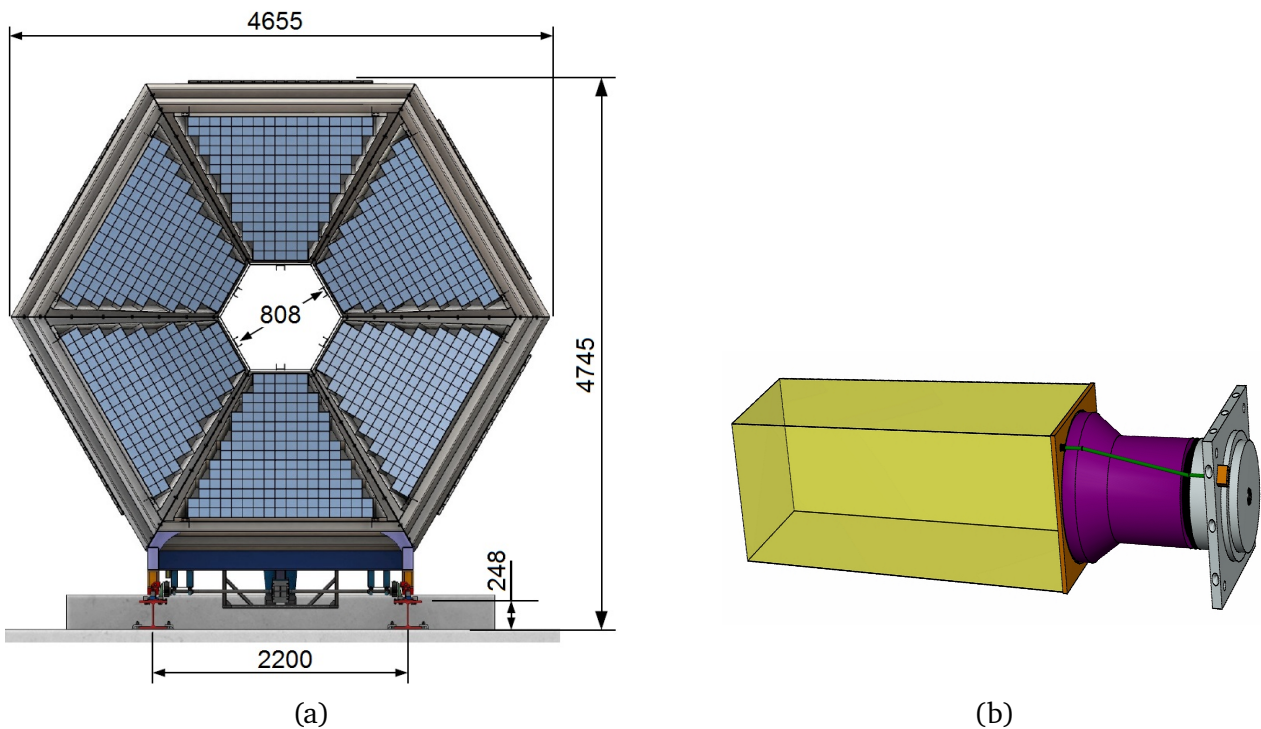(a)   (b)

Figure 2.8: Technical drawing of ECAL showing the front view (a). Taken from [22]. Schematic view of an ECAL module without the brass case showing the lead glass bloch (yellow), the PMT (magenta) and the optical fiber of the LED/laser system for test and calibration purposes (green) (a). Taken from [12].

3 Basics of Silicon based Particle Detectors

In this chapter, the working principle of silicon detectors will be introduced. For that reason, the basic properties of intrinsic semiconductors in general (and Si in particular), and the principle of p-n-junctions will be discussed As we are interested in measuring charged particles the interaction of charged particles with the Si bulk material will be discussed as well as the signal formation mechanism. After presenting some typical applications of silicon detectors the Low Gain Avalanche Detector (LGAD) technology will be introduced and discussed.

3.1 Intrinsic Semiconductors

The reason why metals are good and insulators bad conductors of electricity, lies in the fact that the energy levels of the valence and conduction band overlap in metals and are separated by a large gap in insulators. Semiconductors are a class of material which lies in between those two. The energy levels of the valence and conduction band do not overlap, as it would be the case with metals, but the band gap is smaller than it is the case with insulators. In fact, thermal excitation from the valence to the conduction band is possible.

Crystalline Si is an example of a semiconductor where Si atoms are arranged in a diamond lattice as is illustrated in Fig. 3.1. Due to the tetravalent nature of Si the lattice is formed such that each Si atom has 4 closest neighbors with which the Si atom forms covalent bonds as can be more clearly seen in a 2 dimensional sketch of the lattice, such as in Fig. 3.2. Due to the close spacing inside the crystal lattice the energy levels of the many Si atoms and their electrons form continuous bands. The energy levels of silicon atoms w.r.t the lattice spacing are illustrated in Fig.3.3. These energy bands, namely the conduction and the valence band, are separated by a gap of around 1.12 eV at room temperature (300 K). This gap is small enough for electrons to be thermally excited from the valence band into the conduction band and can conduct electricity. This results in a positively charged vacancy in the original place of the electron, a so called hole. This hole can be filled by an electron in the valence band of a neighboring atom, leaving a hole in that. The hole moved to the second atom. Electrons in the conduction band and holes in the valence band can be considered free particles in the lattice and can move around in the crystal lattice and conduct electricity. In a pure Si crystal, which is an intrinsic semiconductor, the density of electrons in the conduction band n and holes in the valence band p is around $n = p = n_i = 1.45 \cdot 10^{10} \ cm^{-3}$ and is called the intrinsic concentration [24]. In comparison, the amount of atoms in the lattice is around $5 \cdot 10^{22} \ cm^{-3}$. The intrinsic charge carrier concentration is too high to detect for example a minimum ionizing particle traversing the
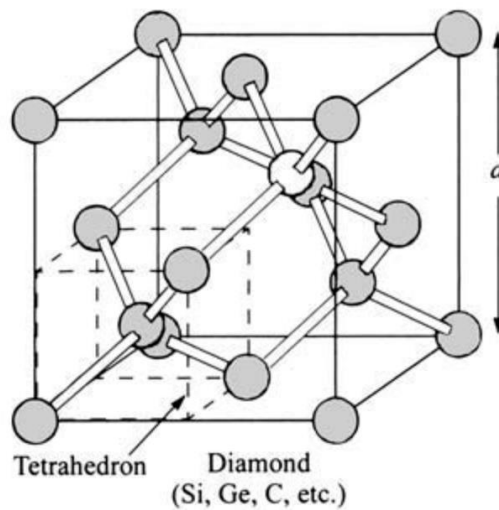
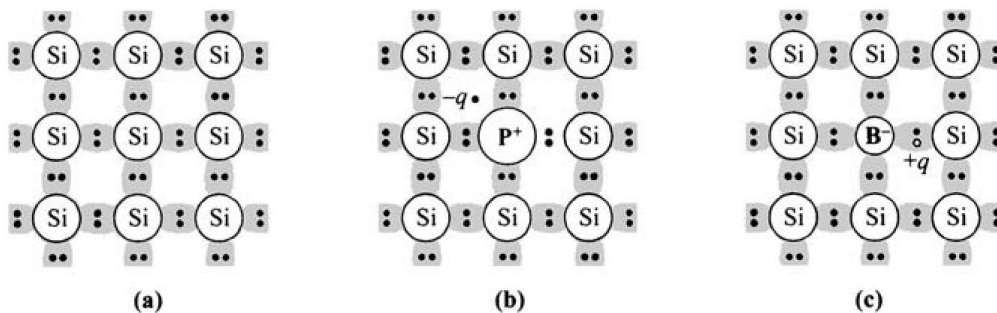Figure 3.1: Schematic view of a 3 dimensional diamond crystal lattice. Taken from [25].

Figure 3.2: Two dimensional diagram showing the covalent bonds between pure (left), with P n-doped (middle) and with B p-doped (right) silicon (a). Taken from [25].

detector creating on average $\approx$108 e/h pairs per μm of detector thickness. Modifications such as doping and formation of a p-n-junction have to be made. They will be described in the next sections.

3.1.1 Doping of Semiconductors

By introducing impurities into the semiconductor, the electrical properties can be modified. Penta- or trivalent atoms built into the diamond lattice act as electron donors or acceptors by introducing additional energy levels close to the conduction/valence band, as is illustrated in Fig 3.4. Pentavalent atoms (i.e. n-type dopants) such as As or Ti introduce additional energy levels close to the conduction band and the Fermi level shifts closer to the conduction band . Due to the pentavalent nature of the atoms it can still form four covalent bonds with the four neighboring Si atoms. The fifth electron ends up being weakly bound and is very likely to be thermally excited into the conduction band.

ELECTRON
ENERGY

CONDUCTION
BAND

E_g

VALENCE
BAND

5.43 Å   LATTICE SPACING

(a)

Si

6

5

4

3

2

1

0

−1

−2

−3

−4

Energy (eV)

E_C

E_g

E_V

L   [111]   Γ   [100]   X

Wave vector

(b)
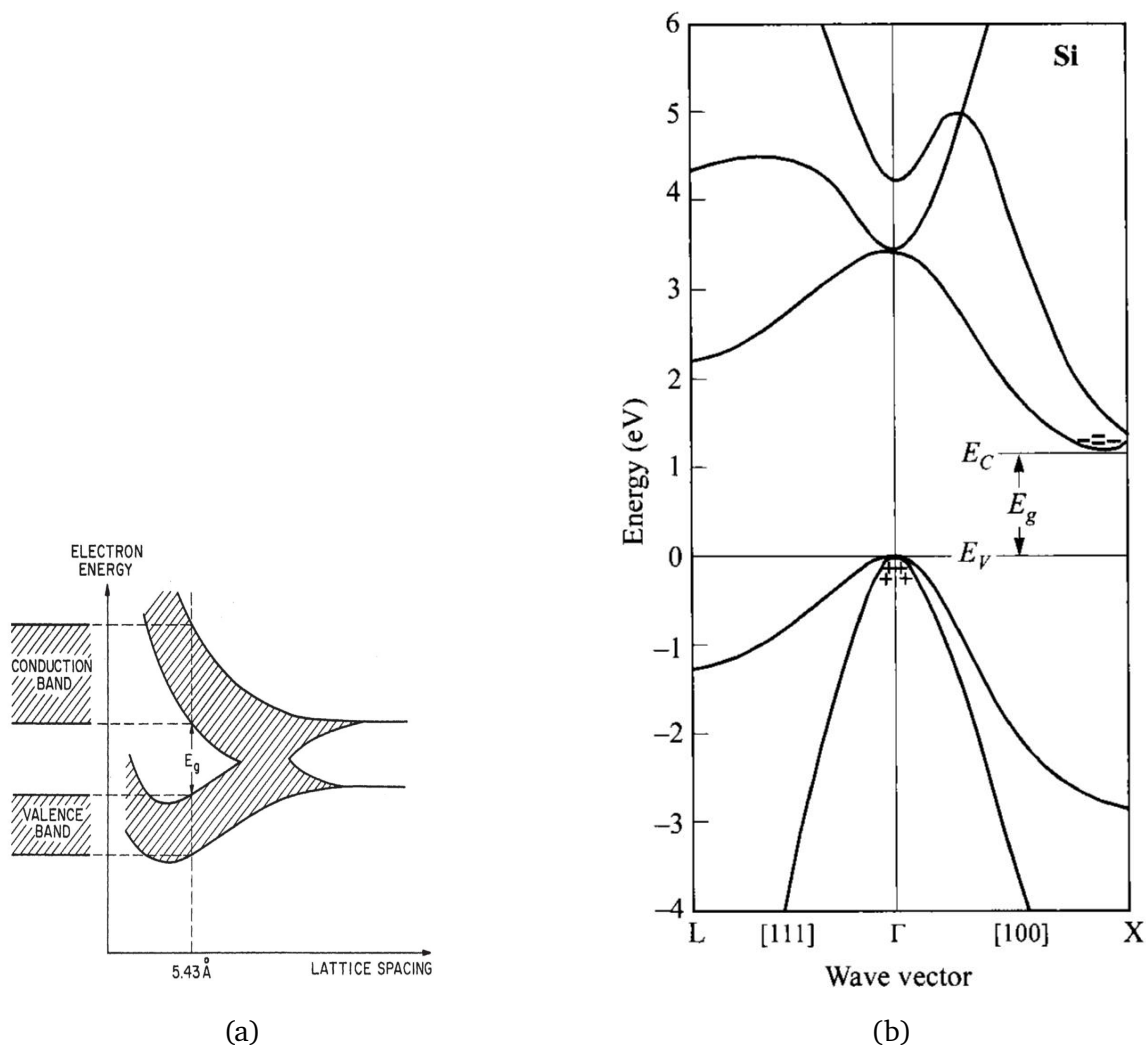
Figure 3.3: Evolution of energy levels of Si atoms w.r.t. lattice spacing showing the change from a discrete structure for large distances between the atoms to the band structure for the lattice spacing of a Si crystal (a). Taken from [26].
Energy band structure of a Si crystal with electrons indicated with "-" and holes indicated with "+" (b). Taken from [25].

Due to the excitation, the electron leaves a positive charge which position is fixed in the lattice. Thus two types of charges are created: a free charge, in form of the electron, and a stationary charge in form of the dopant atom.

Trivalent dopants (i.e. p-type dopants) act as electron acceptors by introducing additional states with energies close to the valence band and the Fermi level gets shifted towards the valence band. Electrons in the valence band can be easily thermally excited into these states thus creating a negative charged dopant atom and a positively charged hole. This hole can be treated as a free charge carrier that can conduct electricity in the valence band. Holes move around by electrons of neighboring Si atoms taking the place of the missing electron thus leaving behind a hole in a different place of the

Figure 3.4: By doping introduced additional energy levels in Si with the respective dopant. Taken from [24].

lattice.

Doped semiconductors are labeled as positively doped (p-doped) or negatively doped (n-doped) semiconductors depending on the sign of the majority of the mobile charge carriers. Typical doping concentrations lie in the range of $10^{12} - 10^{19}\ cm^{-3}$ [24]. At room temperature, it is safe to assume that approximately all dopant atoms are ionized and the carrier concentration is around the doping concentration, because the intrinsic carrier concentration gets dominated by the carrier concentration introduced with the doping.

3.1.2 P-N-Junction

The basic structure of a silicon particle detector is the so called p-n-junction. By bringing a p-doped and an n-doped semiconductor with different doping concentrations into contact, the electrons and holes start to diffuse and annihilate each other when they come into contact. During this process an electric field builds up caused by the stationary charges of the dopants. The annihilation goes on until the the electric potential difference created by the not compensated fixed charges prevents the diffusion of the free charge carriers. This (built-in)voltage can be expressed as[27]:

$$V_{built-in} \approx \frac{kT}{e} ln\left(\frac{N_D N_A}{n_i^2}\right) \tag{3.1}$$

with the Boltzmann constant k, the temperature T, the electron charge e, the concentration of acceptor and donor atoms N_A and N_D respectively and the intrinsic concentration n_i. The annihilation of free charge carriers creates a region that is virtually free of mobile charge carriers, the so called Space Charge Region (SCR).

A sketch depicting the formation of a SCR is shown in Fig. 3.5 By applying a reverse bias the SCR gets wider and its width is given by [27]:

$$W(V) = \sqrt{\frac{2\epsilon_0 \epsilon_{Si}}{e}\left(\frac{1}{N_A} + \frac{1}{N_D}(V + V_{built-in})\right)} \tag{3.2}$$

Figure 3.5: Schematic visualization of the formation of a space charge region (SCR) in a p-n-junction. At the moment of contact electrons and holes flow due to a concentration gradient and annihilate. In Equilibrium a SCR is formed. Taken from [24].

with the permittivity of vacuum ϵ_0 and the permittivity of silicon ϵ_{Si}. When the bias voltage is sufficiently high enough the whole semiconductor is depleted of its free charge carriers and the SCR spreads across the whole volume.

A charged particle passing through the depleted volume creates e/h pairs, which now are not overshadowed by the intrinsic free charge carriers of the semiconductor and can be measured.

3.2 Interaction of Charged Particles with Matter

Particle detectors detect particles through interactions with the detector material. This can be realized through the observation of for example Cherenkov radiation or scintillation light. In silicon detectors, charged particles are detected by measuring the charges they produce along their trajectory through the detector. The mean energy loss rate of a charged particle traversing a medium is given by the Bethe equation [28]:

$$-\left\langle\frac{dE}{dx}\right\rangle = Kz^2\frac{Z}{A}\frac{1}{\beta}\left[\frac{1}{2}ln\frac{2m_ec^2\beta^2\gamma^2W_{max}}{I^2} - \beta^2 - \frac{\delta(\beta\gamma)}{2}\right]. \tag{3.3}$$

With the atomic number of the absorber Z, the atomic mass of the absorber A, the electron rest mass m_e, the speed of light in vacuum c, the ratio between the particle velocity and the speed of

light in vacuum $\beta = \frac{v}{c}$, the so called Lorentz factor $\gamma = \frac{1}{\sqrt{1-\beta^2}}$, the mean excitation energy I and the density effect correction to the ionization loss δ. The constant K is defined as:

$$K = 4\pi N_A r_e^2 m_e c^2. \tag{3.4}$$

with the Avogadro number N_A and the classical electron radius r_e, while W_{max} is the maximum energy transfer in a single collision given by:

$$W_{max} = \frac{2m_2 c^2 \beta^2 \gamma^2}{1 + 2\gamma m_e/M + ()m_e/M)^2}. \tag{3.5}$$

The energy loss defined in Eq. 3.3 is the so called mass stopping power in the units MeV g^{-1} cm^2. In Fig. 3.6 the full function of the mass stopping power is shown for a muon traversing copper as an example. An important point in this graph is the minimum at $\beta\gamma \approx 3$. Particles in this region are so called Minimum Ionizin Particles (MIP) and are often used as a benchmark for detector performances as they create the smallest signal charges in the detector [12]. Because of the normalization of the mean energy loss to the mass density, the course of the Bethe function is very similar for different materials, as can be seen in Fig. 3.7. One should also note the different momentum axes for different particle species.

The energy of a charged particle is not deposited continuously along its track, but rather in a statistical manner leading to fluctuations in the deposited energy. Fluctuations occur in the number of collisions between the charged particle and the detector medium as well as in the transferred energy in each collision with the first ones being describable by a Poisson distribution and the latter by a Landau distribution [24]. In silicon, the mean ionization energy lies at 3.6 eV, so a MIP with an average energy loss of 388 eV/μm creates on average about 108 e/h pairs per μm detector thickness. Due to the large tail of the Landau distributiuon, the Most Probable Value (MPV) of the number of e/h pairs created lies 30 % below the average at around 76 e/h pairs per μm [24].

3.2.1 Silicon based Particle Detector

In Fig. 3.8 the structure of a silicon particle detector and its working principle is shown. An ionizing particle traversing the fully depleted p-doped bulk of the detector creates e/h pairs along its trajectory. The free charge carriers then drift to their respective electrodes and induce a charge on the doped strip, which is then capacitively coupled to the readout strips which are connected to a preamplifier [24]. The p$^+$-stop implants used to isolate the strips from each other.
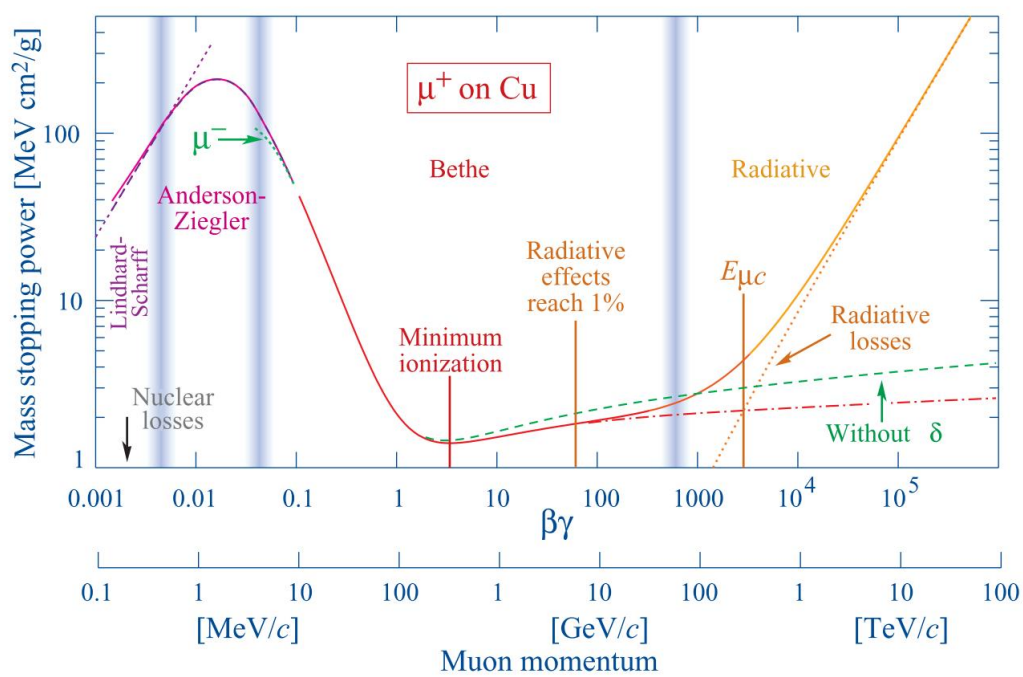
Figure 3.6: Mass stopping power of Cu as a function of $\beta\gamma$, taken from [28].
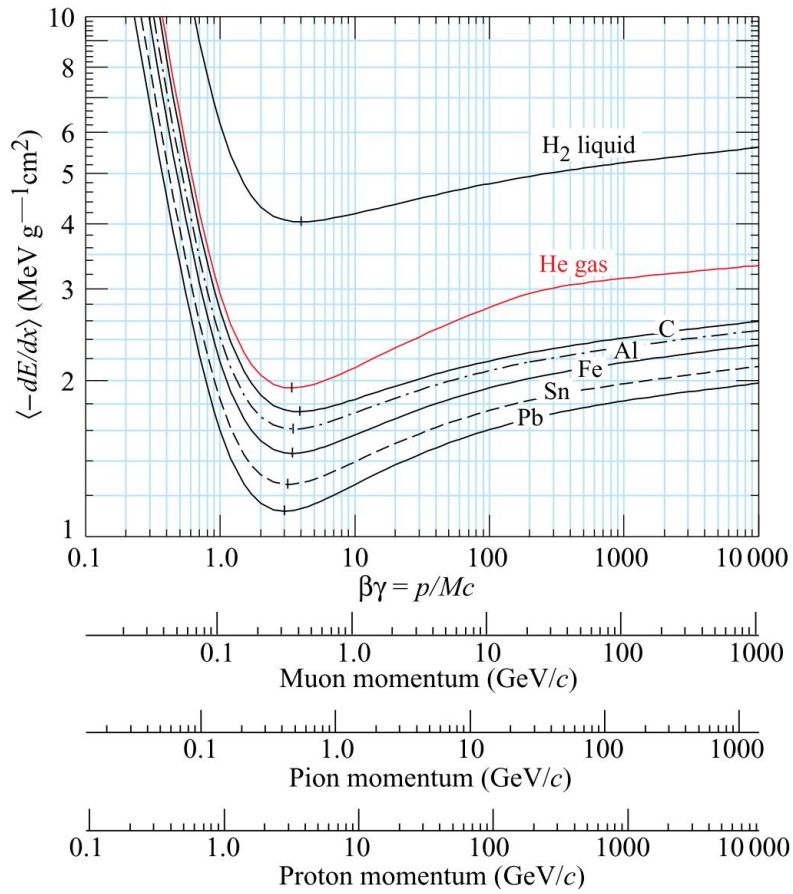
Figure 3.7: Mass stopping power of different media (H$_2$ liquid, He gas, C, Al, Fe, Sn, Pb) with different charged particle species (Muon, Pion, Proton) momenta. Notice the same position (in $\beta\gamma$) of the mass stopping power minimum for different materials. Taken from [28].
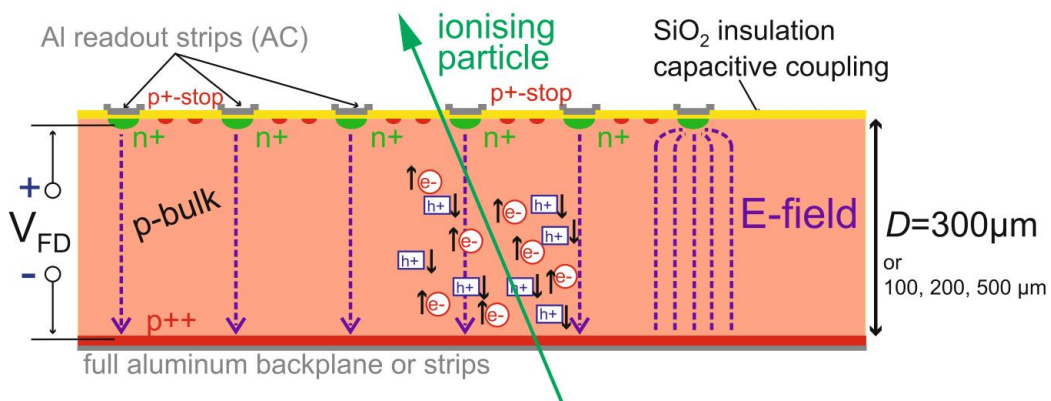
Figure 3.8: Schematic depiction of an n-in-p type silicon particle detector .Taken from [24].

4 Basics of Low Gain Avalanche Detectors

Low Gain Avalanche Detectors (LGAD), in literature also called Ultra Fast Silicon Detectors (UFSD), are Si detectors optimized for timing applications and a timing precision of 16 ps has been demonstrated for a set-up based on LGADs [29]. By introducing additional doping close to the p-n-junction, a spike in the electric field is created, enabling electron multiplication and thus signal amplification inside the sensor itself. The sensors are operated at reverse bias such that the gain is in the order of ~10-20 to minimize noise contributions that worsen the timing precision. Gain enables the use of thin sensors which without gain would produce too low signals. Compared to thick sensors, thin detectors have a higher slew rate of the signal, which is beneficial for timing precision. As Si detectors are used in various high energy physics applications, their radiation hardness has been thoroughly studied. However, the influence of radiation on the gain layer is still under investigation. LGADs have been shown to maintain a timing precision of $\sigma_t \sim 30\ ps$ after neutron radiation up to $n_n \approx 1.5 \cdot 10^{15}$ cm^{-2} and $\sigma_t \sim$50 ps for $n_n \approx$t10^{16} cm^{-2} [30].

4.1 Working Mechanism

In LGADs charge multiplication is used to amplify signals on the detector level. Charge multiplication takes place when free charge carriers acquire enough energy to ionize the detector material and create secondary e/h pairs. In silicon this becomes possible when the electric field reaches values in the order of $E \sim$300 kV/cm and the charge multiplication is governed by electrons [31]. Externally applied biases cannot create electric fields high enough without electric breakdown of the device. For this purpose a strongly ($N_D \approx 10^{16}$cm^{-3}) positively doped thin ($\sim 5\ \mu$m) layer (p^+-layer/gain-layer)is added closely beneath the n-doped layer (n^{++}-layer) of an n-p-junction [31]. In a depleted sensor these two layers create the necessary high field to enable charge multiplication in the localized gain region. The multiplication process can be described by [32]:

$$N(l) = N_0 G = N_0 e^{\alpha(E)l} \tag{4.1}$$

with the number of free charge carriers before the multiplication process N_0, the path length inside the gain region l, a strong function of the electric field α and the gain G. To minimize the Charge Collection Time (CCT), the field in the bulk of the detector should be high enough that the drift velocity of electrons and holes is saturated which happens at electric fields of $E \sim$ 20-30 kV/cm [31, 33]. The electric field w.r.t. the position inside the detector is shown in Fig. 4.1. To avoid

lateral electric breakdown between the readout electrodes, additional structures such as the Junction Termination Extensions (JTE) and p-stop implants have to be implemented. They are shown in the schematic view of an LGAD in Fig. 4.2.

To keep an excellent timing performance, a high uniformity of the signals and therefore also of the gain is necessary [34].
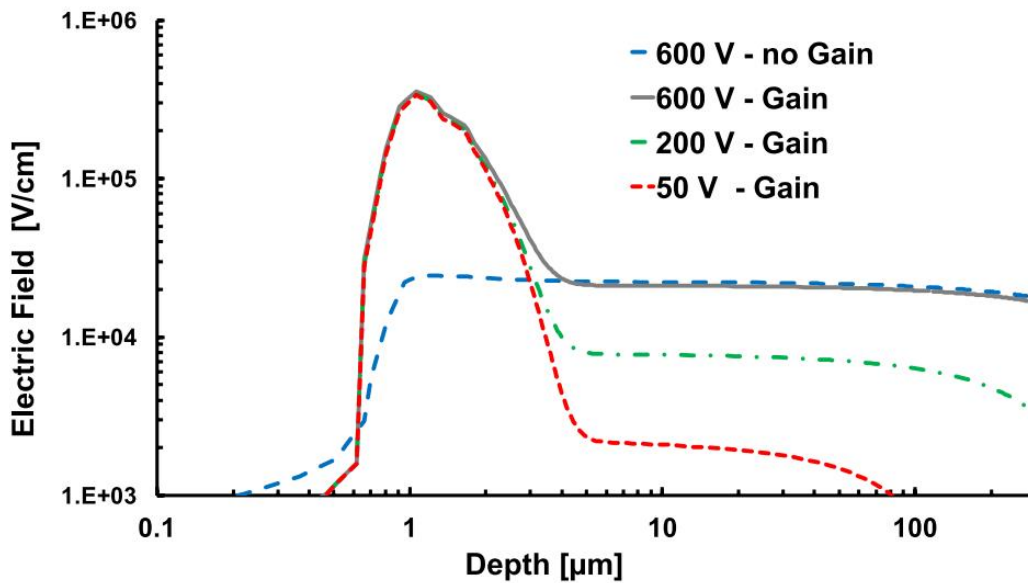
Figure 4.1: Electric field as a function of position inside a 300 μm thick LGAD at different biases and a PiN silion sensor. Taken from [33].
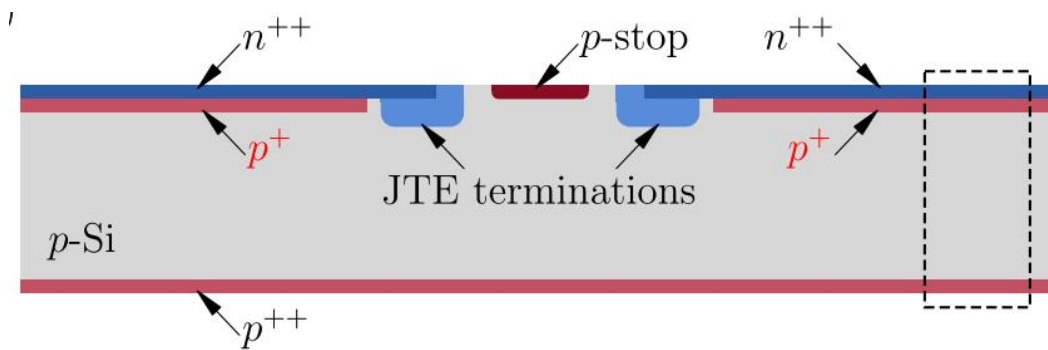
Figure 4.2: Schematic layout of an LGAD including JTE terminations and p-stop implants necessary to avoid lateral breakdown between the electrodes. Taken from [35].

An ionizing particle traversing the detector creates e/h pairs along its trajectory which then start to drift to the respective electrodes. When the electrons reach the gain region charge multiplication takes place and additional e/h-pairs are created. The secondary electrons, created close to the cathode, get absorbed after a short path while the secondary holes drift through almost the full detector thickness to the anode and create a large contribution to the signal [32]. A simulation done
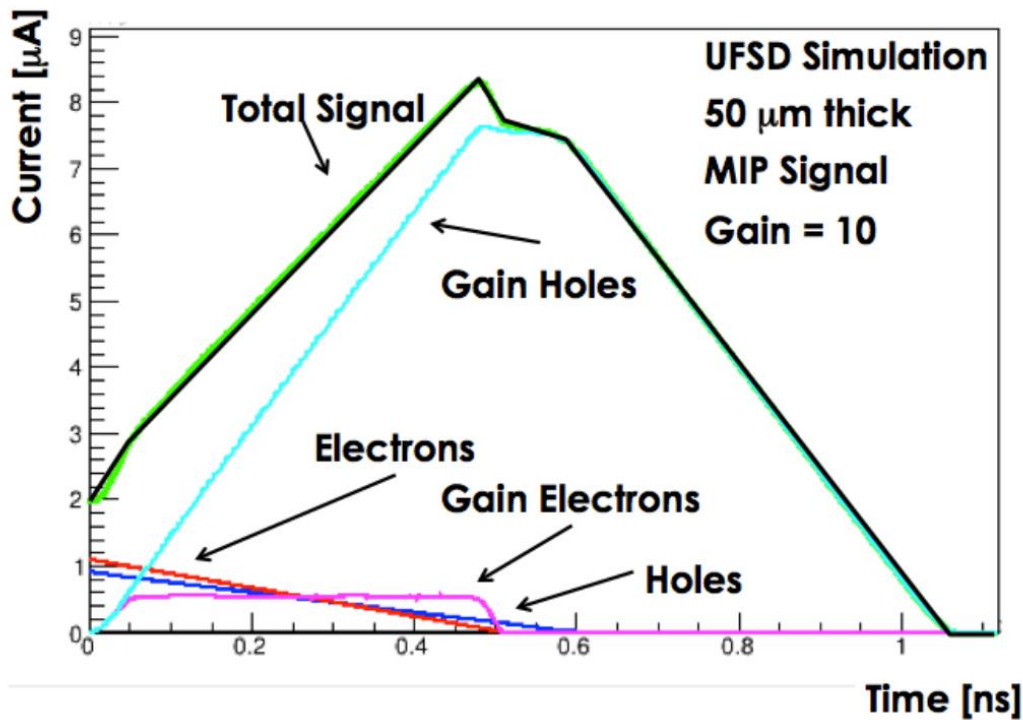
Figure 4.3: Simulated total current signal and its contributions for a 50 μm thick LGAD with a gain of 10 and a MIP traversing the detector. Taken form [32].

with Weightfield 2 (WF2) [36] of the total induced signal and its contributions is shown in Fig. 4.3.

During detector operation the resulting gain G can be varied by changing the applied bias. In Fig. 4.4 the gain dependence on bias voltage V for different doping concentrations of the gain-layer is shown. In addition it is important to note that JTE terminations and p-stop implants interrupt the gain-layer and create so called no-gain regions. Particles traversing the detector in a no gain region create signals that are a factor $\sim G$ smaller than signals induced by particles traversing a gain region. This results in a worse timing precision and inefficiencies in particle detection if the threshold is set too high. The ratio between the area with full gain and the whole detector area is the so called fill factor. Increasing the fill factor to values close to one is of interest to reduce the downsides of wide no-gain regions. A gain profile normalized to full gain which was calculated using numerical simulations plotted w.r.t. hit position of a particle in a detector can be seen in Fig. 4.5.

4.1.1 AC-coupled LGAD

As mentioned above, LGADs have a no gain region caused by JTEs and p-stop implants. To increase the fill factor of the sensor, so called AC-coupled LGADs (in literature also called Resistive Silicon Detector) got designed and produced [35, 38]. The main differences to a standard, or DC-coupled,

FBK UFSD2 - Gain
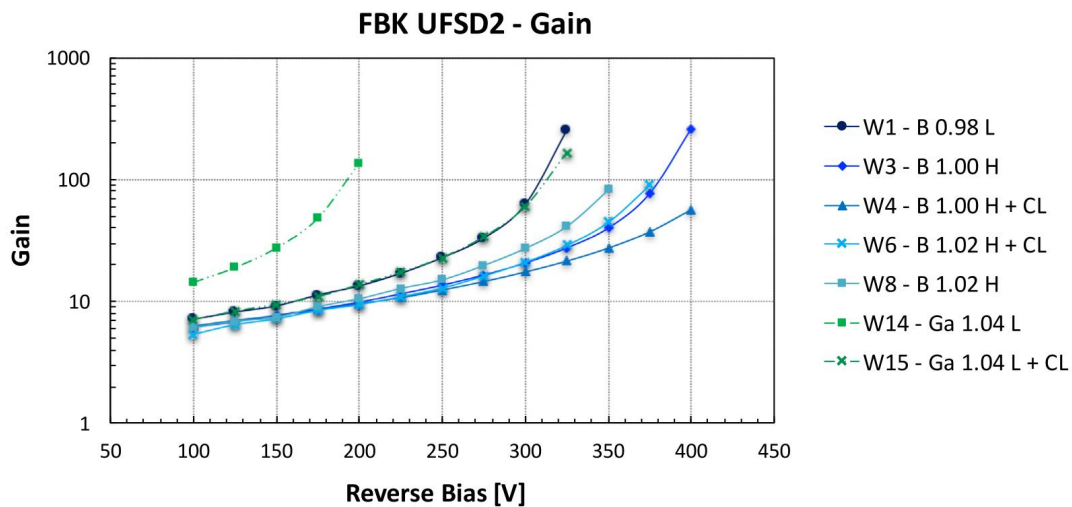
Figure 4.4: Measured gain versus bias voltage for different gain layer dopings of the UFSD2 production. The different wafers are labeled from W1 to W15, the dopant atoms used are either B or Ga. The implant doses are normalized and indicated with the number coming after the dopant species. Additionally, the width of the gain layer is indicated with L, standing for Low diffusion, meaning a more narrow gain layer, and H, standing for High diffusion and therefore for a wider gain layer. The additional +CL stands for a low carbon dose in the gain layer. Sensors without the label +CL do not have additional carbon in the gain layer. Taken from [37].

LGAD are a non segmented gain layer, an additional coupling layer above the n-doped layer, as well as a DC contact, to collect the charge, see Fig. 4.6. The readout pads are capacitively coupled to the detector via the coupling layer.

As the gain layer is not segmented, there are no regions without gain in the detector, except on the edges of the detector. This results in a fill factor of almost one.

After charge multiplication, the created charges drift to their electrodes and induce a signal. When the electrons reach the resistive layer, they flow towards the DC contact and induce an undershoot signal while in doing so. This creates an undershoot signal. Through proper design of the resistance of the resistive layer and the capacitance of the coupling capacitors, the amplitude and duration of the undershoot can be controlled.

In the following, when the coupling technology of an LGAD is not specifically mentioned, DC-coupled LGADs are meant, while AC-coupled LGAD are always labeled as such.
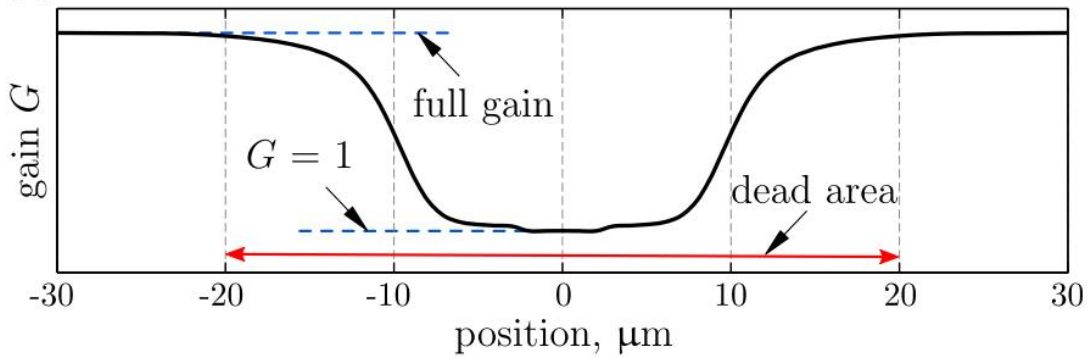
Figure 4.5: Gain profile of an LGAD including the no gain area caused by JTE terminations and p-stop implants. Taken from [35].
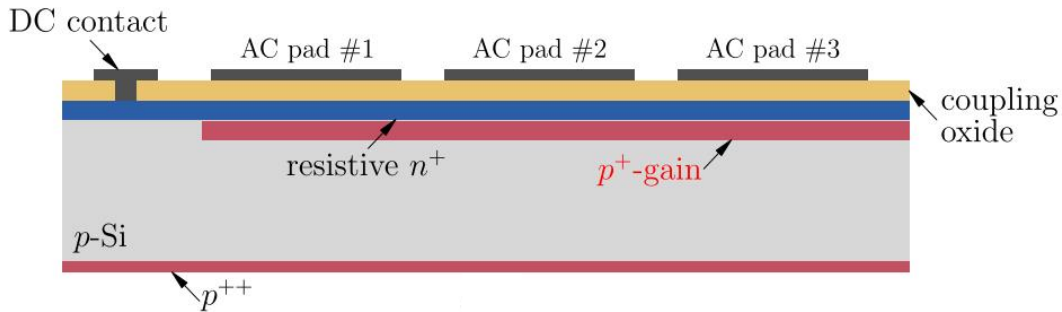
Figure 4.6: Schematic cross section of an AC-coupled LGAD. Taken from [38].

4.2 Timing Precision

To achieve accurate timing the Front End Electronic (FEE) has to be able to precisely determine the time when a particle passes the detector. A simplified model of a timing detector set-up is shown in Fig. **??**, where the sensor, in the figure labeled as Pixel, is read out by a Pre-Amplifier used for shaping of the signal. The shaped signal then gets compared to a set threshold to determine the time of threshold crossing and the output is then digitized using a Time to Digital Converter (TDC) [39].

By grouping the contributions to the timing precision σ_t^2 into five groups the precision can be expressed as [33]:

$$\sigma_t^2 = \sigma_{TimeWalk}^2 + \sigma_{LandauNoise}^2 + \sigma_{Distortion}^2 + \sigma_{Jitter}^2 + \sigma_{TDC}^2 \qquad (4.2)$$

The first two terms, $\sigma_{TimeWalk}^2$ and $\sigma_{LandauNoise}^2$, represent contributions from variations in the deposited signals mentioned in Sec. 3.2 with amplitude variations being the root of the so called Time Walk effect (TWalk) and irregularities in the energy deposition, therefore also in the signal shapes, being the cause for so called Landau noise. Signals can also be distorted due to varying drifting velocities of the charge carriers and the weighting field. This contribution is represented by the term $\sigma_{Distortion}^2$. The last two terms, σ_{Jitter}^2 and σ_{TDC}^2, are the uncertainties which arise from the
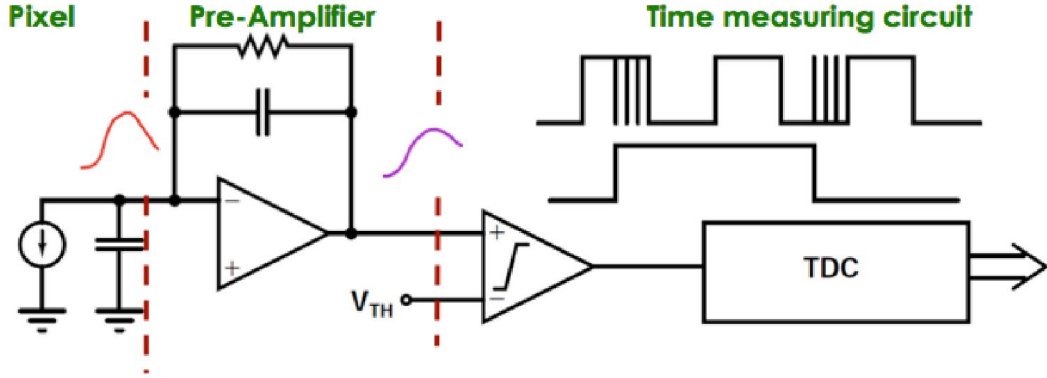
Figure 4.7: Main components of a time tagging detector, consisting of the sensors which is modeled as a capacitance with a parallel current source (Pixel), a Pre-Amplifier for shaping of the signal, a comparator for signal discrimination and time measurement and a Time to Digital Converter (TDC) Taken from [39].

electronics noise, known as jitter, which causes early or late registration of the time and digitization of the arrival time. In the following the different contributions and the implications for LGADs will be discussed.

4.2.1 Time Walk Effect

As mentioned above time registration happens when a signal crosses a fixed threshold V_{thr}. Signals with the same rise time (t_r) but with different amplitudes S cross this threshold after different delay times, t_d, as is illustrated in Fig. 4.8. This is known as the Time Walk effect, where the spread in t_d is the contribution to the timing uncertainty and can be written as [39]:

$$\sigma_{TimeWalk} = [t_d]_{RMS} \tag{4.3}$$

There are various ways to correct for the Time Walk effect and reduce its contribution to the timing uncertainty. For example, by using a constant fraction discriminator, which defines the time of arrival (TOA) of the signal to the point when the signal crosses a set fraction of the signal amplitude, the spread in t_d can be reduced.

Another way are signal amplitude dependent TOA corrections. By measuring the signal amplitude, or another observable which is correlated with it, one can correct the measured TOA. In this work, the correction is done in this way. The observable used is the Time over Threshold (ToT), which is the difference between the time when the signal crosses the threshold for the first time (leading edge time) and and for the second time (trailing edge time). In an offline analysis, ToT dependent correction parameters are found to correct for the time Walk Effect. For details see Sec. **??**.
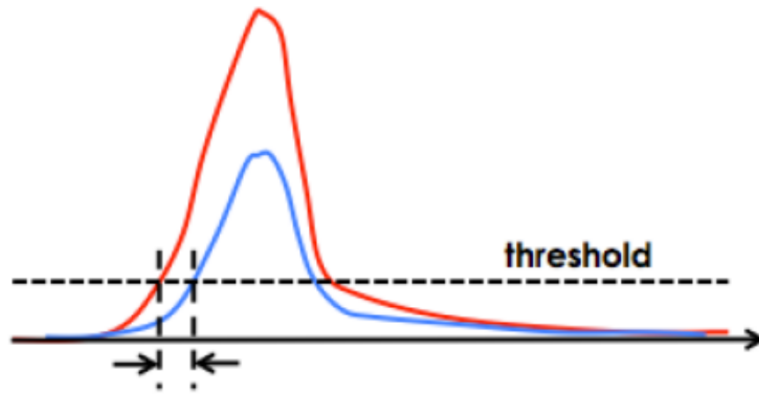
Figure 4.8: Schematic explanation of the Time Walk effect. Signals with similar shapes but different amplitude cross the threshold of a comparator at different times. Taken from [39].

4.2.2 Distortion Noise due to Weightfield and Drift Velocity

According to the Shockley-Ramo theorem [40], the induced current by a moving charge is given by:

$$i(t) = -q\vec{v} \cdot \vec{E_W} \tag{4.4}$$

where q is the charge of the charge carrier, $\vec{v}$ its drift velocity and $\vec{E_W}$ is the so called weighting field. From Eq. 4.4 one can deduce two important parameters to ensure high signal uniformity: (i) the drift velocity and (ii) the weighting field. A saturated drift velocity of the charge carriers is necessary to ensure uniform signals. However, to minimize noise contributions, such as Jitter, thin sensors are optimal because they have a lower breakdown voltage meaning that the applicable bias is lower. As a consequence it is possible that the drift velocity of the charge carriers does not saturate, leading to variations in the the signals. The weighting field is the electric field which would exist if the read out electrode was at unit potential, all other electrodes were grounded and all charges were removed [40].

Signals from particles traversing the detector at different lateral positions would generate different signals if the weighting field varied strongly in the lateral direction. To avoid this, the weighting field should be as uniform as possible. In Fig. 4.9 the weighting field for two different sensor geometries is shown. It turns out that to obtain a lateral uniform weighting field the width of the electrodes should be similar to the pitch while being bigger than the sensor thickness [41].

4.2.3 Jitter

Small fluctuations on the signal itself, as shown in Fig. 4.10, can cause an early or late firing of the comparator. The fluctuations are called Jitter and the timing uncertainties that arise from Jitter can
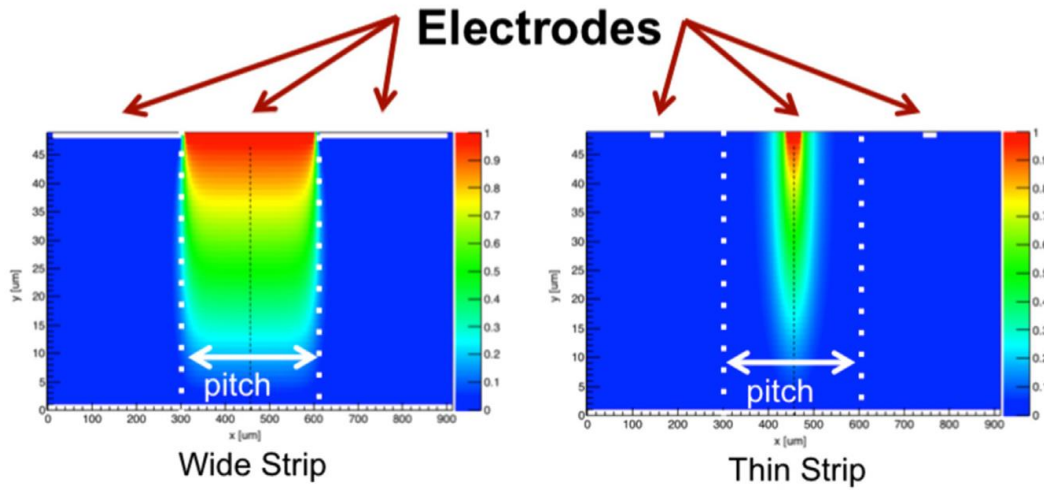
Figure 4.9: Weighting field for two different geometries. The weighting field of a wide electrode strip (left) display a bigger lateral homogeneity than the one of a narrow electrode (right). Taken from [41].
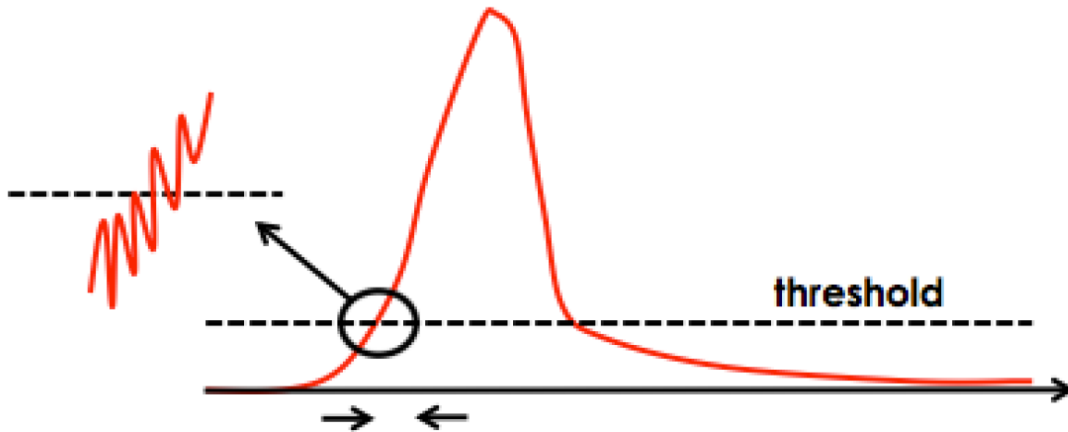
Figure 4.10: Schematic depiction of Jitter noise an the signal causing an early or late crossing of a set threshold.Taken from [39].

be expressed as [33]:

$$\sigma_{Jitter} = \frac{N}{dV/dt} \tag{4.5}$$

with the RMS noise level N and the signal slope dV/dt.

Using Eq. 4.4 and the fact that a MIP produces around 70 e/h pairs per μm the maximum induced current in a LGAD can be calculated [31]:

$$I_{max} \propto Nq\frac{1}{d}v_{sat} = 70dq\frac{1}{d}v_{sat} = 70qv_{sat}. \tag{4.6}$$

Here, a saturated drift velocity is assumed. One can see that the maximum induced current I_{max} is independent on the sensor thickness. Interestingly, the rise time of a current signal generated by a MIP is as long as the drift time of an electron traversing the whole sensor, making the rise time dependent on the sensor thickness [33]. Therefore, the slew rate of the signal dV/dt is higher in thin than in thick sensors, reducing the contributions of Jitter to the timing uncertainty. The dependence of the signal rise time on the sensor thickness is indicated in Fig 4.11 (a) and (b). In detectors with gain the maximum induced current naturally depends on the gain G. By using the Shockley-Ramo theorem again, the influence of the gain on the slew rate of the signal can be expressed as [31]:

$$\frac{di_{Gain}}{dt} \sim \frac{dV}{dt} \propto \frac{G}{d} \tag{4.7}$$

with the current induced by charges created in the avalanche process di_{Gain}. The dependence of the slew rate on sensor thickness and gain, obtained with WF2, is shown in Fig 4.11 (b). In summary, one can say that the maximum induced current is only proportional to the set gain value and the slew rate is depending on sensor thickness [33]. Therefore, very thin sensors with high gain would have the smallest contribution from Jitter onto the timing uncertainty. Nevertheless, too thin sensors or too high gain would have a negative impact on timing precision as other contributions to the timing uncertainty would rise.

4.2.4 Landau Noise

Landau noise is associated with the variations in non uniform energy deposition inside the sensor. This does not only lead to amplitude fluctuations, which are the cause of the Time Walk effect, but

(a)

(b)
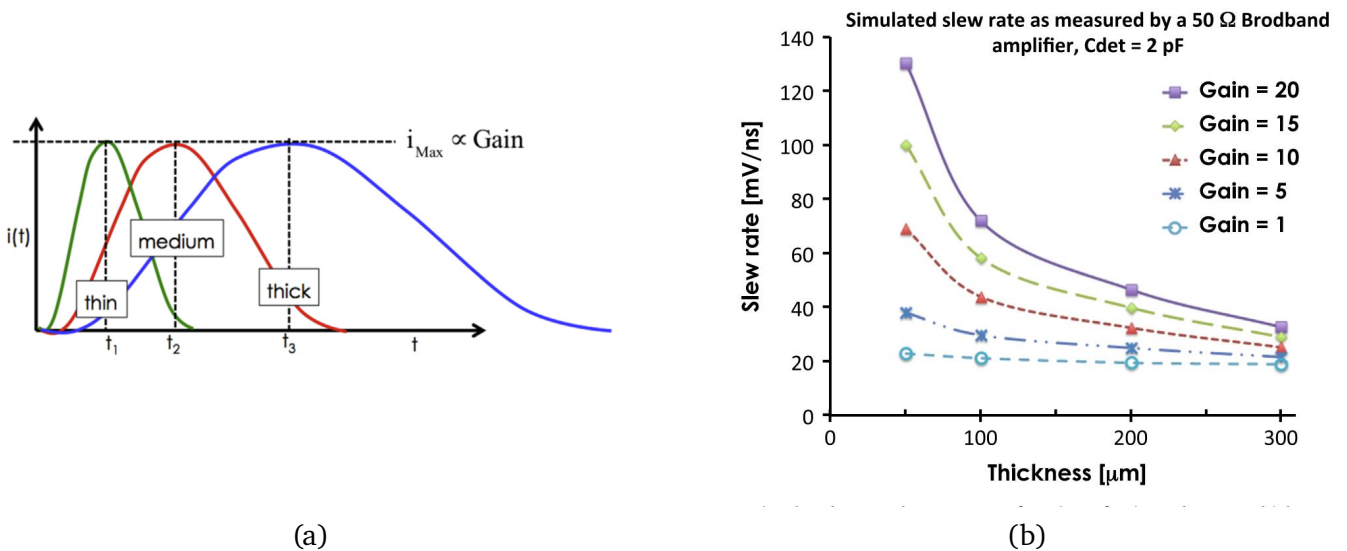
Figure 4.11: Signal width for LGAD with three different thicknesses (a). Simulated slew rate of LGAD depending on active sensor thickness and gain. Simulations were done using WF2 (b). Both taken from [31].

also to irregularities in the induced currents and therefore to signal shape variations. In Fig. 4.12 one can see the simulated (WF2) energy deposition of a MIP (left side) and the induced current signals (right side) for two different events (a) and (b). As one can see, the differences in the current signal can be substantial. One way to reduce the influence of Landau noise on the timing precision is to use thin sensors as their steep signal is less sensitive to fluctuations in the signal shape. However, in thin sensors the MPV of the energy loss of ionizing particle passing through tends to decrease for smaller sensors while the width of the energy loss distribution increases [42]. This leads to an enhanced Time Walk effect [39]. In Fig. 4.13 the Landau contributions to the timing resolution, simulated with WF2, versus the comparator threshold is shown for 300 and 50 μm thick sensors with different gains. As one can see, the gain does not have a large impact on the resolution. However, thin sensors have a significantly smaller timing uncertainty due to Landau fluctuations. In both cases, a low comparator threshold is most optimal.

4.2.5 Shot Noise

Shot noise is due to the discrete nature of charge carriers generating the leakage current in a p-n-junction [25]. As the shot noise increases with leakage current the, built in gain in LGADs leads to an enhancement of shot noise in two ways. As it is indicated in Fig. 4.14 (a), the leakage current can be divided into the surface current $I_{Surface}$, which does not get amplified, and the bulk leakage current I_{Bulk}, which gets amplified as the charge carriers generating it undergo charge multiplication.
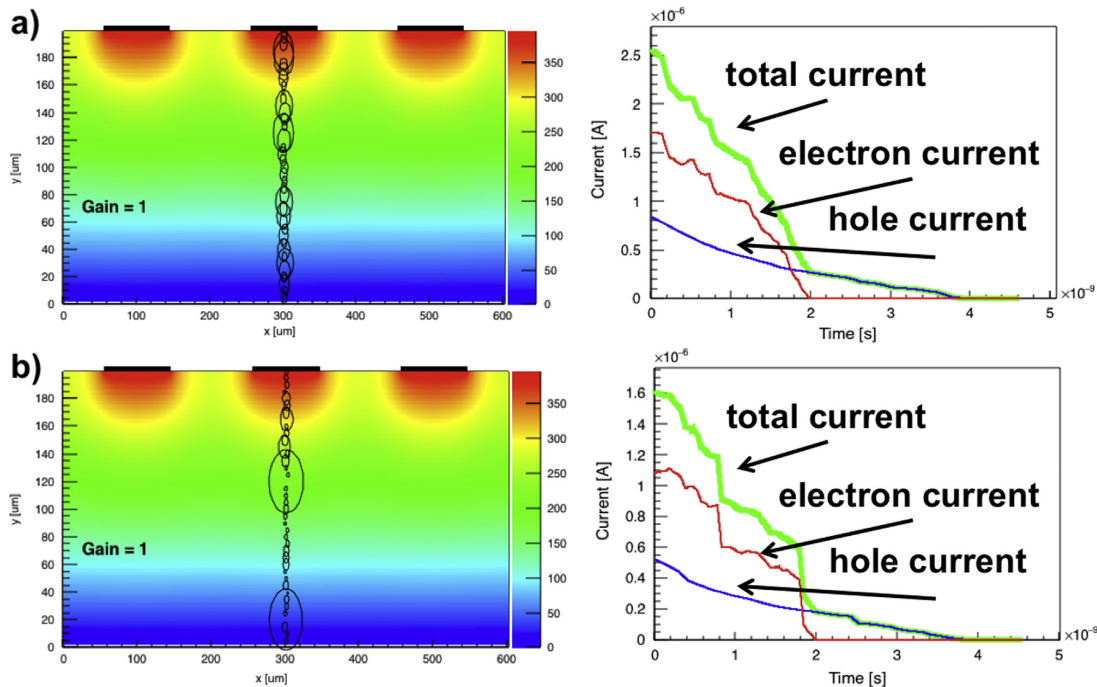
Figure 4.12: Simulated deposited energy by a MIP in an LGAD (left) and the corresponding simulated current signal (right) for two different events (a) and (b). Simulations were done using WF2. Taken from [41].
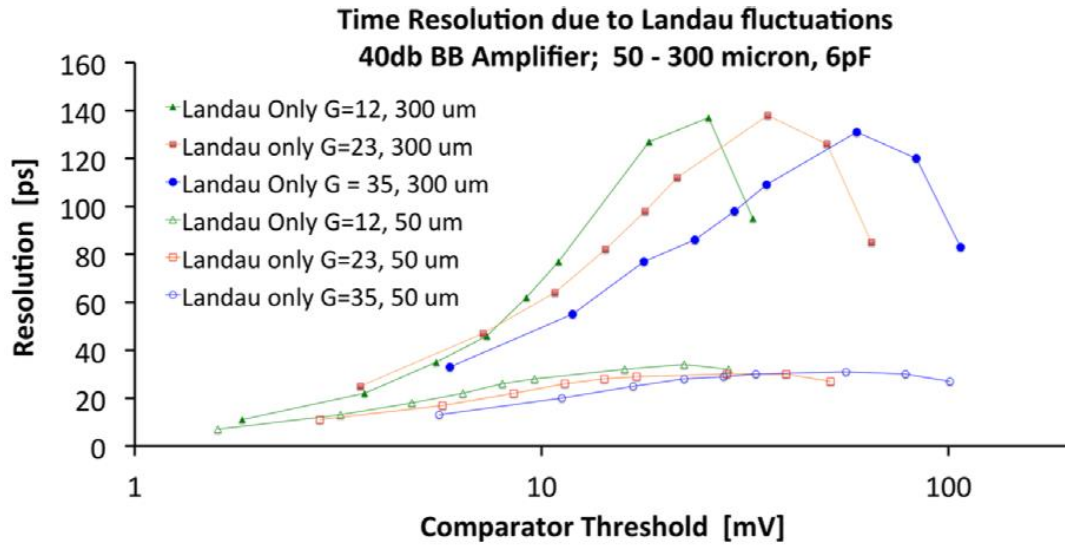
Figure 4.13: Simulated contributions to the timing uncertainty of Landau fluctuations for different 300 μm and 50 μm thick LGADs with different gains. Simulations were done using WF2. Taken from [41].

Being a statistical process, charge multiplication is another source of noise as not every charge gets multiplied by the same value, giving rise to the so called Excess Noise Factor (ENF). The ENF can be expressed as [33, 43, 44]:

$$F \sim G^x = kG + \left(2 - \frac{1}{G}\right)(1 - k) \tag{4.8}$$

with the ratio $k = \alpha/\beta$ between the hole ionization rate α and the electron ionization rate β, and with the average gain in the device G. With this the shot noise current density is can be expressed as [33]:

$$i_{shot}^2 = 2qI_{Det} = 2q[I_{Surface} + (I_{Buld} + I_{Signal})G^2G^x] \tag{4.9}$$

with the gain G, the excess noise factor expressed in terms of gain G^x and the signal current I_{Signal}. Excess noise leads to the effect that noise in a sensor with gain gets stronger amplified than the signal, thus the signal to noise ratio S/N worsens with gain. Usually this is no problem for Si detectors as the total noise is normally dominated by electronic noise and not by sensor noise [33]. However, by choosing a too high gain value sensor noise can start to be significant and even be a dominating source of noise, as is indicated in Fig. 4.14 (b). Shot noise can be minimized by cooling as the leakage current decreases by a factor of 2 for every 7 K that the sensor is cooled [41].
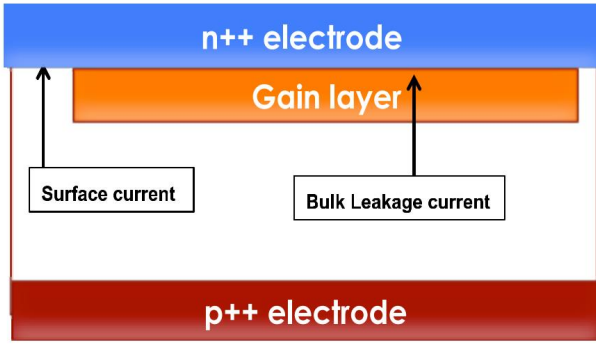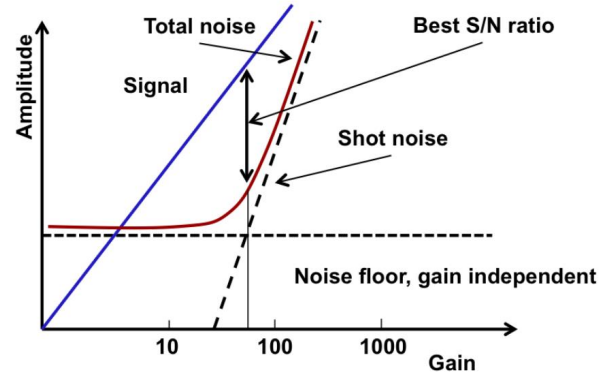
| (a) | (b) |

Figure 4.14: Schematic display of the contributions to leakage current in an LGAD. While the surface current does not get amplified, the bulk leakage current takes the same route as a signal and gets amplified due to the gain layer (a). Taken from [32]. Noise level of an LGAD w.r.t gain showing that shot noise becomes a dominant noise source at high gain and that the optimal signal to noise ratio is obtained at low to medium gain (b). Taken from [32], based on [45].

4.3 Radiation Hardness

The radiation hardness of LGADs is of great importance as they will be often used in environments characterized by radiation. Non-Ionizing Energy Loss (NIEL) is the main source of radiation damage to the bulk of the detector and introduces defects within the band gap [33]. Deep and shallow charged defects change the doping concentration (N_{eff}) by introducing additional donors/acceptors, shallow neutral defects have a negative effect on the charge collection efficiency (CCE) by trapping electrons and holes and mid-gap neutral defects generate leakage current [33]. In Fig. 4.15 a graphical representation of these effects is shown.

In addition to the removal of acceptors in the p-doped gain layer, acceptors in the bulk are created, following the equation [47]:

$$N_A(\Phi, x) = g_{eff}\Phi + N_A(0, x)e^{-c(N_A(\Phi,x))\Phi} \tag{4.10}$$

with the acceptor concentration $N_A(\Phi, x)$, an effective generation of acceptors $g_{eff}\Phi$ ($g_{eff} \approx 0.02\,\mathrm{cm}^{-1}$), the fluence Φ and an acceptor removal rate $c(N_A(\Phi, x))$, extracted from fits. The microscopic mechanism underlying the initial acceptor removal is not yet fully understood. A two step process consisting of first, the production of interstitial Si atoms through radiation, and second, an inactivation of the acceptors, seems to be a plausible explanation [48]. In Fig. 4.16 a secondary ion mass spectrometer measurement of an irradiated and a non-irradiated LGAD is shown. One can see that the doping profile for a heavily irradiated and a non-irradiated sensor is the same. This indicates that the acceptor atoms were not removed but rather deactivated.
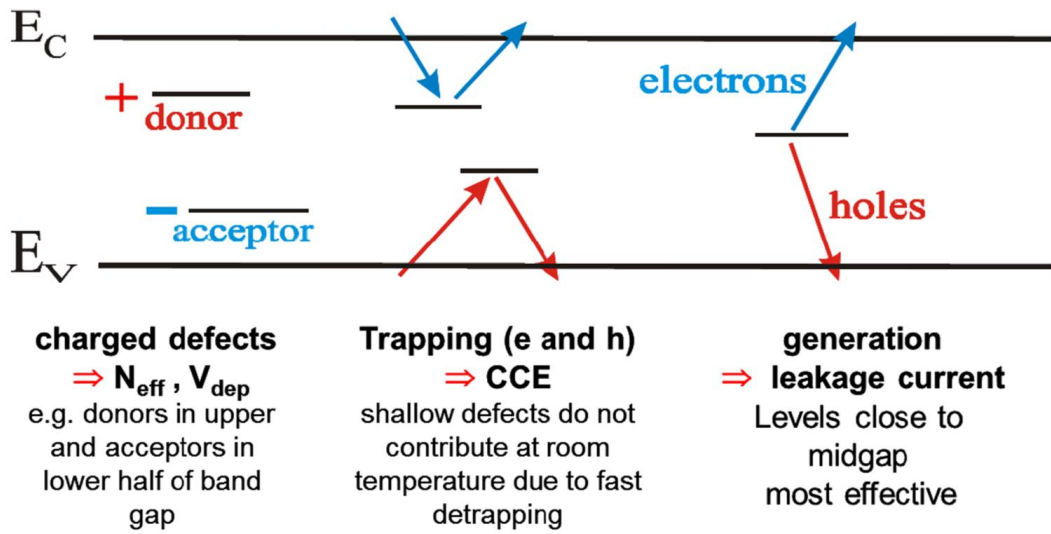
Figure 4.15: Schematic depiction of defects induced by radiation and the resulting effects. Taken from [33], based on [46].

The number of inactivated acceptors per incident particle increases with the initial acceptor density, as is shown in Fig. 4.17 (a). However, the fraction of removed acceptors to the current number of acceptors decreases with the acceptor density, see Fig. 4.17 (b). This indicates that gain layers with higher initial doping concentration are more radiation hard [48].

In Fig. 4.18 the evolution of different initial acceptor densities with increasing fluence can be seen. For details to the exact obtainment of the value for c, see [48]. In the plot one can see clearly the increased radiation hardness of high density doping as the drop in initial (active) acceptor density happens at higher fluences for higher initial doping densities. In addition, one can see that at sufficient high fluences the density of active acceptors converges to the density of a sensor with an initial acceptor density of $N_A = 6.2 \cdot 10^{12} \ cm^{-3}$, which corresponds to the bulk of a high resistivity PiN sensor [48]. Therefore, an LGAD does not differ from a standard PiN sensor if they were exposed to the same, sufficiently high fluence.

The leakage current vs bias voltage of 50 μm (50D) and 80 μm (80D) HPK sensors after being irradiated with different fluences (1 MeV neutron equivalent) is shown in Fig. 4.19 (a) [49]. As can be seen the leakage current increases with fluence and is lower for thin sensors at the same fluences. The leakage current can be expressed as [50]:

$$I = M_I I_{gen} = M_I(\Phi_{eq})\alpha\Phi_{eq}V \qquad (4.11)$$

with the generation current I_{gen}, the current multiplication factor M_I, the leakage current damage constant α (for details see [51]), the equivalent fluence Φ_{eq}, and the active volume V. As mentioned in Sec. 4.2.5 the increased leakage current can be reduced by cooling.

In Fig. 4.19 (b) the most probable collected charge of the same sensors for different fluences is shown. One can see that the collected charge decreases for increasing fluences which can be attributed to a
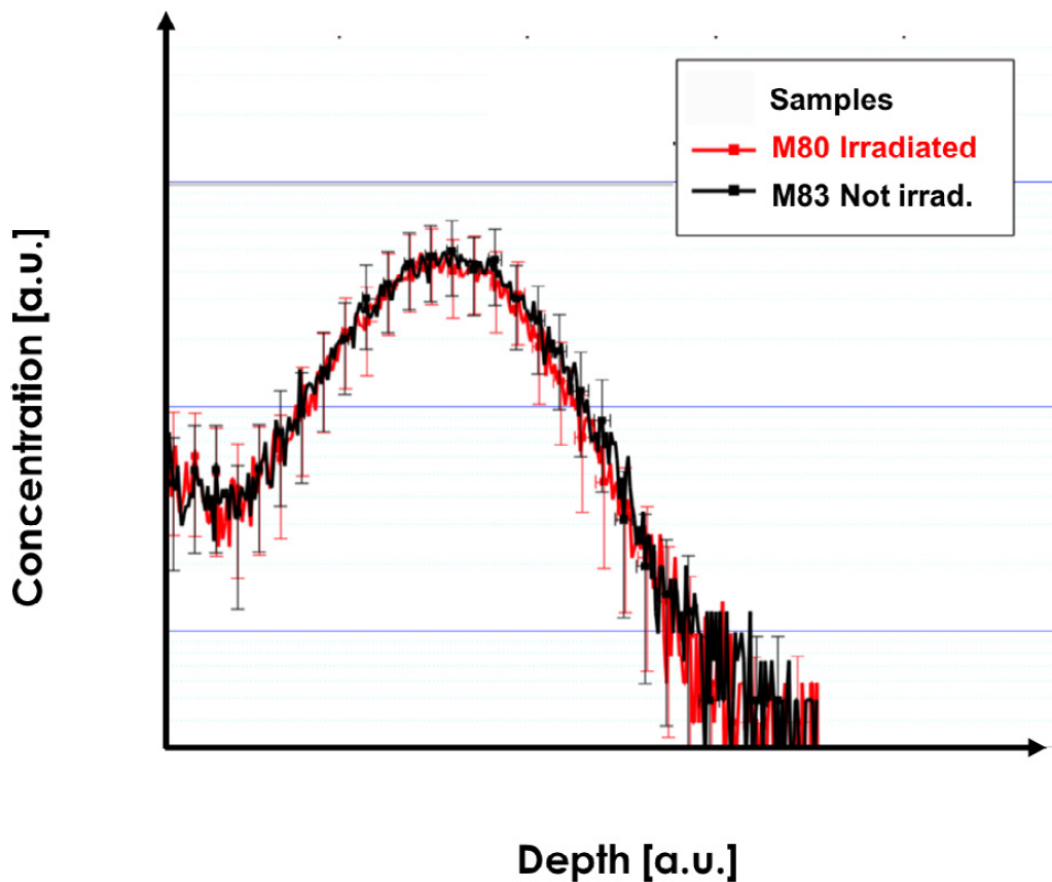
Figure 4.16: Density of Boron atoms in the gain layer of a non-irradiated (M83) and an irradiated LGAD (M80) with an almost completely deactivated gain layer. The density profiles are the same, indicating that the Boron atoms were not removed from the lattice but rather inactivated. The scales in x- and y-direction are logarithmic. Taken from [48].

combination of worse CCE through trapping and a lower gain caused by removal of acceptors in the gain layer which leads to a smaller peak electric field in the gain layer. Up to a certain level of fluence the reduced gain and CCE can be compensated by an increased bias voltage. Especially at high fluences the residual acceptors in the gain layer play a bigger role in thin sensors than in thick [49]. One can see for more heavily irradiated devices that the collected charge stays constant for a wide range of bias voltage and then starts to increase as mulitplication sets in. This happens earlier for thin sensors.

In the following three different approaches to improve the radiation hardness of LGADs will be discussed. The substitution of Boron dopant atoms with Gallium promised to improve the radiation hardness of LGADs. Due to higher mass of Gallium it is less likely to be removed from the crystal lattice and it was speculated that it would also be less susceptible to inactivation due to Si interstitials [52]. In [52] an inactivation rate around two times smaller than the one from Boron was reported for Gallium. It is possible that the lower inactivation rate of Gallium was due to a larger initial
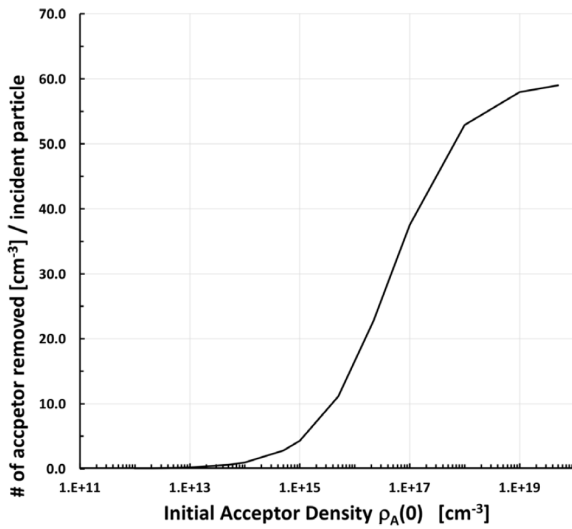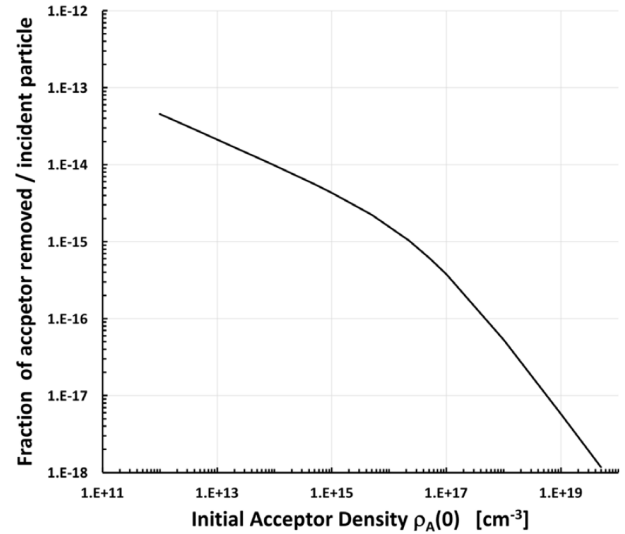
Figure 4.17: Number of acceptors removed by an incident particle versus the initial accep-
tor density (a). Fraction of acceptor removed by an incident particle versus the
initial acceptor density. Taken from [48].

doping. Additionally, in [48] a larger inactivation rate of Gallium was found which was not solely
explainable with a lower doping concentration. This would mean that doping the gain layer with
Gallium instead of Boron does not improve the radiation hardness of LGADs.

Other approaches to improve the radiation hardness of LGADs are a C-coimplantation in the volume
of the gain layer [30, 53] and so called deep gain layers [53] and will be discussed in the following.

Deep Gain Layer

In [53], the effects of deep gain layers, i.e. gain layers with a distance to the surface bigger than in
standard LGADs, on radiation hardness were investigated. Deep gain layers do not alter the acceptor
removal process but improve the ability to recover gain with the bias voltage as the volume in which
charge multiplication takes place is bigger. In Fig. 4.20 one can see measured gain vs bias of HPK
LGADs with deep gain layers where the gain layer of HPK-3.2 is deeper than the one of HPK-3.1 (see
Sec. 4.3.1). As one can see, HPK-3.2 outperforms HPK-3.1 in terms of reachable gain significantly up
until fluences of $\Phi_{eq} = 1.5 \cdot 10^{15} n_{eq} cm^{-2}$ and slightly at the fluence of $\Phi_{eq} = 3 \cdot 10^{15} n_{eq} cm^{-2}$. However,
due to the very deep gain layer, operation of the HPK-3.2 sensor at temperatures of -30° C had to
take place close to the break down voltage, worsening the timing performance before irradiation.
In Fig. 4.21 one can see the timing performance of the HPK sensors for different fluences. Timing
precisions of around 40 ps and 30 ps could be reached for fluences up to $n_{eq} = 4 \cdot 10^{14} cm^{-2}$ for
HPK-3.1 and HPK-3.2 respectively while after $\Phi_{eq} = 3 \cdot 10^{15} n_{eq} cm^{-2}$ the timing precision was around
60 ps.
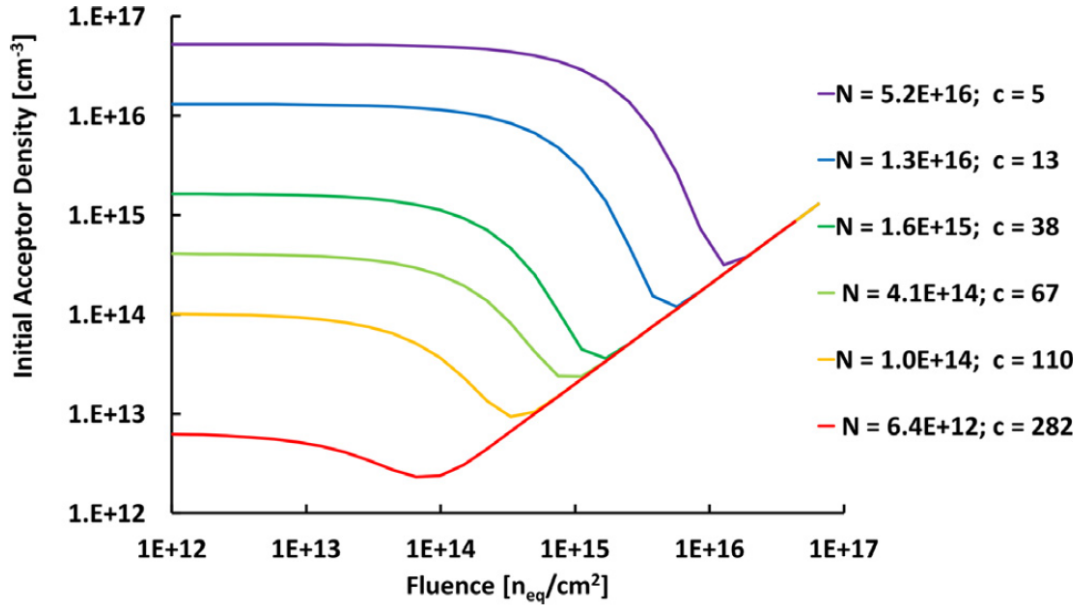
Figure 4.18: Density of initial acceptors in an LGAD as a function of fluence. Note that after a fluence in the order of $\Phi_{eq} \sim 10^{16} n_{eq} cm^{-2}$ the LGADs have the same acceptor density as a PiN diode without gain layer (b). Both taken from [48].

Carbon Co-Implantation in Gain Layer

A Carbon co-implantation in the gain layer has been shown to reduce the inactivation of acceptors and therefore the decrease in gain due to radiation damage [30, 48, 53]. In contrast to a deep gain layer, additional carbon in the gain layer does not alter the performance of LGADs at low fluences as it is electrically inactive. In Fig. 4.22 one can see the evolution of the still active gain layer fraction with rising fluence. The function fitted to the measured data is the exponential of Eqn. 4.10, normalized to be ≈ 1 for $\Phi = 0$. The fit is used to extract the acceptor removal rate c from Eqn. 4.10. As one can see in Fig. 4.22, the fraction of active gain layer for a given fluence is bigger for carbonated sensors (W6 B+C and W15 Ga+C) than for non-carbonated devices (W8 B, W14 Ga and W1 B LD). A bigger fraction of active gain layer for a given fluence means also that the acceptor inactivation rate c is lower, as can be seen in the given fit functions.

Comparing the non carbonated sensors, one can see that the more densely doped LGAD (W1 B LD) is less prone to acceptor inactivation than the other non carbonated devices. The differences of the evolution of the active gain layer fraction between Boron (W8 B) and Gallium (W14 Ga) doped sensors is partly attributed to different densities of the dopants. However, it is claimed that the differences are bigger than they would be taking only the different doping densities into account [48].

In Fig. 4.23 (a) the timing performance of a carbonated sensor produced by Fondazione Bruno Kessler (FBK), from a different production than the ones shown in Fig. 4.22, for different fluences is shown. One can see the trend that with higher radiation exposure a higher bias voltage needs to be applied to reach a similar timing precision. Up to a fluence of $\Phi_{eq} = 8 \cdot 10^{14} n_{eq} cm^{-2}$ a timing precision

(a)   (b)
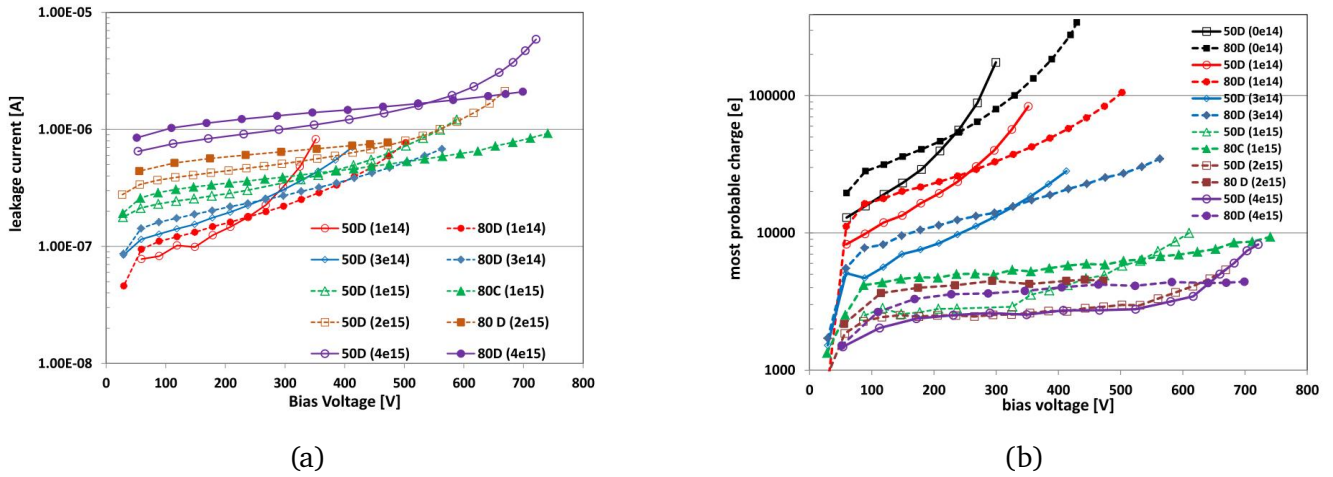
Figure 4.19: Leakage current versus applied bias for HPK sensors with 50 μm and 80 μm thickness after irradiation with different fluences (a). Most probable collected charge versus applied bias for HPK sensors with 50 μm and 80 μm thickness after irradiation with different fluences (b). Both taken from [49].

of about 40 ps can be reached and the timing precision stays below 60 ps up to $\Phi_{eq} = 3\cdot10^{15}\mathrm{n}_{eq}\mathrm{cm}^{-2}$ and is around 65 ps even after $\Phi_{eq} = 4\cdot10^{15}\mathrm{n}_{eq}\mathrm{cm}^{-2}$. For the non-carbonated sensor only the timing precision after irradiation with a fluence of $\Phi_{eq} = 2.5\cdot10^{15}\mathrm{n}_{eq}\mathrm{cm}^{-2}$ is shown and a timing precision slightly above 60 ps is reached. This indicates that the carbon co-implantation does not only improve the radiation hardness in terms of active gain layer fraction but also in terms of timing precision, the key element of LGADs.

4.3.1 Characterization of Sensors using C-V-Measurements

For characterization of LGADs, so called capacitance-voltage-scans can be done. By measuring the capacitance of the sensor for a given bias voltage, the depletion voltage of the gain layer V_{GL}, the depth of the gain layer and the similarity of doping profiles can be investigated. A C-V-curve for four different sensors, two from HPK and two from FBK, is shown in Fig. 4.24 (a) and the $1/C^2$-V-curve is shown in Fig. 4.24 (b). An indicator for the depth of the gain layer is the initial capacitance in the C-V-curve. A lower initial capacitance at low bias indicates a deeper gain layer, while the intercept between the flat plateau at low bias and the extension of the fast rising part in the $1/C^2$-V-curve indicates V_{GL}, which is proportional to the doping concentration and depth of the gain layer [53]. One can see in both plots that the behavior of the FBK sensors does not differ from each other even though carbon was added to the gain layer of the FBK+C sensor. This shows that the co-implantation of carbon does not alter the electric properties of the sensor before irradiation as it is electrically inactive, while a deeper gain layer increases V_{GL} [53].

In Fig. 4.25 $1/C^2$-V-curves from a sensor with a deep gain layer, namely HPK3.2, Fig. 4.25 (a) and from a sensor with a carbonated gain layer, namely FBK3+C, Fig. 4.25 (b) before and after irradiation are shown. Two effects of irradiation can be observed. The first effect is that V_{GL} decreases
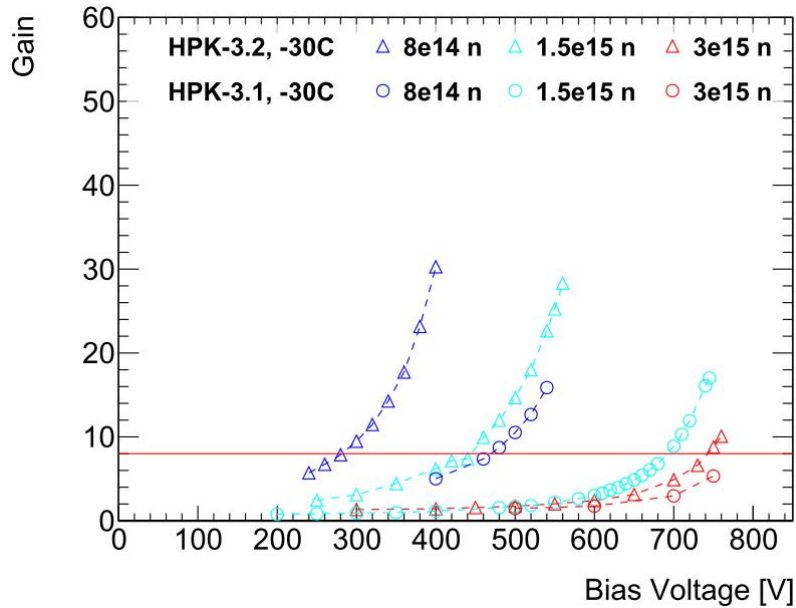
Figure 4.20: Gain versus applied bias voltage for two HPK LGADs with a deep gain layer after irradiation with different fluences. The gain layer of HPK-3.2 is deeper than the one of HPK-3.1. Taken from [53].

with irradiation. As V_{GL} is proportional to the doping concentration of the gain layer (the position of the gain layer does not change), this means that the active doping concentration in the gain layer decreases. In Fig. 4.25 (a) the observable decrease of V_{GL} is stronger than in Fig. 4.25 (b), indicating that the acceptor inactivation rate is smaller in carbonated gain layers. The second effect is the change of the slope at voltages above V_{GL}. This indicates a bulk with a higher resistivity and the increase of bulk doping [53, 54]. The proportionality between V_{GL} and the active doping concentration in the gain layer means, that V_{GL} measurements can be used to extract the acceptor inactivation rate c mentioned in Eqn. 4.10. The evolution of V_{GL} and the exponential fit according to Eqn. 4.10 to extract the c-value is shown in Fig. 4.26. One should note that the c-value as shown in Fig. 4.26 is not the gain layer inactivation rate, as the rate should be the same for both HPK devices as they have the same doping profile. The c-value can therefore be interpreted as a decrease rate of gain layer efficiency, meaning its influence on charge multiplication.

By plotting the bias voltage required to reach a certain gain (e.g. V(G=8)) versus V_{GL} for different fluences one finds a linear correlation. This enables, after calibration, the prediction of the needed bias voltage to reach a certain gain after a certain fluence using a V_{GL} measurement [53]. The linear correlation is shown in Fig. 4.27. In the plot the following two effects can be observed. First, the linear function for the FBK3+C LGAD is steeper than the one for the HPK devices with a deeper gain layer. This means that for a shallow gain layer after a certain decrease of V_{GL} a bigger increase in bias is needed to reach the same gain. Second, the measurement points, indicating the different fluences, are closer together in the FBK3+C sensor than in the HPK devices. This indicates a smaller inactivation rate of initial acceptors in the gain layer. As the carbon co-implantation and the deep
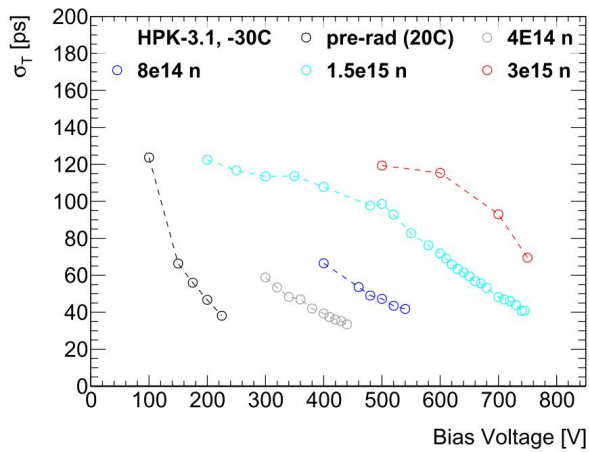
(a)
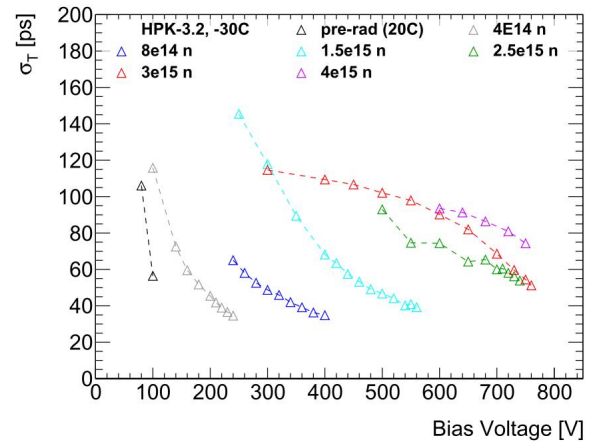
(b)

Figure 4.21: Timing precision of an HPK-3.1 LGAD versus bias after irradiation with different fluences (a). Timing precision of an HPK-3.2 LGAD versus bias after irradiation with different fluences (b). Both taken from [53].

gain layer are independent from each other and both increase the radiation hardness of an LGAD, it is expected that a combination of both technologies can further increase the radiation hardness [53].
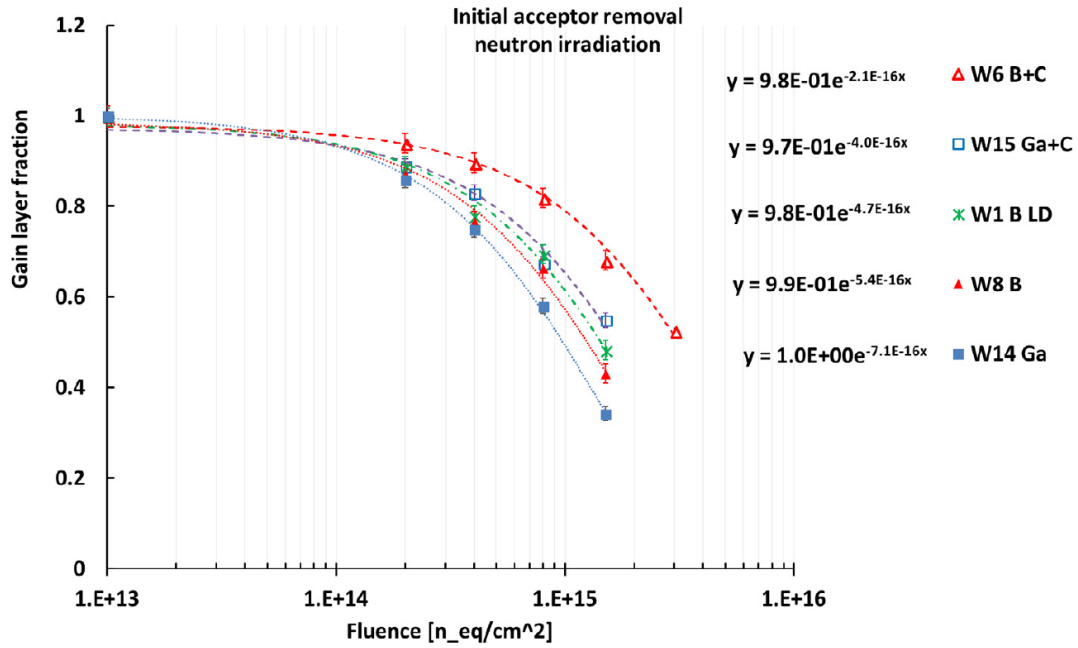
Figure 4.22: Fraction of active gain layer versus fluence for different FBK from the UFSD2 production. The different wafers are labeled from W1 to W15, the dopant atoms used are either B or Ga. The additional +C stands for a carbonated gain layer. The LD for W1 stands for low diffusion and indicates a more narrow, but more densely doped gain layer. Taken from [48].

    (a)   (b)
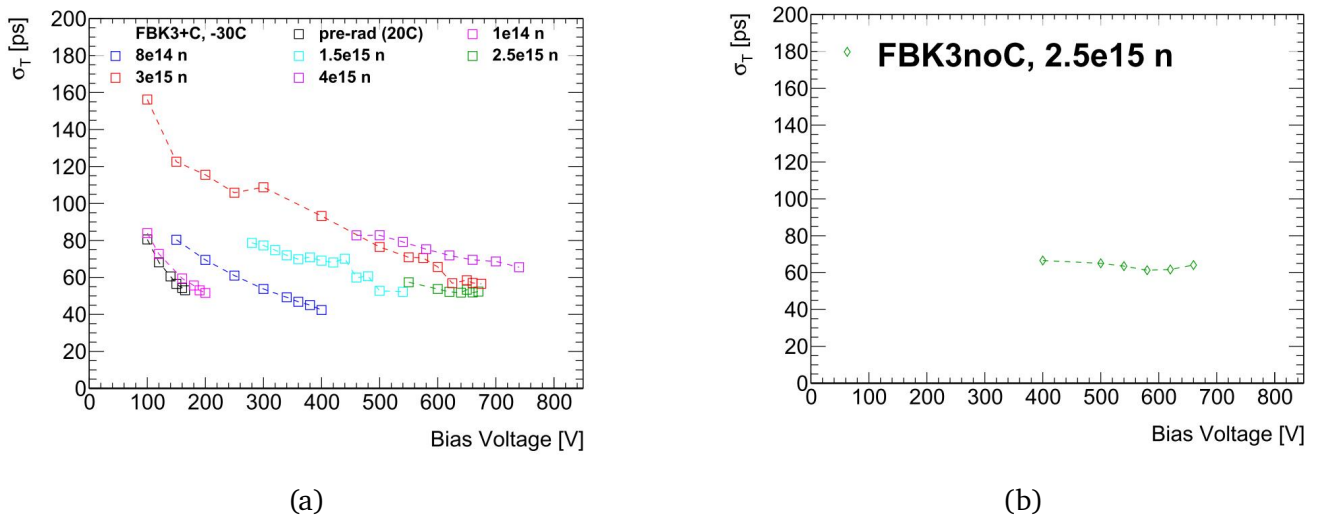
Figure 4.23: Timing precision of an FBK LGAD from the UFSD3 production with a carbon co-implantation in the gain layer versus applied bias after irradiation with different fluences (a). Timing precision of FBK LGAD from the UFSD3 production without a carbon co-implantation in the gain layer versus applied bias after irradiation with a fluence $\Phi_{eq} = 2.5 \cdot 10^{15} \mathrm{n}_{eq} \mathrm{cm}^{-2}$ (b). Both taken from [53].
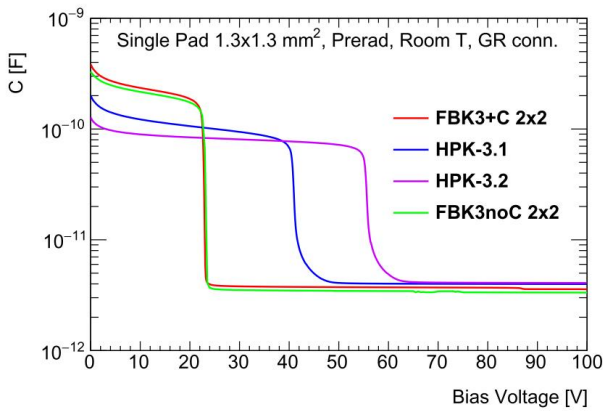
(a)
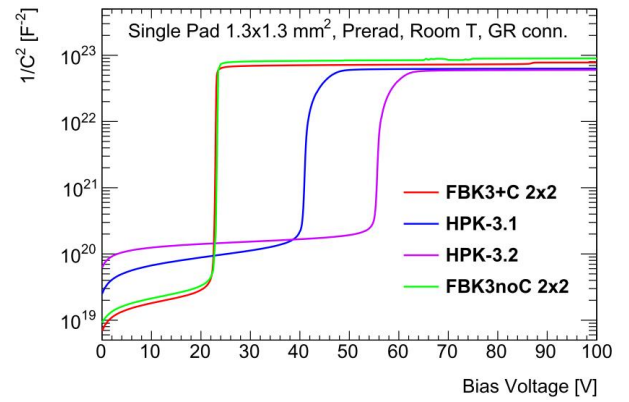
(b)

Figure 4.24: C-V-scan of 2 HPK LGADs with deep gain layers and 2 FBK LGADs, one with a carbonated gain layer (FBK3+C) (a). $1/C^2$-V-scan of 2 HPK LGADs with deep gain layers and 2 FBK LGADs, one with a carbonated gain layer (FBK3+C) (b). Both taken from [53].
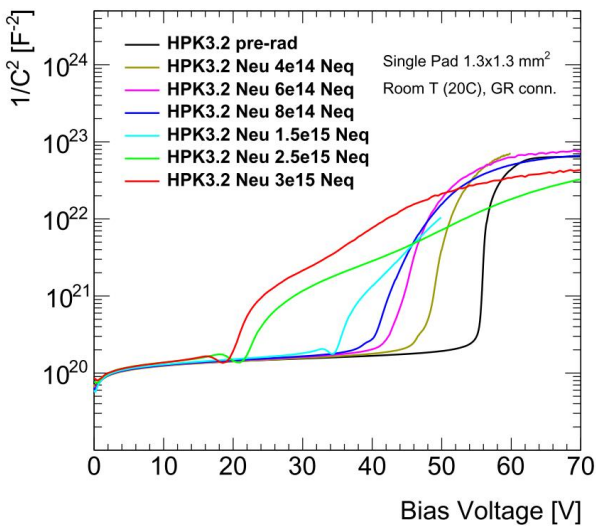
(a)
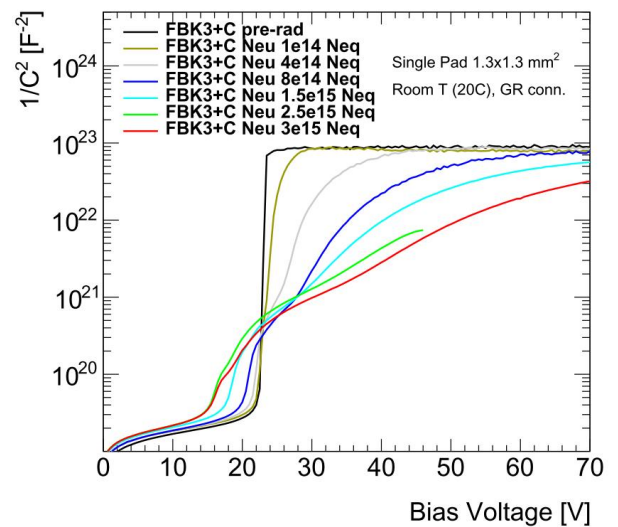
(b)

Figure 4.25: $1/C^2$-V-scan of an HPK LGAD with a deep gain layer after irradiation with different fluences (a). $1/C^2$-V-scan of an FBK LGAD with a carbonated gain layer after irradiation with different fluences (b). Taken from [53].
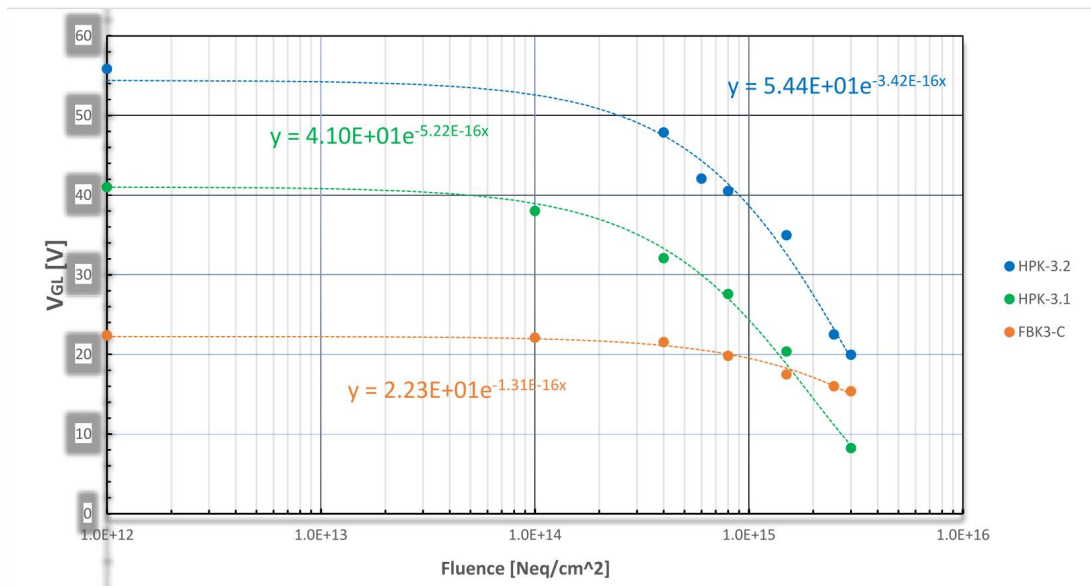
Figure 4.26: Evolution of V_{GL} versus fluence for two HPK LGADs with a deep gain layer and an FBK LGAD with a carbonated gain layer. Taken from [53].
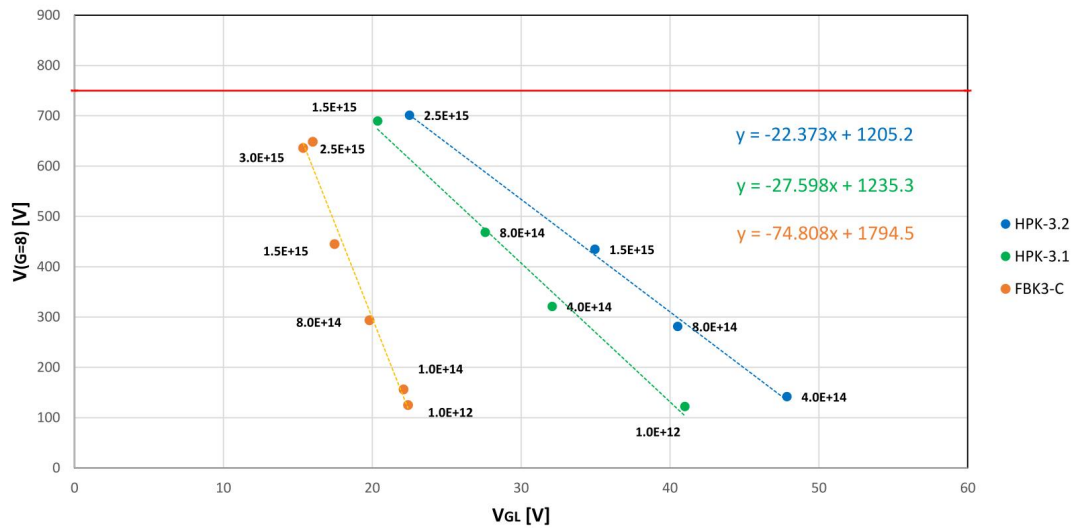
Figure 4.27: Needed bias to reach a gain of $G = 8$ versus V_{GL} for two HPK LGADs with a deep gain layer and an FBK LGAD with a carbonated gain layer after irradiation with different fluences. Taken from [53].

5 Performance of a Prototype T_0 Detector

In this chapter, the experimental set-up used to investigate the timing capabilities of LGADs in combination with different types of discriminator boards will be described. The set-up of a prototype T_0 detector that was tested at the COoler SYnchrotron (COSY) in Juelich with a 1.92 GeV proton beam will be described. As the goal of the beam test at COSY was to study the timing properties of LGADs, the recorded data had to be calibrated. The data calibration as well as the resulting timing precision will be discussed.

In addition, a modified set-up including an AC-coupled LGAD, in literature also called Resistive Silicon Detector (RSD), will be introduced. The modified set-up was tested at higher beam intensities in order to reproduce the timing precision obtained in Juelich and to investigate the rate capability of the set-up as well as the timing properties of an AC-coupled LGAD.

The analysis and calibration of the data recorded during the experiments was performed using the Go4 [55] and ROOT [56] analysis framework.

5.1 Set-Up

The two DC-coupled LGADs used in the prototype T_0 detector were produced in the UFSD2 production run by FBK [37] and are called W3 and W15. While the W3 LGAD featured a gain layer doped with Boron, the gain layer of the W15 sensor was doped with Gallium and an additional low dose of Carbon. Both sensors are 5.0 mm wide and 4.3 mm long, have an active thickness of 50 μm and have a single sided parallel strip geometry with a strip to strip distance of 20 μm and a pitch of 146 μm [6]. However, each detector is far thicker than 50 μm as they are thermally bonded onto a 500 μm thick support wafer [37].

Sensors with the same geometry as the W3 and W15 LGADs were investigated in detail by [57]. A focused 20 keV X-ray beam was used to scan three strips of the sensor in order to investigate the dependence of the gain on position. The result of the scan and its projection onto the x-axis can be seen in Fig. 5.1 (a) and Fig. 5.1 (b) respectively. The measured energy was obtained through a calibration from ADC units and normalized to the measured energy in regions without any gain. As one can see in the pictures, the distance between areas with at least 50 % of the maximum gain is 90 μm. This distance can be slightly reduced by applying a higher bias voltage, resulting in a fill factor of around 55-50 % at gain 20 and 300 V bias [6].

The described LGADs were, with the help of an adapter, mounted on PCBs with two amplification stages close to the sensor. The schematic of the two amplification stages is shown in Fig. 5.2. In

(a)

(b)
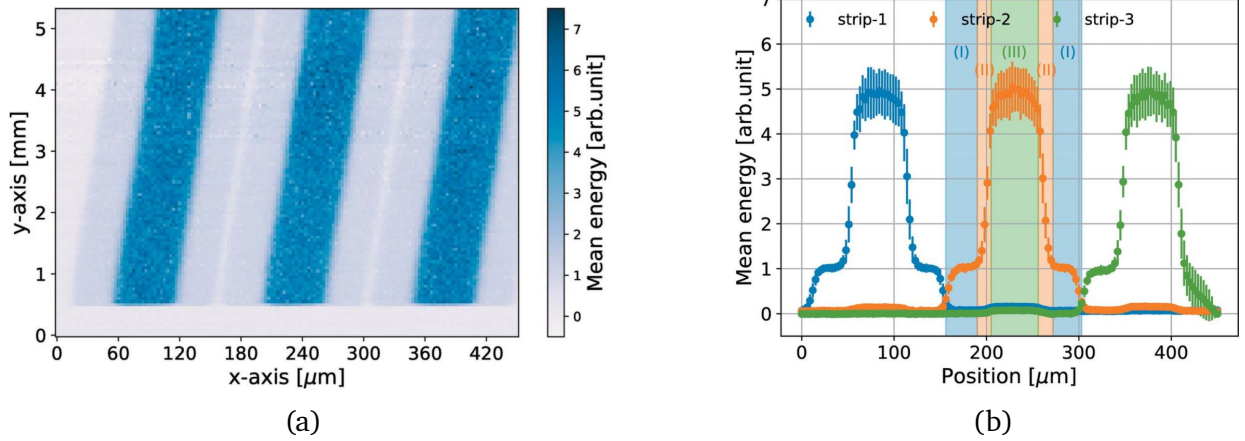
Figure 5.1: Mean energy measured as a function of position measured using focused X-ray beam (a) and its projection onto the x-axis (b). Both taken from [57].

Table 5.1: Connection scheme for the 16 connected channels to the read out electronics.

Discriminator Type	PaDiWa3	NINO	PaDiWa3	NINO	PaDiWa3	NINO	PaDiWa3	NINO
Channel Position	1	2	3	4	5	6	7	8
Channel Number	16	1	15	2	14	3	13	4
Discriminator Type	PaDiWa3	NINO	PaDiWa3	NINO	PaDiWa3	NINO	PaDiWa3	NINO
Channel Position	9	10	11	12	13	14	15	16
Channel Number	12	5	11	6	10	7	9	8

total, each PCB features 32 channels, distributed along four different directions in groups of eight. Of each LGAD, 16 channels, located in the middle of the detectors, were wire bonded onto the PCB and the signals coming from them went through two stages of amplification located close to the sensor on the PCB. After the two amplification stages, the 16 wire bonded channels of each LGAD were connected to either a NINO chip [58] or a PaDiWa3 discriminator board [59] alternately. The detailed connection scheme is shown in Table. 5.1, with the connected channels of the detector numbered from 1-16. Both used discriminators are leading edge discriminators. The Low Voltage Differential Signals (LVDS) coming from the discriminators were read out by the TRB3 platform [60]. The whole LGAD read out scheme is shown in Fig. 5.3. A picture of an LGAD mounted on a PCB can be seen in Fig. 5.4 (a). To realize the prototype T_0 detector, two LGADs were arranged in a telescope setup. The second sensor was rotated by 90° with respect to the other to enable a simultaneous x- and y-position measurement, with z being the beam direction. A picture of the telescope setup is shown in Fig. 5.4 (b). During the experiment, the sensors were not cooled and operated in air. The applied bias was chosen such, that a gain of ~20 was reached in both sensors, resulting in 250 V applied to the W15 LGAD and 300 V applied to the W3 LGAD. A proton beam with an energy of 1.92 GeV, i.e. MIPs (see Fig. 3.7), and a beam intensity ranged from 10^5 to 10^6 protons/s has been used. This beam intensity corresponds to rates between 1-10 Hz per strip [6].
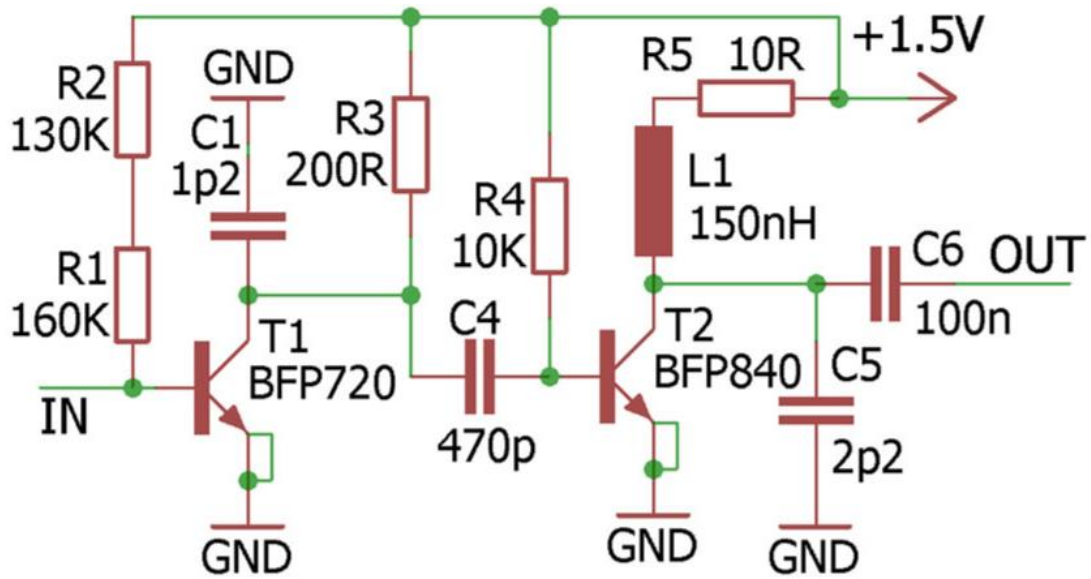
Figure 5.2: Schematic of the two stages of front-end amplification. Taken from [6].
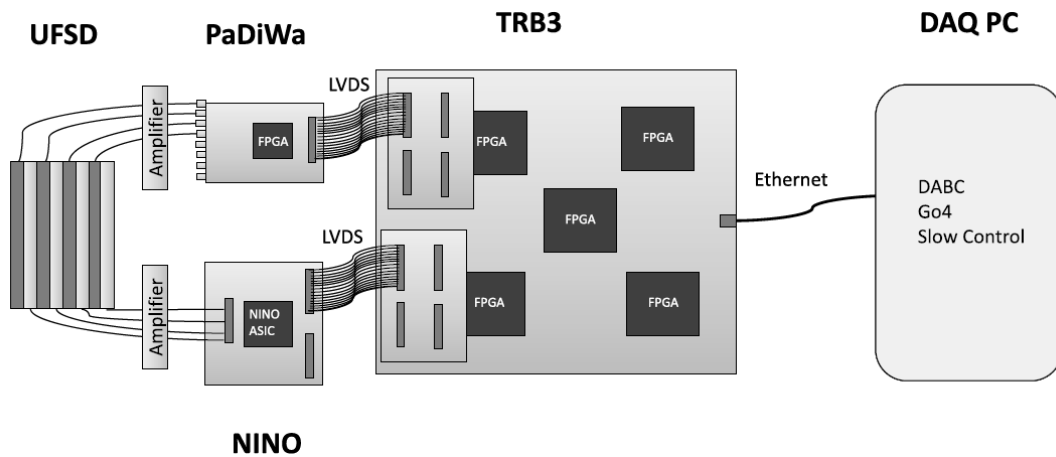
Figure 5.3: Schematic depiction of the readout scheme used in the LGAD set-up. Taken from [12].
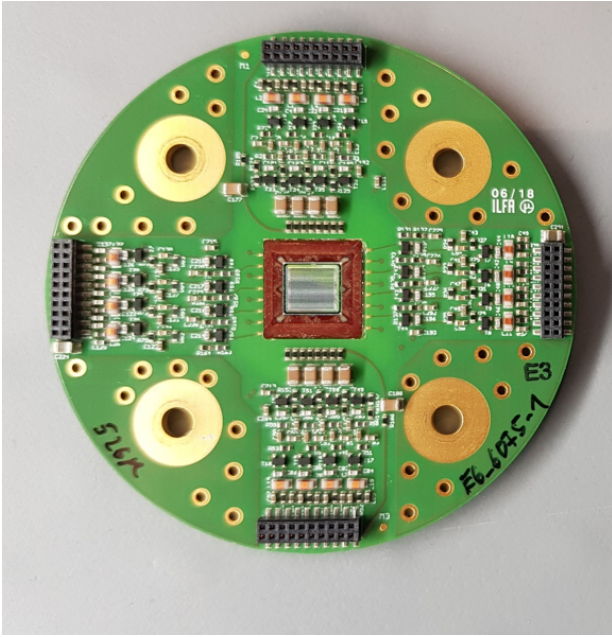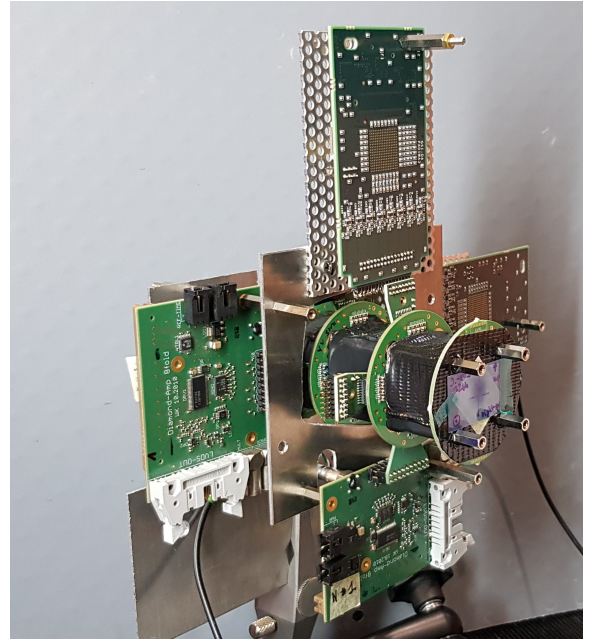
(a)   (b)

Figure 5.4: Photograph of a mounted LGAD on a PCB with two amplification stages close to the sensor (a). Taken from [6]. Photograph of the prototype T_0 detector telescope (b).

5.2 Data Calibration

During the experiments, the leading edge time, or Time of Arrival (ToA), (t_0) and the trailing edge time (t_1) were recorded. The integral of the signal is coded into the width of the signal, which can be obtained by subtracting t_0 from t_1 and is labeled as Time over Threshold (ToT).

In order to evaluate the achievable timing precision of the LGADs the recorded data has to be calibrated. This consists mainly of an ToT dependent correction of t_0 of the signal, as well as offset corrections for each detector strip. In the end of the calibration, cuts on ToT are introduced to discriminate between desired and undesired signals.

To ensure that real particles coming form the beam are measured, the corrections mentioned above are performed with the two detectors in correlation. To be considered in the analysis, a signal has to be detected in detector 1 and detector 2, see Fig. 5.5, in the same event. By subtracting ToA_{Det2} from ToA_{Det1}, the time difference between both detectors (TDiff) can be obtained. Assuming a constant velocity of the particles traversing the detectors, TDiff should be constant, as the distance between the detectors does not change during the experiment. The spread in TDiff represents therefore the timing resolution of both detectors in correlation.

In the following, the calibration procedure will be described using channels connected to NINO discriminators of both detectors (marked yellow in Fig. 5.5).
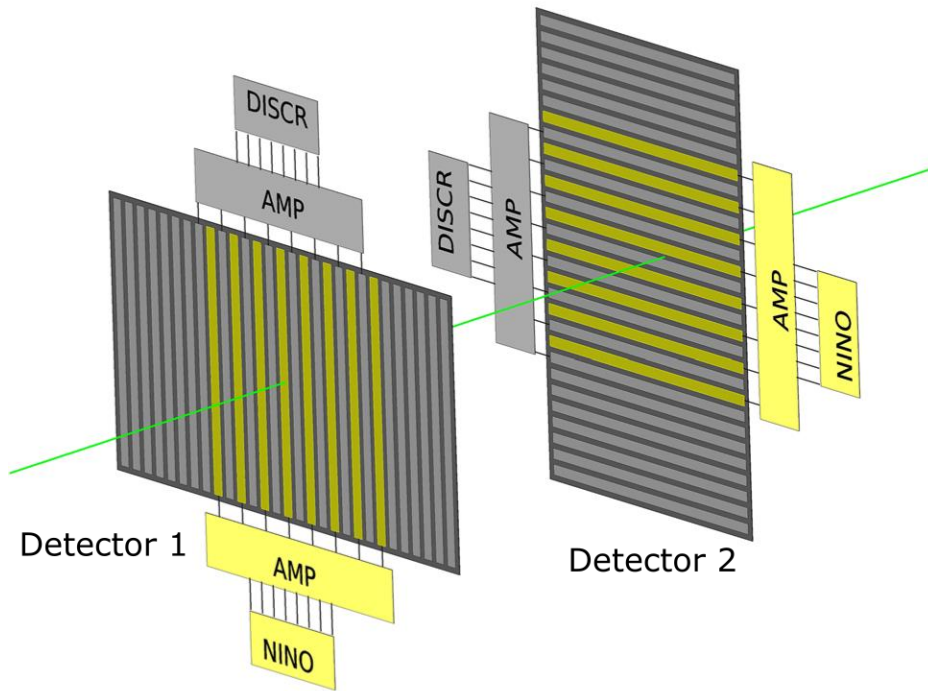
Figure 5.5: Schematic depiction of the detector orientations used in the prototype T_0 detector. Every second readout strip of a sensor is connected to a NINO discriminator (highlighted yellow). Taken from [6].

During the calibration of the data, TDiff versus ToT histograms will be used to illustrate the effects of some calibration steps as well as to extract calibration parameters. To fill these histograms, first a channel in detector 1 and a channel in detector 2 is chosen. As a second choice one has to decide which registered ToT should be plotted. The TDiff versus ToT histograms in the following section show the ToT of channel 2 in detector 1 and the TDiff between channel 2 of detector 1 (ch2_1)and channel 2 of detector 2 (ch2_2). The histograms are filled if both channels detect a signal. The TDiff between the signals is calculated and the histogram is filled in the bin corresponding to TDiff and ToT. For an example of TDiff versus ToT plot, see Fig. 5.7.

5.2.1 Time Difference Calibration

The first calibration step consists of correcting the time offsets of the signals for each used channel. This offset is due to different path lengths of the signals. The correction is done by first choosing one reference channel in the first detector and plotting TDiff to all other channels in the second detector and vice versa. The actual correction parameters are extracted by fitting a Gaussian function to the TDiff distribution between the reference channel and the correlated ones. Using the mean value of the fit, one can perform the correction for the ToA by subtracting the offset. After the time difference calibration, TDiff between both detectors should be, for every channel combination, at zero. In Fig. 5.6 one can see the uncorrected and corrected TDiff distributions.
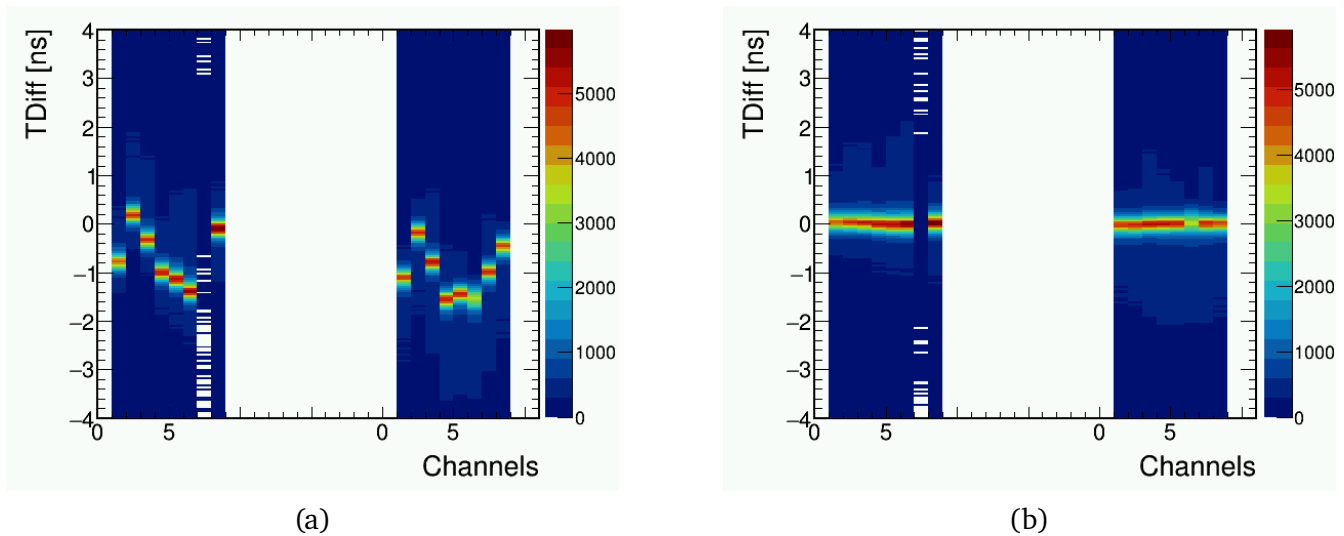
Figure 5.6: Time difference distribution for each channel connected to a NINO discriminator board before (a) and after (b) time difference calibration.

One has to keep in mind that the zero value of TDiff is arbitrarily chosen. However, this does not influence the timing resolution of the detector, as we are only interested in the spread of TDiff.

5.2.2 Time Walk Correction

As mentioned in Sec. 4.2.1, the Time Walk effect arises from amplitude fluctuations and negatively affects the timing resolution of a detector. As can be seen in Fig. 5.7 (a), a strong ToT dependent shift in TDiff of up to 2 ns can be seen for ToT below 15 ns. For larger amplitude signals the effect is not as pronounced, but nevertheless there. As already mentioned, the correction is done offline and consists of parameters generated by Gaussian fits on TDiff for each ToT bin (in 1/3 ns steps). The mean values of the fits were used to correct the ToA dependent on ToT. In Fig. 5.7 (b) the result of the calibration can be seen. TDiff has no clear dependence on ToT anymore.

5.2.3 Time over Threshold to Input Charge Calibration

To translate the measured ToT to a charge induced on the strip, two measurements were taken. The first measurement was done using an oscilloscope connected to an LGAD using a ^{90}Sr source to measure the signal coming directly from it. The area of the resulting signal, which is proportional to the induced charge, was plotted against the amplitude. In Fig. 5.8 (a) the linear dependence of the signal area versus the amplitude can be seen.

The second measurement was done by injecting pulses with a pulser into the NINO discriminator and measuring the resulting ToT. During this measurement we made sure that the width and amplitude of the injected pulses correspond to the width and amplitude relation of signals generated
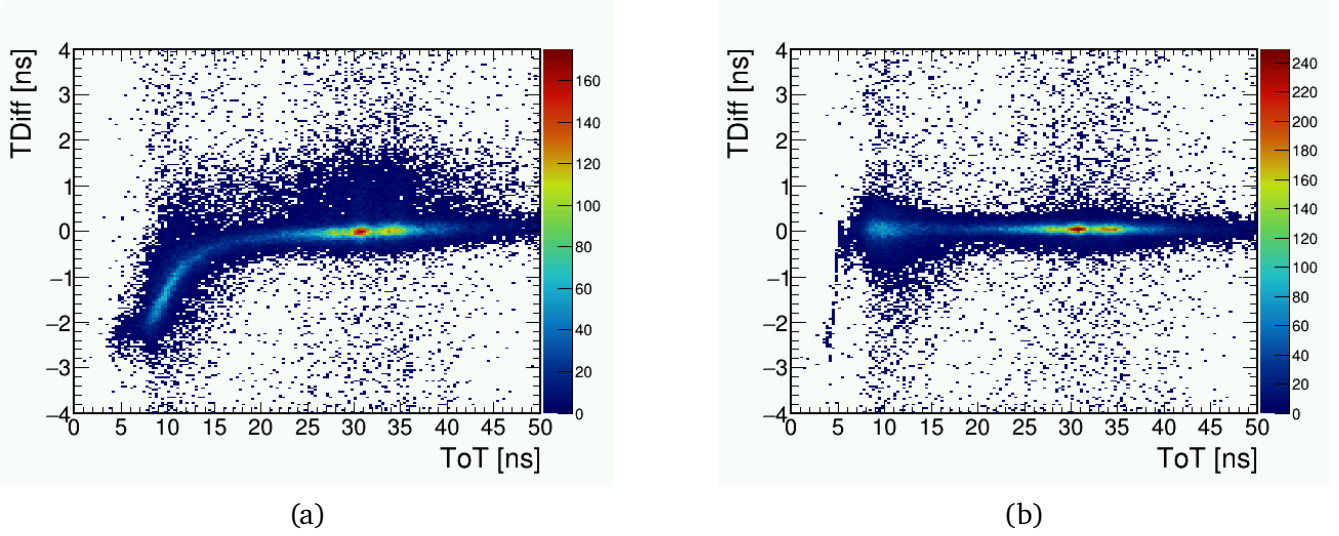
Figure 5.7: Time difference versus ToT for the second channel of detector1 before (a) and after (b) Time Walk correction.

by the detector. Using the proportionality between pulse amplitude and pulse area, as well as the proportionality between pulse area and input charge, the resulting calibration curve can be seen in 5.8 (b). The charge is normalized such, that the expected most probable value (MPV) of the input charge, 10.6 fC (resulting from the most probable energy loss of a MIP in a 50 μm thick detector with gain 20), corresponds to 35 ns ToT. The data in Fig. 5.8 (b) is well described by:

$$
f(x) = \begin{pmatrix} 0 < x < 9.7 & : & 0.04152x \\ 9.7 < x < 39.7 & : & 0.00011053x^3 + 0.00537968x^2 - 0.0207062x - 0.00437408 \\ x > 39.7 & : & 0.804646x - 17.3803. \end{pmatrix} \tag{5.1}
$$

5.2.4 Normalizing the Time over Threshold distributions

Due to the fact that the thresholds for every channel cannot be set to the exact same value, the most probable ToT varies for each channel. As the MPV for the induced charge in a channel does not depend on the chosen channel, ToT has to be normalized to 35 ns for the charge calibration to be valid. The normalization is done by fitting a Gaussian distribution to the ToT spectrum with ToT > 20 ns and multiplying all measured ToT with $35/\mu_{Gaus}$. The resulting normalization and charge calibration can be seen in Fig. 5.9.

5.2.5 Applied Cuts

In Fig. 5.9 not only the prominent signal around 35 ns ToT but also an accumulation of small amplitude signals around 12 ns ($\sim$0.7 fC) can be seen. The small amplitude signals are mainly

| (a) | (b) |
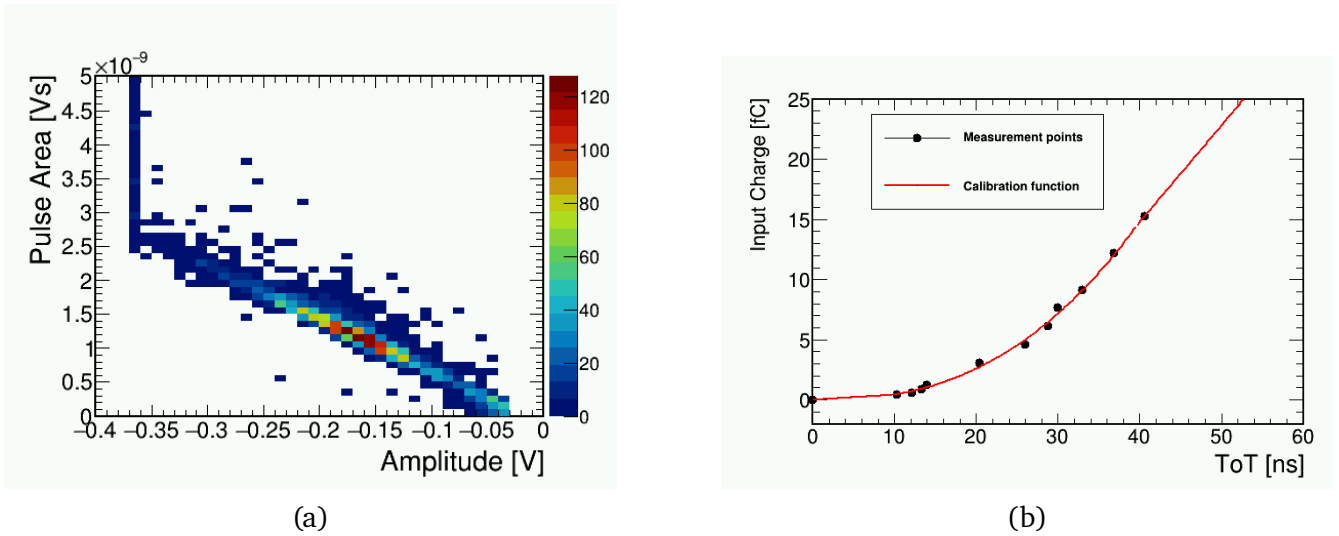
Figure 5.8: Pulse area vs. amplitude of a signal recorded with an LGAD using a ^{90}Sr source (a). Final calibration curve converting ToT to input charge with the calibration function (red curve) given in Eq. 5.1.

coming from a capacitive coupling between the read out strips, as will be discussed later. In a first step, the low amplitude signals from the correlated channel will be removed. The cut consists of removing signals with a ToT outside of the interval 29 ns<ToT<43 ns detected in ch2_2. The resulting TDiff versus ToT distribution can be seen in Fig. 5.10. Compared to Fig 5.9, one can see that the low amplitude signals of ch2_1 are still present, however the smearing in TDiff got less, indicating that the timing resolution got better. To remove the small amplitude signal of ch2_1, two approaches will be presented.

The first approach makes use of the fact that signals, arising from capacitive coupling, are accompanied by higher amplitude signals in one of the neighboring strips and form a signal cluster. By identifying the signal clusters and removing all signals, which have a lower ToT than the highest signal in the cluster, the signals arising from capacitive coupling should be removed. This algorithm is from now on called "cluster removal algorithm" or simply "cluster removal". The resulting TDiff versus ToT plot, after applying the cluster removal algorithm to the data collected from both detectors, can be seen in Fig. 5.11. As one can see, the cluster removal was successful and a significant amount of low amplitude signals got removed. However, not all low amplitude signals got removed, as they can also stem from signals which were not amplified at all or did not get amplified by the full internal gain of the LGAD. Therefore, the second approach consists of the same ToT cut described above, now applied to ch2_1. Additionally, a TDiff cut was performed, such that events with TDiff > 1 ns are disregarded. The result of both cuts applied can be seen in Fig. 5.12 and shows the ToT range used to extract the peak timing precision of the tested LGADs.
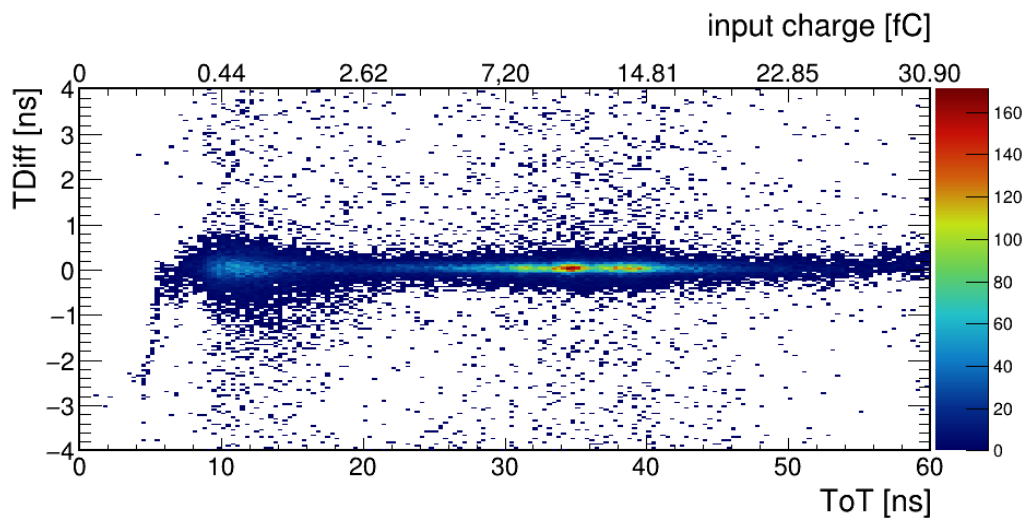
Figure 5.9: Time difference versus ToT histogram for ch2_1 after normalization. The upper axis represents the resulting induced charge on the read out strip.
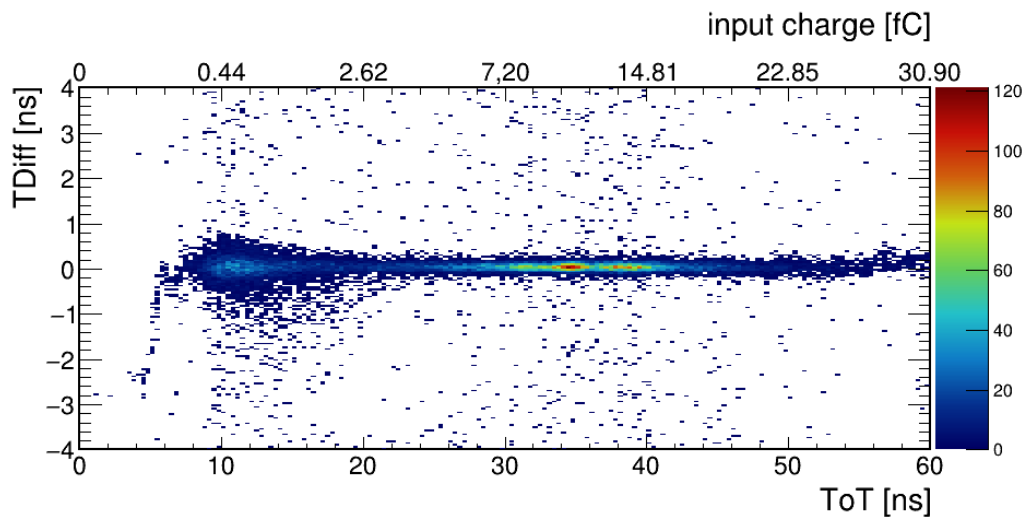
Figure 5.10: Time difference versus ToT histogram for ch2_1 after the cut on ch2_2 described in the text.
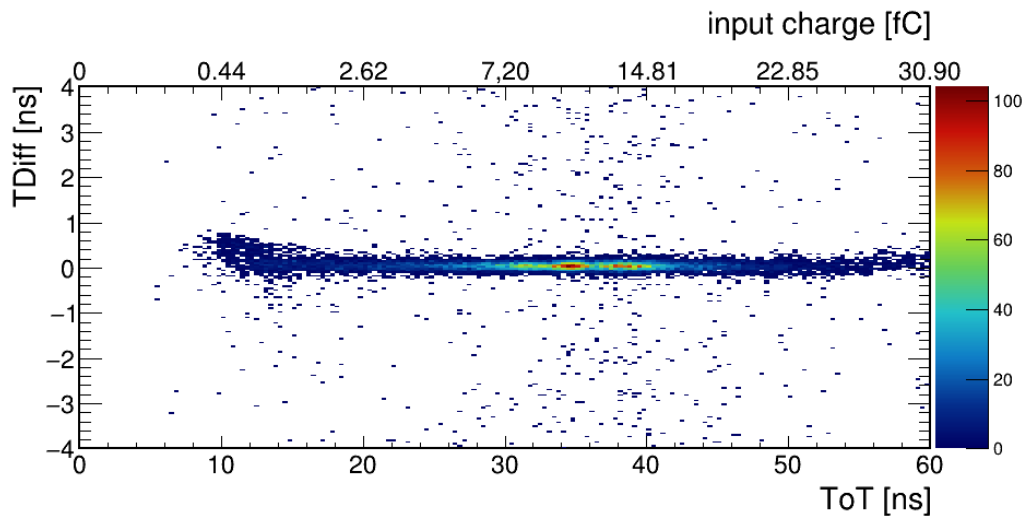
Figure 5.11: Time difference versus ToT histogram for ch2_1 after applying the cluster removal algorithm.
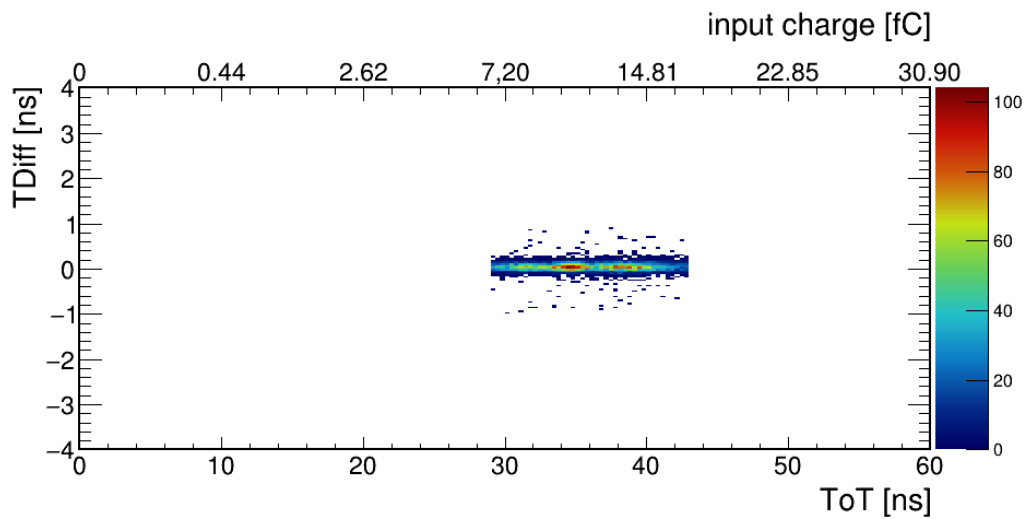
Figure 5.12: Time difference versus ToT histogram for ch2_1 after the cut on ch2_1 described in the text.

5.3 Discussion and Results

In this section the cuts applied in Sec. 5.2.5 will be motivated by showing that the signals indeed come from capacitive coupling between the read out strips. The influence of each cut on the timing precision will be shown and discussed. In the end the timing precision of the set-up will be shown for channels connected to NINO and PaDiWa3 separately.

5.3.1 Capacitive Coupling

In Sec. 5.1 it was mentioned that the wire bonded channels of the used LGADs were alternately connected to NINO and PaDiWa3 discriminator boards. This was done in order to prevent cross talk in the read out electronics. However, investigations showed a clear correlation between signals in a readout strip and its two closest strips. This correlation can be clearly seen in Fig. 5.13 where a reference channel of detector 1 (y-axis) is clearly correlated to two channels of the same detector. Such a strong correlation is not present for all other channels.

The strong correlation between the three read out strips is investigated by plotting the cluster size of the three strips, i.e. how many of these read out strips registered a signal above threshold, versus the ToT of the middle strip. In Fig. 5.14 (a) this kind of histogram is shown. The middle strip is chosen to be ch2_1 (see Table 5.1). One can distinguish between five different regions in this plot. Region one (1) is characterized by lower amplitude signals up to 28 ns ToT and a cluster size of one. Those are signals which do not arise from capacitive coupling between the readout strips but are
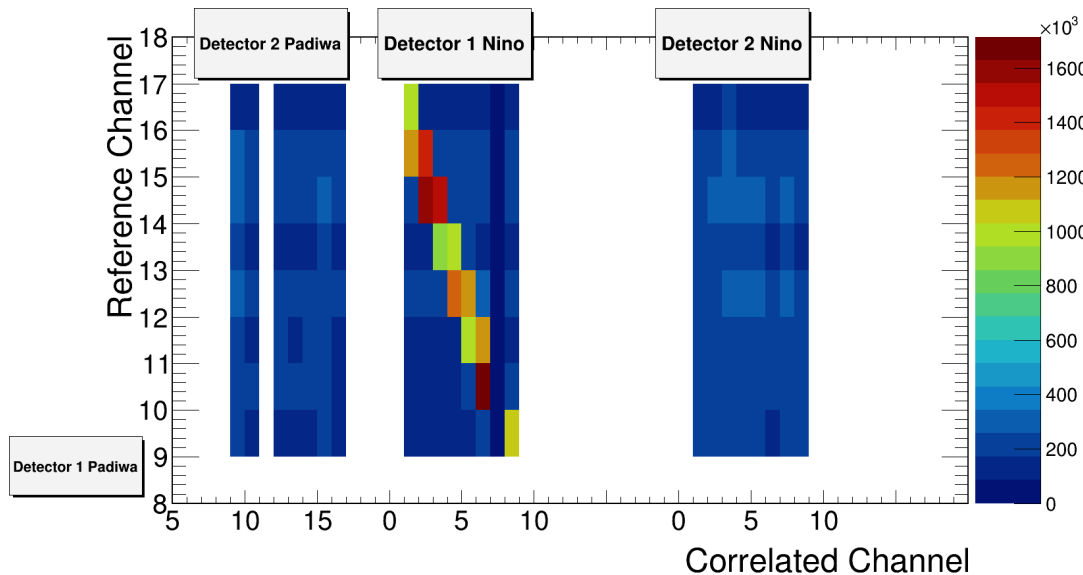
Figure 5.13: Correlation between channels. Channels 9-16 of detector 1 are taken as a reference. A clear correlation between neighboring channels on the same detector can be seen.

rather signals which did not get amplified by the full gain or did not get amplified at all, compare region I (blue) and region II (orange) in Fig. 5.1 (b). Regions (2), (3) and (4) are characterized by high amplitude signals starting from 28 ns ToT up to above 50 ns with a cluster size of one, two and three respectively. For these regions one can see a stepwise increase in cluster size for increasing ToT, indicating that the thresholds of the discriminators connected to the adjacent strips are not set to the exact same value.

The last region with distinctive features is region (5), with low ToT (∼15 ns) and a cluster size of two. Signals lying in region (5) are caused by capacitive coupling, when the signal of one of the adjacent strips lies in region (3) or (4). This can be verified by applying the local maximum condition, as explained in Sec. 5.2.5, to the histogram. The effect on this condition can be seen in Fig. 5.14 (b). As one can see, the amount of signals in region (5) got significantly reduced, meaning that a signal with a bigger ToT was found in one of the adjacent strips.

In the investigated LGADs capacitive coupling of a strip to an adjacent strip of about 5 % is expected [6]. This is consistent with the measured charge of signals caused by capacitive coupling (region (5)) and signals inducing, through capacitive coupling, signals above threshold in adjacent strips (regions (3) and (4)). Coincidentally, the created charge corresponding to signals which where not amplified by the internal gain of the LGADs is also around 5 % of the created charges corresponding to signals subject to full gain, as the gain is set to be 20. Therefore the residual signals in region (5) can be interpreted as chance coincidences between non amplified signals, signals caused by capacitive coupling or a combination of both.

In Fig. 5.15 the ToT measured in a channel of detector connected to the PaDiWa3 discriminator versus the ToT measured in the adjacent strip, connected to the NINO discriminator, is shown. The histogram is filled when both strips measured a signal above threshold with a detector intern time difference below 10 ns in the same event. One can see a clear correlation between big signals in NINO and small signals in PaDiWa3 and vice versa. This reinforces the capacitive coupling argumentation

(a)   (b)
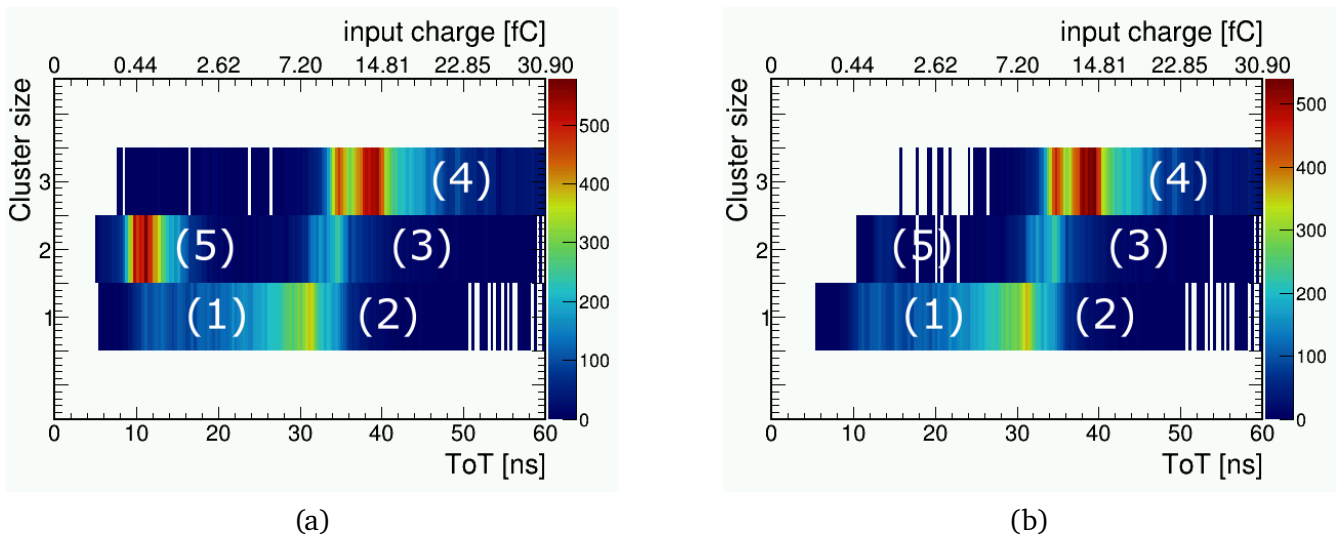
Figure 5.14: Cluster size of a subset of three readout strips, consisting of ch2_1 and its two adjacent strips, versus ToT of ch2_1 (a). The same as in (a), but with the condition that ch2_1 should be a local maximum (b).
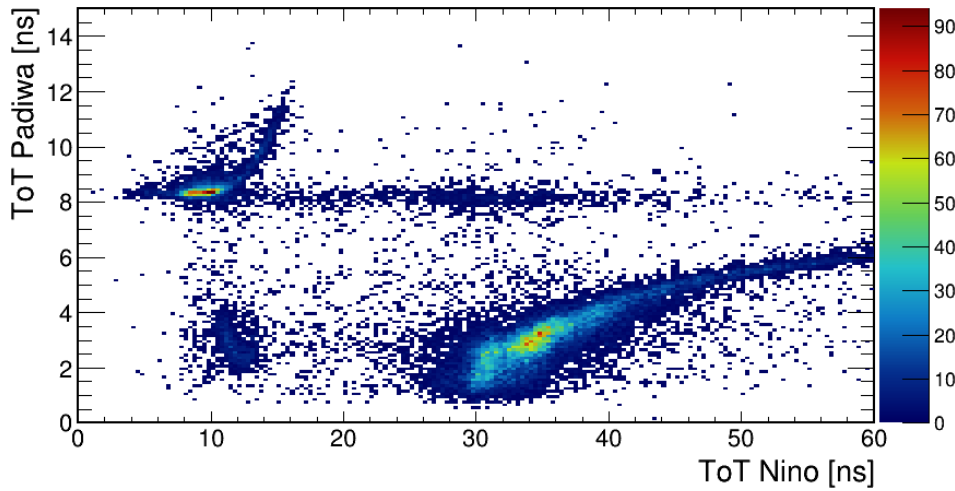
Figure 5.15: ToT of ch2_1 (x-axis) and one of its adjacent strips (y-axis).

and justifies the cuts on low signals as they either arise from capacitive coupling or were subject to only a part of the full gain.

5.3.2 Calibration steps

In this section the influence of the applied cuts and cluster removal on the ToT distribution of ch2_1 and the timing precision of the channel will be discussed. These calibration steps need to be discussed as they change the statistics of the analyzed signals and one needs to make sure that cuts on ch2_2 do not influence the ToT spectrum of ch2_1 in a surprising manner. The ToT distribution for ch2_1 is shown in Fig. 5.16 (a) and the corresponding ration, normalized to the distribution after the cut on the correlated channel ch2_2, is shown in Fig. 5.16 (b). It is acquired through projections of TDiff versus ToT histograms shown in Sec. 5.2 onto the x-axis. The naming convention used in the legend is based on the order the cuts were introduced in Sec. 5.2.5. Step0 corresponds to no cuts, step1 to the cut on ch2_2, step2 to applying the cluster removal algorithm to ch2_1 and step3 to the final cut done on the ToT spectrum of ch2_1. The substructure in the ToT distribution, especially noticeable around 35 ns ToT, in the form of a triple peak structure could be due to high frequency noise, to which ToT measurements are especially sensitive [61].

In Fig. 5.16 (b) one can see that step1 only reduces statistics, as ch2_1 is correlated with less events of ch2_2 as a result of the cut. This is shown by the black curve, which is a flat distribution around 1.75, signaling a reduction of statistics around ∼40-50 %, but no change in the spectrum characteristics. The cluster removal shows, as already seen in Sec. 5.2.5, a strong suppression only of low amplitude signals, whereas the final cut removed all contributions outside the cut interval.

In Fig. 5.17 (a) the timing precision versus ToT for each ToT bin of ch2_1 is shown. The naming convention is the same as above. One can see that the first calibration step clearly improves the achieved timing resolution for every ToT, as was already indicated by the reduced smearing in ToT in Fig. 5.10 compared to Fig. 5.9. After cluster removal, statistics for low ToT was very poor, which
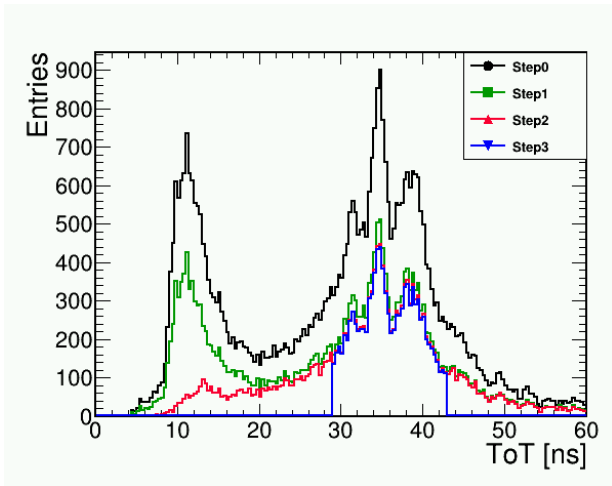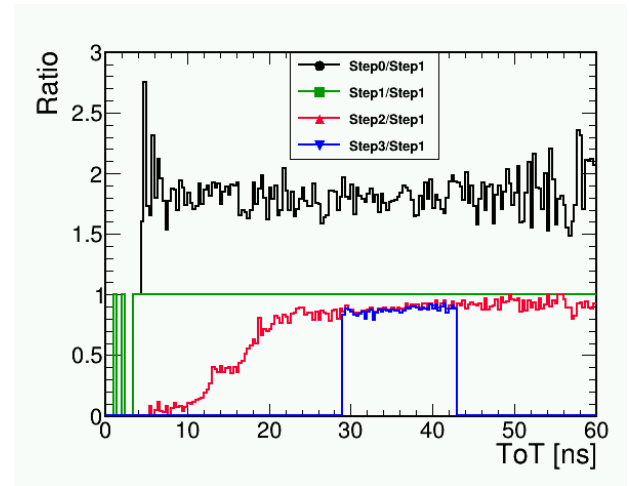
Figure 5.16: ToT distribution of ch2_1 after different calibration steps (a) and the ratios to the distribution corresponding to step1 (b). The legend is described in the text.
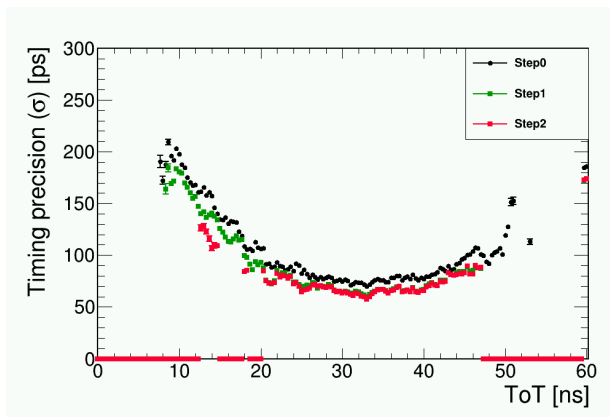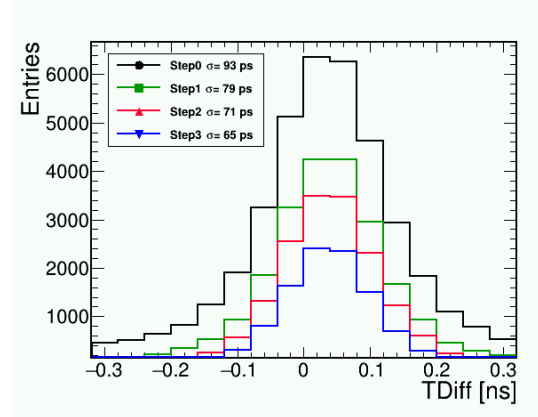
Figure 5.17: Timing precision versus ToT for ch2_1 after the first two calibration steps (a) and the total timing precision of ch2_1 after different calibration steps. The legend is described in the text.

is the reason for missing timing precision at low ToT. However, the difference to step1 is very low for intermediate to high ToT. Additionally, one can see a broad valley marking the ToT region where the timing precision is most optimal. This valley reinforces the cut intervals chosen.

In Fig. 5.17 (b) the timing precision reached for ch2_1 after each calibration step is shown. The timing precision was extracted from Gaussian fits to the projections of TDiff versus ToT histograms, as shown in Sec. 5.2 onto the TDiff-axis. One can see that every calibration step improves the timing resolution reached with ch2_1.

5.3.3 Timing Performance

The timing precision of the T_0 prototype detector presented here has to be split into the performance reached by using the NINO or the PaDiWa3 discriminator. We extracted the timing precision from Gaussian fits to the projections of TDiff versus ToT histograms (after full calibration), like the one shown in Sec. 5.12 onto the TDiff-axis. This was done for every channel of detector1 correlated with one channel, connected to the same discriminator type, of detector2 and the results can be seen in Fig 5.18. A constant fit to the resulting timing precisions per channel was done to get a value for both detectors. As all timing precisions were reached by two LGADs in correlation, the average value has to be divided by $\sqrt{2}$ to get the timing precision of one detector. Therefore, the single channel timing precision achieved with the NINO discriminators is around $66.8/\sqrt{2} \approx 47.2$ ps and with the PaDiWa3 discriminators a single channel timing precision of about $94.5/\sqrt{2} \approx 66.8$ ps was reached.

PaDiWa Performance

In Fig. 5.19 one can see the TDiff versus ToT plot of a channel connected to a PaDiWa3 discriminator before (a) and after a full calibration, without normalization and the last ToT and TDIff cut (step3), (b). One can see that the majority of the signals is closely spread around 8 ns ToT. This small spread in ToT reduced the effectiveness of the Time Walk calibration and therefore influenced the resulting timing precision. The different performance of the PaDiWa3 discriminator boards could be caused by an additional amplification integrated into the PaDiWa3 boards that were used during the experiment. Due to the additional amplification signals saturate early, leading to a worse signal to noise ratio, as noise does not saturate. Another effect could be a saturation in the signal width, causing a lot of signals to have the same short width of about 8 ns, reducing the precision improvement gained by the Time Walk correction.
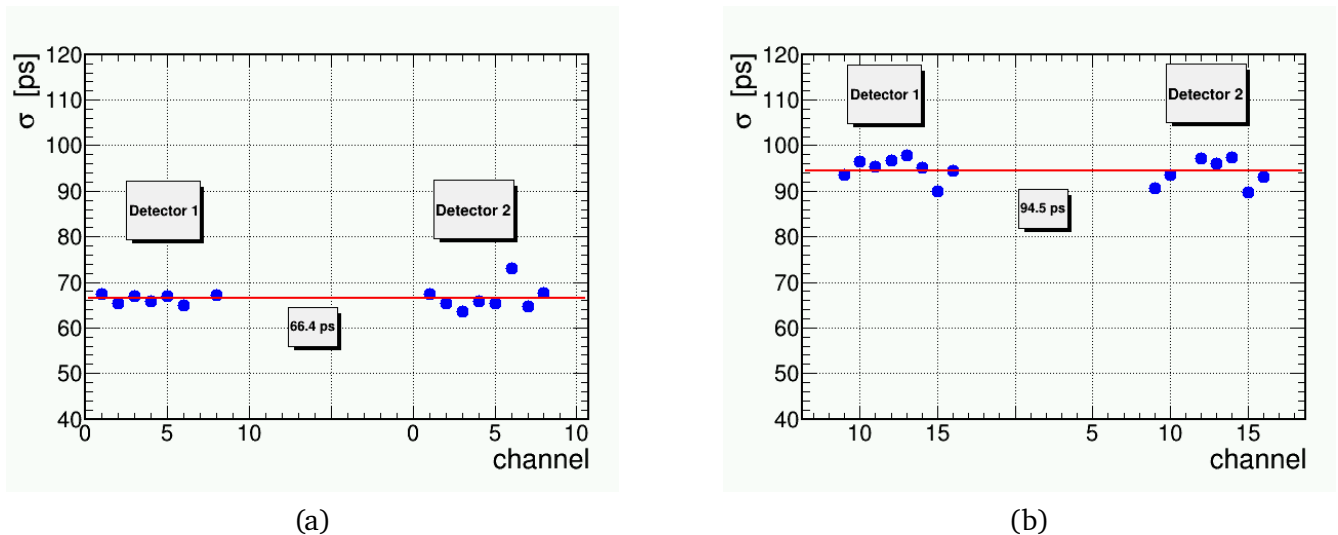
Figure 5.18: Timing performance reached in the experiment at COSY with a 1.92 GeV proton beam for both detectors for NINO (a) and PaDiWa3 (b) discriminator boards.
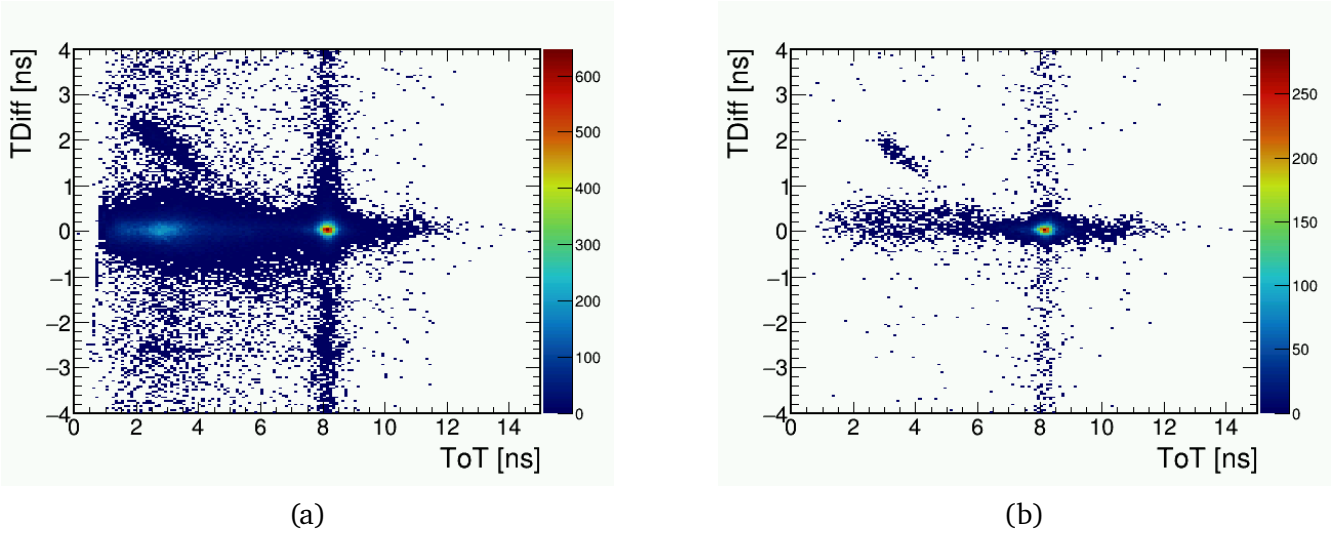
Figure 5.19: ToT versus TDiff histogram for channel 15 of detector 1 (connected to a PaDiWa3 discriminator) after Time Walk calibration (a) and after full calibration (b).

5.4 Tests of LGAD at GSI

A similar set-up as described in Sec. 5.1 was studied at the SIS18 synchrotron at GSI in Darmstadt. The set-up was modified and an AC-coupled LGAD was put in between the two DC-coupled LGADs. The used AC-coupled LGAD has a parallel multi-strip geometry with 1 cm long strips and the strip orientation was parallel to the strip orientation of the first detector (W3). A photograph of it mounted on a PCB is shown in Fig. 5.20. As an LGAD technology with a fill factor close to one, the timing performance of it was investigated. Eight channels in the middle of the detector were wire bonded onto a PCB with two amplification stages close to the sensor. After the amplification stages a NINO discriminator was connected in order to achieve the best possible timing precision. Except from this additional LGAD, no other changes to the set-up were made. The set-up, now consisting of three LGADs, was again operated in air without additional cooling. A 2.5 GeV proton beam was delivered by the SIS18 synchrotron and signal rates between 0.5 MHz and 1.2 MHz per channel were observed. The applied biases were 400 V to the AC-coupled LGAD, 250 V to the LGAD of type W3 and 200 V to the LGAD of type W15. This means that the gain of the DC-coupled LGADs was lower than in the experiment at COSY, described in Sec. 5.1.

5.4.1 AC-coupled LGAD Performance

In order to analyze the performance of the AC-coupled LGAD, again TDiff versus ToT histograms were made. For this, the last detector (W15) was correlated with the AC-coupled LGAD. In Fig. 5.21 (a) the TDiff versus ToT histogram after Time Walk correction, can be seen. After applying a cut on the correlated channel and on the channel of the AC-coupled LGAD, a timing precision of around 182 ps
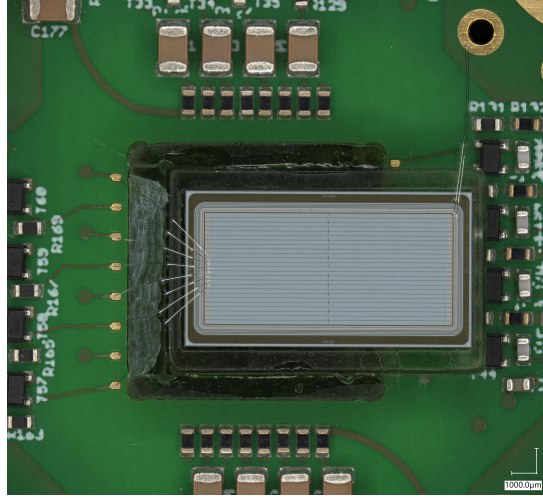
Figure 5.20: Close-up picture of the used AC-coupled LGAD after being mounted and wire bonded to a PCB.

could be extracted, see Fig. 5.21 (b). However, this time the resulting precision cannot be divided by $\sqrt{2}$, as the precision of the correlated LGAD (W15) is significantly better. Taking the precision of the W15 LGAD into account one reaches a timing precision of:

$$\sigma_{AC-LGAD} = \sqrt{(182\ ps)^2 - (89.5\ ps/\sqrt{2})^2} \approx 170.6\ ps. \tag{5.2}$$

5.4.2 DC-coupled LGAD Performance

One of the goals of the experiment at SIS18 was to reproduce the excellent timing performance below 50 ps achieved with LGADs at COSY in Juelich. The timing precision was obtained, after full calibration, in the same way as described in Sec. 5.3.3. In Fig. 5.22 (a) and (b) one can see the timing precision obtained for each channel connected to a NINO discriminator and a PaDiWa3 discriminator respectively. Additionally, a constant was fitted to the data to obtain a value for both detectors. The obtained timing precisions are: $\sigma_{NINO} =$89.5 ps/$\sqrt{2} \approx 63.3$ ps and $\sigma_{PaDiWa} =$109.4 ps/$\sqrt{2} \approx$77.4 ps. The worse performance compared the COSY experiment can be attributed to the lower applied bias voltage and therefore a lower gain of the LGADs. Future investigations will address these issues in detail.
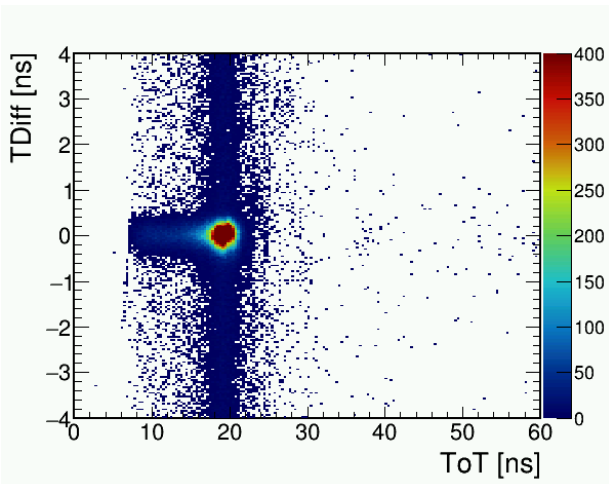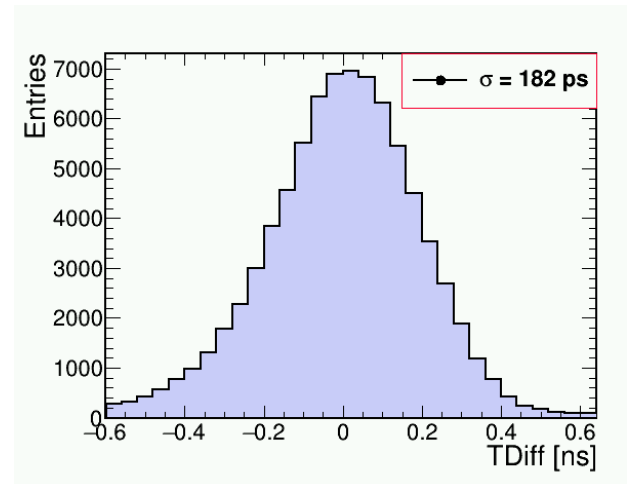
(a)   (b)

Figure 5.21: TDiff versus ToT histogram for a channel of the AC-coupled LGAD connected to a NINO discriminator, in correlation with a DC-coupled LGAD, (a) and the resulting timing precision after calibration (b). The device was tested at SIS18 with a 2.5 GeV proton beam.
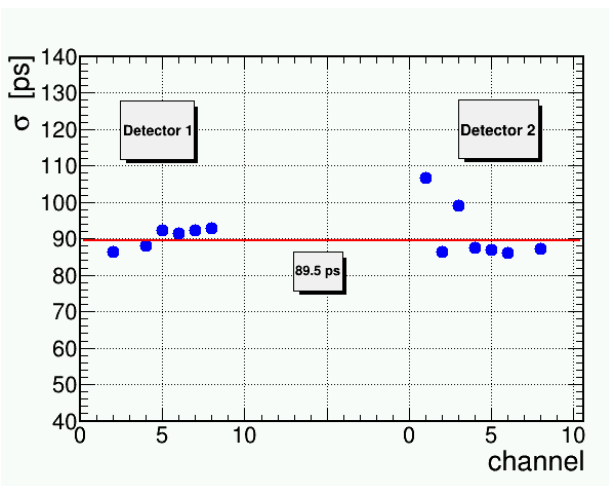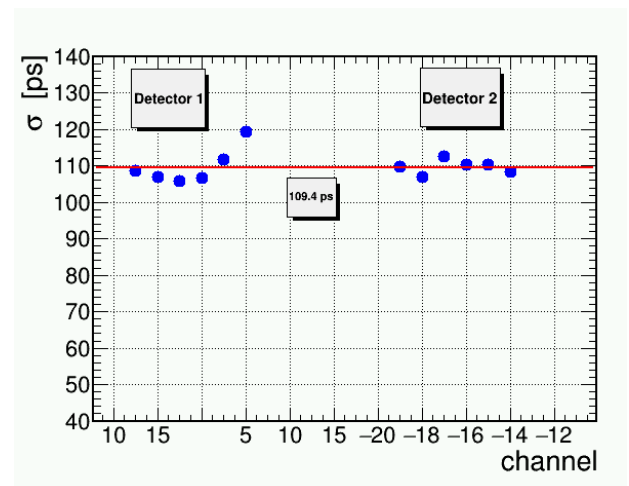
(a)   (b)

Figure 5.22: Timing performance reached in the experiment at SIS18 with a 2.5 GeV proton beam with DC-coupled LGAD detectors, for NINO (a) and PaDiWa3 (b) discriminator boards.

6 PaDiWa Board Parameter Studies

In order to investigate the saturation of the measured ToT when using PaDiWa3 discriminators, a parameter study was conducted. For the study the DC-coupled LGADs W3 and W15 were used, again arranged behind each other and with a 90° rotation of the second sensor. The connections to the read out electronics are the same as described in Sec. 5.1. However, to reduce noise and ringing in the set-up, only one discriminator per sensor was connected. This made cluster size studies impossible, as every second strip was not read out. The study was performed using a ^{90}Sr source. The detectors were placed in a light-tight box together with the source. To have a reference timing precision, first NINO discriminators were connected and data was recorded as well as calibrated and analyzed. In the second part of the study PaDiWa3 boards were modified and the TDiff versus ToT spectra as well as the resulting timing precision were studied. Additionally, a PaDiWa4 discriminator board was tested, as PaDiWa4 discriminators do not have a built in amplification. The PaDiWa4 board was modified as well, in order to study the effects of the modification.

6.1 NINO Reference Measurement

In Fig. 6.1 (a) the TDiff versus ToT histogram of a channel connected to a NINO discriminator is shown. The correlated channel was also connected to a NINO discriminator to prevent any possible distortion caused by PaDiWa boards. A bias of 250 V and 200 V was applied to the W3 and W15 sensor respectively. The timing precision was extracted as already described in the Sec. 5.3.3 and amounted to σ_{NINO}=93 ps/$\sqrt{2}$ =65.8 ps.
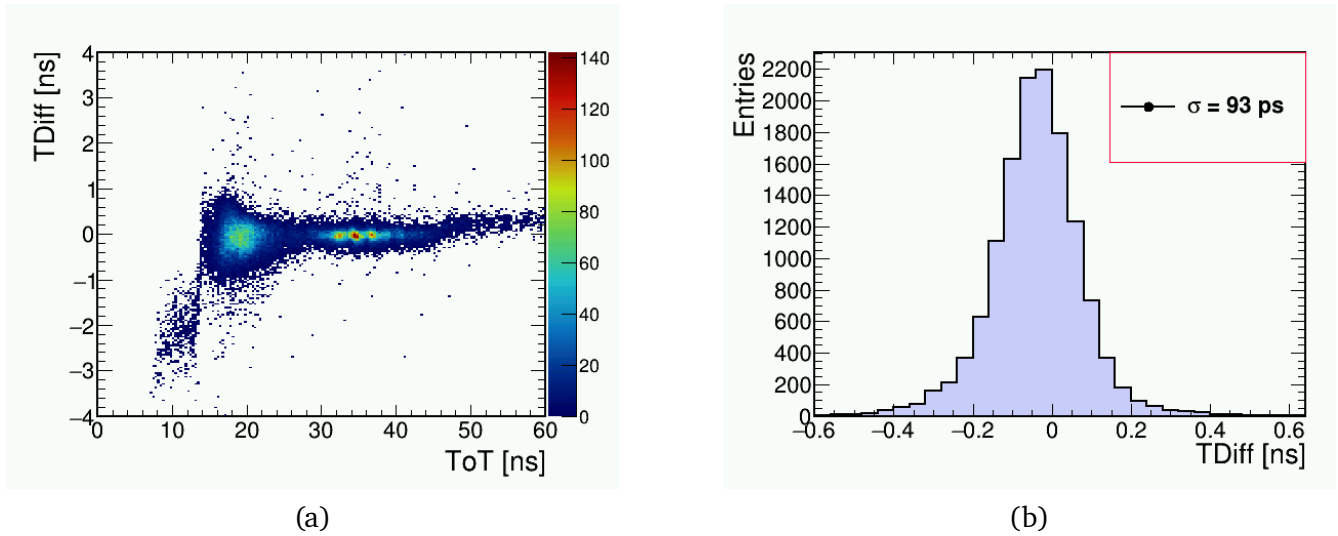
Figure 6.1: TDiff versus ToT histogram for a channel connected to a NINO discriminator and the resulting timing precision after calibration (b). The experiment was performed using two DC-coupled LGADs and a ^{90}Sr source.

6.2 PaDiWa3 Modifications and Timing Precision

In Fig. 6.2 the schematics of the analog part of a channel of a PaDiWa3 discriminator is shown. The two boxed components (black and green) are the components which were modified in some channels. The first modification done was by changing the green boxed capacitance to 10 nF and to 100 nF. However, these modifications did not show any significant effect. In a next step the black boxed capacitance was replaced by capacitances of 100 pF (mod3.1), 300 pF (mod3.2) and 1 nF (mod3.3), with mod3.0 being the unmodified PaDiWa3 board. The effects of the modifications can be seen in Fig. 6.3, which shows TDiff versus ToT spectra on the left side and the corresponding timing precision after cuts on the right side.

As one can see, replacing the capacitance increased the measured ToT from around 8 ns for mod3.0 to 18 ns for mod3.3. However, the achieved timing precision gets significantly worse for high capacitances, from σ_t=127 ps/$\sqrt{2}$ =89.8ps for mod3.0 to σ_t=175 ps/$\sqrt{2}$ =123.7ps for mod3.3. This lead to the conclusion that in order to achieve an optimal timing precision with PaDiWa3 discriminator boards, no modifications should be done.
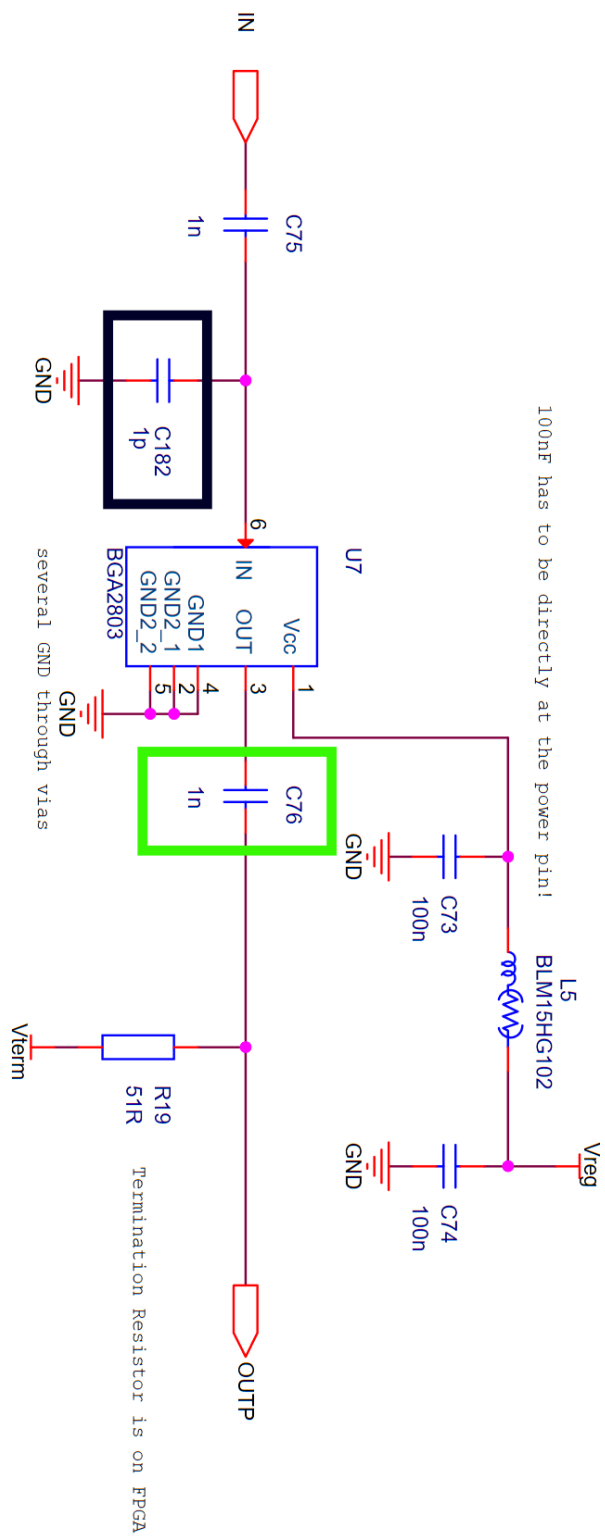
Figure 6.2: Schematics of the analog part of a channel from a PaDiWa3 discriminator board. Taken from [59].
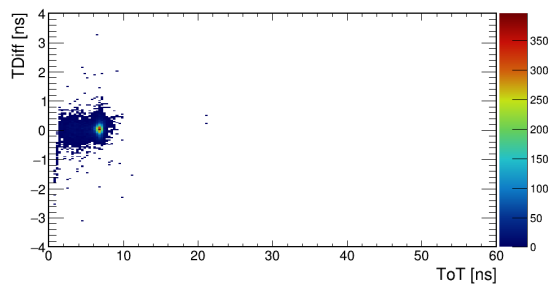
(a)
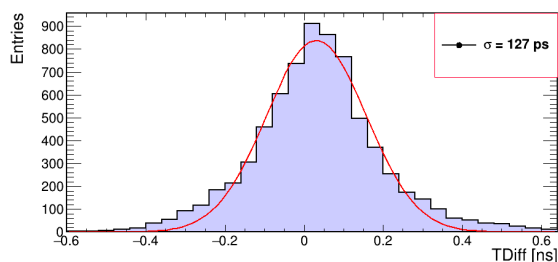
(b)
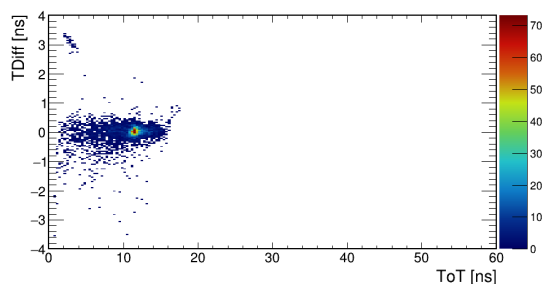
(c)
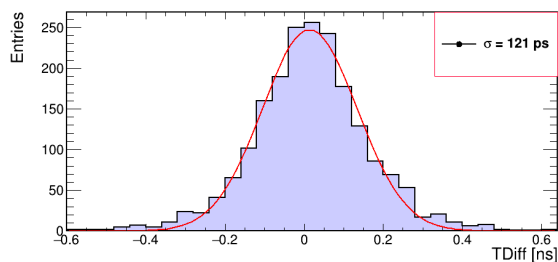
(d)
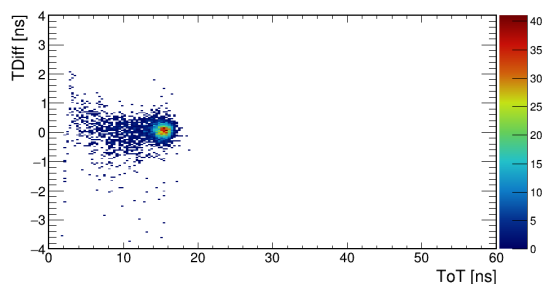
(e)
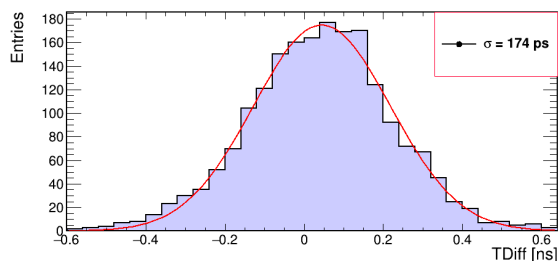
(f)
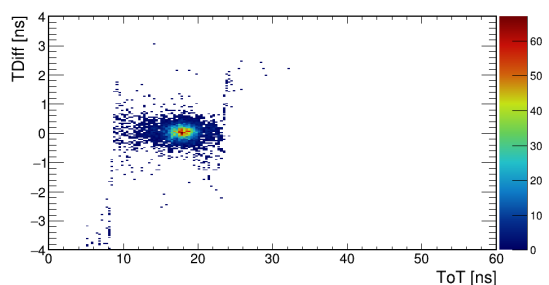
(g)
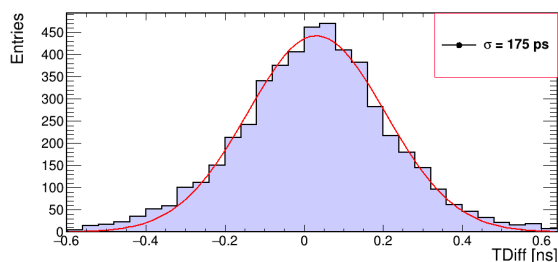
(h)

Figure 6.3: TDiff versus ToT histogram for channels connected to a PaDiWa3 discriminator board with modification mod3.0 (a), mod3.1 (c), mod3.2 (e), mod3.3 (g) and the resulting timing precision after calibration (b), (d), (f) and (h), respectively. The experiment was performed using two DC-coupled LGADs and a ^{90}Sr source.

6.3 PaDiWa4 Modifications and Timing Precision

As the difference in the ToT distribution of signals read out by the PaDiWa3 discriminator board was attributed to the gain in the PaDiWa3 board, PaDiWa4 discriminator boards were tested. The PaDiWa4 discriminator board is very similar to the PaDiWa3, except that no amplification is built in and it has an overvoltage protection [59]. Modifications to some channels of the PaDiWa4 board were done in two steps. First, the green boxed 50 Ω resistor, see Fig. 6.4, was replaced by a 75 Ω resistor (mod4.1). In the second step, the in Fig. 6.4 black boxed diode and capacitances were removed and a resistor (green boxed) with 50 Ω (mod4.2) and 75 Ω (mod4.3) were used. An unmodified PaDiWa4 channel corresponds to mod4.0. The effects of the modifications can be seen in Fig. 6.5, which shows TDiff versus ToT spectra on the left side and the corresponding timing precision after cuts on the right side.

Exchanging the resistor had a similar effect as for the PaDiWa3 boards: the measured ToT spectrum got shifted to slightly higher ToT. The MPV for ToT shifted from ∼8 ns for mod4.0 to ∼10 ns for mod4.1, with a slight change in timing precision from σ_t=126 ps/$\sqrt{2}$ =89.1ps for mod4.0 to σ_t =129 ps/$\sqrt{2}$ =91.2ps for mod4.1.
The modifications mod4.2 and mod4.3 showed a larger influence on ToT spectrum. For mod4.2 even a separation between low ToT and higher ToT, similar to the case using the NINO discriminator, see Fig. 6.1, is visible. However, due to the low statistics and non performable cluster studies, it is not possible to say whether the low amplitude signals are coming from capacitive coupling or not and where exactly to perform the cuts during calibration. This resulted in a loose cut, ranging from 7.7 ns<ToT<24 ns. Mod4.2 and mod4.3 delivered slightly better performances with respect to timing precision, with the best performance reached with mod4.2 at σ_t=118 ps/$\sqrt{2}$ =83.4ps.

An investigation was done to ensure that the high ToT signals seen for mod4.2 and mod4.3 were not due to an error during data taking. For this, the number of leading and trailing edges per event was analyzed and is shown in Fig. 6.6 for mod4.2. Because ToT is calculated as the difference between the recorded trailing edge timing and leading edge timing, a missing leading edge could result in distortions in the ToT distribution. As one can see in Fig. 6.6, in the vast majority of events with signals in a channel connected to mod4.2 one leading and one trailing edge were recorded. Therefore it was concluded that the high ToT signals were not due to a missing leading edge.
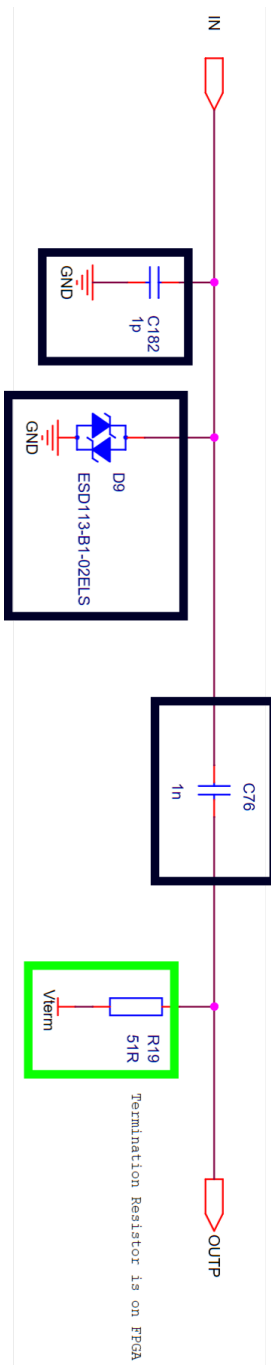
Figure 6.4: Schematics of the analog part of a channel from a PaDiWa4 discriminator board. Taken from [59].
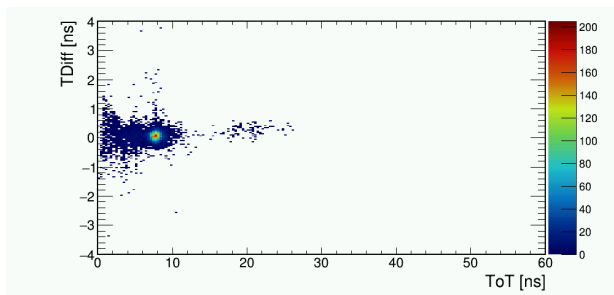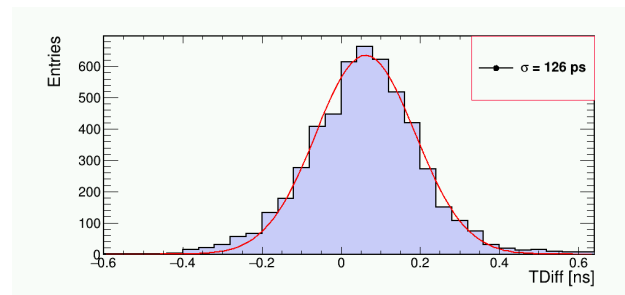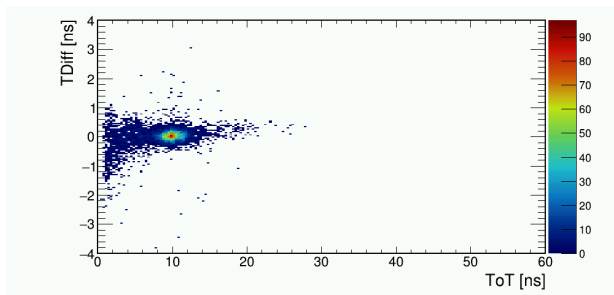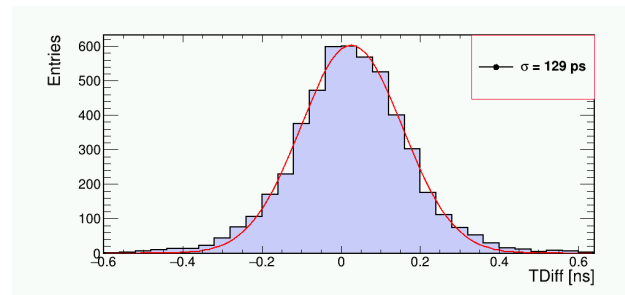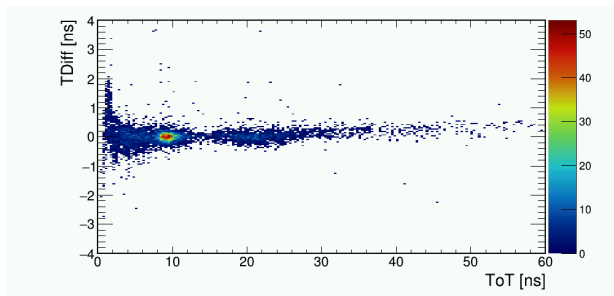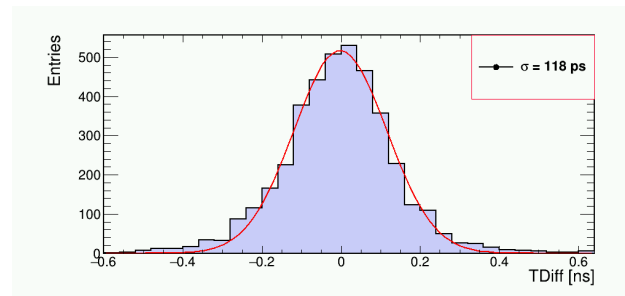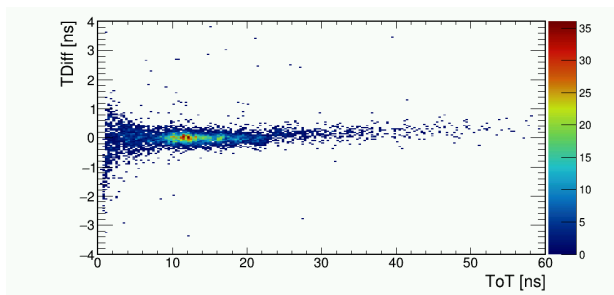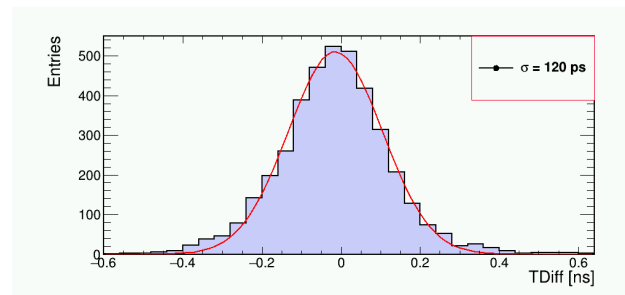
Figure 6.5: TDiff versus ToT histogram for channels connected to a PaDiWa3 discriminator board with modification mod4.0 (a), mod4.1 (c), mod4.2 (e), mod4.3 (g) and the resulting timing precision after calibration (b), (d), (f) and (h), respectively. The experiment was performed using two DC-coupled LGADs and a ^{90}Sr source.
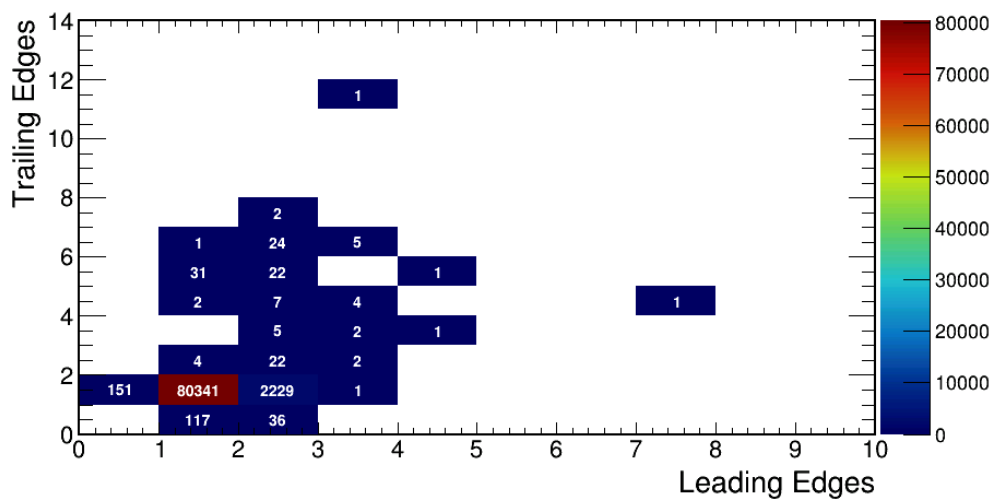
Figure 6.6: Number of trainling edges versus number of leading edges recorded per event for a readout strip connected to a PaDiWa4 board, with mod4.2.

7 Summary and Outlook

In this document, the working principles of LGADs and their timing precision and radiation hardness were introduced. The calibration process including the Time Walk correction, a cluster removal algorithm and applied cuts on ToT were described and motivated. A timing precision of $\sigma_t \approx 47$ ps has been demonstrated for MIPs using uncooled LGADs operated in air at COSY in Juelich. The results were published in The European Physics Journal A with the title "Low Gain Avalanche Detectors for the HADES reaction time (T0) detector upgrade" (2020), see [6]. However, the result could not be reproduced in an experiment at SIS18 in Darmstadt, where 2.5 GeV protons at a higher beam intensity were used. At SIS18 a timing precision of $\sigma_t \approx 63.3$ ps was reached. In both experiments the timing precisions reached with PaDiWa3 discriminators, $\sigma_t \approx 66.8$ ps $\sigma_t \approx 77.4$ ps at COSY and SIS18 respectively, were significantly worse than the precisions reached with NINO discriminators. An AC-coupled LGAD, tested at SIS18, reached a timing precision of about $\sigma_t \approx 171$ ps, therefore more research is needed in order to reach a timing precision comparable to the demonstrated DC-coupled LGADs.

In order to improve the reached timing resolution using PaDiWa discriminators, modifications on PaDiWa3 and PaDiWa4 boards were made and investigated. However, non of the made modifications improved the timing resolution, instead it got worse.

It could be shown that the LGAD technology is a promising candidate to replace the diamond based Start detector currently used in HADES. In fact, it is planned to use an LGAD based T_0 detector in an upcoming experiment in 2021 with 4.5 GeV protons with an intensity of $7.5 \cdot 10^7$ p/s. It is foreseen to use a $2 \times 2 \text{cm}^2$ big sensor with two rows of 46 strips and, in order to have an improved radiation hardness, a carbon co-implanted gain layer. PaDiWa3 boards without further modifications will be used to read out the LGADs

New LGADs are available and will be exposed to heavy ion beam in order to study their radiation hardness. In case of a sufficient radiation hardness, it is foreseen to use LGADs for beam monitoring purposes, as a part of a fast beam abort system and as a T_0 detector (for moderate beam intensities) at the future CBM experiment at FAIR.

Acknowledgements

Bibliography

[1] G. Agakichiev et al. "The high-acceptance dielectron spectrometer HADES". In: *The European Physical Journal A* 41.2 (2009). ISSN: 1434-6001. DOI: 10.1140/epja/i2009-10807-5.

[2] Tetyana Galatyuk. "Recent Results from HADES". In: *Proceedings of 13th International Conference on Nucleus-Nucleus Collisions*. DOI: 10.7566/JPSCP.32.010079. eprint: https://journals.jps.jp/doi/pdf/10.7566/JPSCP.32.010079. URL: https://journals.jps.jp/doi/abs/10.7566/JPSCP.32.010079.

[3] J. Adamczewski-Musch et al. "Probing dense baryon-rich matter with virtual photons". In: *Nature Physics* 15.10 (2019), pp. 1040–1045. ISSN: 1745-2473. DOI: 10.1038/s41567-019-0583-8.

[4] P. Salabura. "Studying Baryonic Matter with HADES at GSI/FAIR". In: *Acta Physica Polonica B* 50.6 (2019), p. 1205. ISSN: 0587-4254. DOI: 10.5506/APhysPolB.50.1205.

[5] Tetyana Galatyuk. "HADES overview". In: *Nuclear Physics A* 931 (2014), pp. 41–51. ISSN: 03759474. DOI: 10.1016/j.nuclphysa.2014.10.044.

[6] J. Pietraszko et al. "Low Gain Avalanche Detectors for the HADES reaction time (T_0) detector upgrade". In: *The European Physical Journal A* 56.7 (2020). ISSN: 1434-6001. DOI: 10.1140/epja/s10050-020-00186-w.

[7] Adrian Rost et al., eds. *Beam Quality Monitoring System in the HADES Experiment at GSI Using CVD Diamond Material: JACoW Publishing, Geneva, Switzerland*. 2019. DOI: 10.18429/JACOW-IBIC2018-TUPC03.

[8] Adrian Rost et al., eds. *Performance of the CVD Diamond Based Beam Quality Monitoring System in the HADES Experiment at GSI*: JACoW Publishing, Geneva, Switzerland*. 2019. DOI: 10.18429/JACOW-IPAC2019-WEPGW019.

[9] Tetyana Galatyuk et al. "Tests of the Electromagnetic Calorimeter for HADES Experiment at GSI". In: *KnE Energy* 3 (Apr. 2018), p. 162. DOI: 10.18502/ken.v3i1.1739.

[10] J. Pietraszko et al. "Diamonds as timing detectors for minimum-ionizing particles: The HADES proton-beam monitor and START signal detectors for time of flight measurements". In: *Nuclear Instruments and Methods in Physics Research Section A: Accelerators, Spectrometers, Detectors and Associated Equipment* 618.1-3 (2010), pp. 121–123. ISSN: 01689002. DOI: 10.1016/j.nima.2010.02.113.

[11] J. Pietraszko et al. "Radiation damage in single crystal CVD diamond material investigated with a high current relativistic 197Au beam". In: *Nuclear Instruments and Methods in Physics Research Section A: Accelerators, Spectrometers, Detectors and Associated Equipment* 763 (2014), pp. 1–5. ISSN: 01689002. DOI: `10.1016/j.nima.2014.06.006`.

[12] Adrian Rost. "Design, installation and commissioning of new read-out electronics for HADES ECAL and diamond detectors for T0-reconstruction and beam diagnostics". PhD thesis. Darmstadt: Technische Universität Darmstadt, 2020. URL: `http://tuprints.ulb.tu-darmstadt.de/12235/`.

[13] K. Zeitelhack et al. "The HADES RICH detector". In: *Nuclear Instruments and Methods in Physics Research Section A: Accelerators, Spectrometers, Detectors and Associated Equipment* 433.1 (1999), pp. 201–206. ISSN: 0168-9002. DOI: `https://doi.org/10.1016/S0168-9002(99)00371-X`. URL: `http://www.sciencedirect.com/science/article/pii/S016890029900371X`.

[14] C. Pauly et al. "Upgrade of the HADES RICH photon detector with H12700 MAPMTs". In: *Nuclear Instruments and Methods in Physics Research Section A: Accelerators, Spectrometers, Detectors and Associated Equipment* 876 (2017). The 9th international workshop on Ring Imaging Cherenkov Detectors (RICH2016), pp. 164–167. ISSN: 0168-9002. DOI: `https://doi.org/10.1016/j.nima.2017.02.067`. URL: `http://www.sciencedirect.com/science/article/pii/S0168900217302632`.

[15] C. Müntz et al. "The HADES tracking system". In: *Nuclear Instruments and Methods in Physics Research Section A: Accelerators, Spectrometers, Detectors and Associated Equipment* 535.1-2 (2004), pp. 242–246. ISSN: 01689002. DOI: `10.1016/j.nima.2004.07.232`.

[16] Michael Wiebusch. "Towards new front-end electronics for the HADES drift chamber system". PhD thesis. 2019.

[17] Timo Scheib. "Λ and K0s production in Au+Au collisions at 1.23A GeV". Dissertation, JWGU Frankfurt, 2017. Dissertation. Frankfurt am Main: JWGU Frankfurt, 2017. URL: `https://repository.gsi.de/record/209923`.

[18] D. Belver et al. "The HADES RPC inner TOF wall". In: *Nuclear Instruments and Methods in Physics Research Section A: Accelerators, Spectrometers, Detectors and Associated Equipment* 602.3 (2009), pp. 687–690. ISSN: 01689002. DOI: `10.1016/j.nima.2008.12.090`.

[19] Georgy Kornakov Van. "New advances and developments on the RPC tof wall of the HADES experiment at GSI". PhD thesis. 2012. URL: `http://hdl.handle.net/10347/7281`.

[20] Christian Lippmann. "Detector Physics of Resistive Plate Chambers". PhD thesis. Frankfurt U., 2003, pp. 23–24.

[21] C. Agodi et al. "The time of flight wall for the HADES spectrometer". In: *IEEE Transactions on Nuclear Science* 45.3 (1998), pp. 665–669. ISSN: 0018-9499. DOI: `10.1109/23.682606`.

[22] O. Svoboda et al. "Electromagnetic calorimeter for the HADES@FAIR experiment". In: *Journal of Instrumentation* 9.05 (2014), pp. C05002–C05002. ISSN: 1748-0221. DOI: `10.1088/1748-0221/9/05/C05002`.

[23] M. Akrawy et al. "Development studies for the OPAL end cap electromagnetic calorimeter using vacuum photo triode instrumented leadglass". In: *Nuclear Instruments and Methods in Physics Research Section A: Accelerators, Spectrometers, Detectors and Associated Equipment* 290.1 (1990), pp. 76–94. ISSN: 0168-9002. DOI: `https://doi.org/10.1016/0168-9002(90)90346-8`. URL: `http://www.sciencedirect.com/science/article/pii/0168900290903468`.

[24] Frank Hartmann. *Evolution of Silicon Sensor Technology in Particle Physics*. Vol. 275. Cham: Springer International Publishing, 2017. ISBN: 978-3-319-64434-9. DOI: `10.1007/978-3-319-64436-3`.

[25] S. M. Sze and Kwok K. Ng. *Physics of semiconductor devices*. 3. ed. Hoboken, NJ: Wiley-Interscience, 2007. ISBN: 9780471143239. DOI: `10.1002/0470068329`. URL: `http://search.ebscohost.com/login.aspx?direct=true&scope=site&db=nlebk&db=nlabk&AN=172575`.

[26] Gerhard Lutz. *Semiconductor Radiation Detectors*. Berlin, Heidelberg: Springer Berlin Heidelberg, 2007. ISBN: 978-3-540-71678-5. DOI: `10.1007/978-3-540-71679-2`.

[27] Matteo Centis Vignali. "Silicon Sensors for the Upgrades of the CMS Pixel Detector". PhD thesis. Hamburg: Hamburg U., 2015. DOI: `10.3204/DESY-THESIS-2015-052`.

[28] M. Tanabashi et al. "Review of Particle Physics". In: *Physical Review D* 98.3 (2018). ISSN: 2470-0010. DOI: `10.1103/PhysRevD.98.030001`.

[29] N. Cartiglia et al. "Beam test results of a 16 ps timing system based on ultra-fast silicon detectors". In: *Nuclear Instruments and Methods in Physics Research Section A: Accelerators, Spectrometers, Detectors and Associated Equipment* 850 (2017), pp. 83–88. ISSN: 01689002. DOI: `10.1016/j.nima.2017.01.021`.

[30] S. M. Mazza et al. "Properties of FBK UFSDs after neutron and proton irradiation up to $6 \cdot 10^{15}$ n_{eq}/cm^2". In: *Journal of Instrumentation* 15.04 (2020), T04008–T04008. ISSN: 1748-0221. DOI: `10.1088/1748-0221/15/04/T04008`.

[31] N. Cartiglia et al. "Design optimization of ultra-fast silicon detectors". In: *Nuclear Instruments and Methods in Physics Research Section A: Accelerators, Spectrometers, Detectors and Associated Equipment* 796 (2015), pp. 141–148. ISSN: 01689002. DOI: `10.1016/j.nima.2015.04.025`.

[32] V. Sola et al. "Ultra-Fast Silicon Detectors for 4D tracking". In: *Journal of Instrumentation* 12.02 (2017), pp. C02072–C02072. ISSN: 1748-0221. DOI: `10.1088/1748-0221/12/02/C02072`.

[33] Hartmut F-W Sadrozinski, Abraham Seiden, and Nicolò Cartiglia. "4D tracking with ultra-fast silicon detectors". In: *Reports on Progress in Physics* 81.2 (2018), p. 026101. ISSN: 0034-4885. DOI: `10.1088/1361-6633/aa94d3`.

[34] C. Gallrapp et al. "Study of gain homogeneity and radiation effects of Low Gain Avalanche Pad Detectors". In: *Nuclear Instruments and Methods in Physics Research Section A: Accelerators, Spectrometers, Detectors and Associated Equipment* 875 (2017), pp. 27–34. ISSN: 01689002. DOI: `10.1016/j.nima.2017.07.038`.

[35] M. Mandurrino et al. "Analysis and numerical design of Resistive AC-Coupled Silicon Detectors (RSD) for 4D particle tracking". In: *Nuclear Instruments and Methods in Physics Research Section A: Accelerators, Spectrometers, Detectors and Associated Equipment* 959 (2020), p. 163479. ISSN: 01689002. DOI: 10.1016/j.nima.2020.163479.

[36] Francesca Cenna et al. "Weightfield2: A fast simulator for silicon and diamond solid state detector". In: *Nuclear Instruments and Methods in Physics Research Section A: Accelerators, Spectrometers, Detectors and Associated Equipment* 796 (2015), pp. 149–153. ISSN: 01689002. DOI: 10.1016/j.nima.2015.04.015.

[37] V. Sola et al. "First FBK production of 50 μm ultra-fast silicon detectors". In: *Nuclear Instruments and Methods in Physics Research Section A: Accelerators, Spectrometers, Detectors and Associated Equipment* 924 (2019), pp. 360–368. ISSN: 01689002. DOI: 10.1016/j.nima.2018.07.060.

[38] Marco Mandurrino et al. "Demonstration of 200-, 100-, and 50-μ m Pitch Resistive AC-Coupled Silicon Detectors (RSD) With 100% Fill-Factor for 4D Particle Tracking". In: *IEEE Electron Device Letters* 40.11 (2019), pp. 1780–1783. ISSN: 0741-3106. DOI: 10.1109/LED.2019.2943242.

[39] N. Cartiglia et al. "Performance of ultra-fast silicon detectors". In: *Journal of Instrumentation* 9.02 (2014), pp. C02001–C02001. ISSN: 1748-0221. DOI: 10.1088/1748-0221/9/02/C02001.

[40] Zhong He. "Review of the Shockley–Ramo theorem and its application in semiconductor gamma-ray detectors". In: *Nuclear Instruments and Methods in Physics Research Section A: Accelerators, Spectrometers, Detectors and Associated Equipment* 463.1 (2001), pp. 250–267. ISSN: 0168-9002. DOI: https://doi.org/10.1016/S0168-9002(01)00223-6. URL: http://www.sciencedirect.com/science/article/pii/S0168900201002236.

[41] N. Cartiglia et al. "Tracking in 4 dimensions". In: *Nuclear Instruments and Methods in Physics Research Section A: Accelerators, Spectrometers, Detectors and Associated Equipment* 845 (2017), pp. 47–51. ISSN: 01689002. DOI: 10.1016/j.nima.2016.05.078.

[42] S. Meroli, D. Passeri, and L. Servoli. "Energy loss measurement for charged particles in very thin silicon layers". In: *Journal of Instrumentation* 6.06 (2011), P06013–P06013. ISSN: 1748-0221. DOI: 10.1088/1748-0221/6/06/P06013.

[43] R. J. McIntyre. "Multiplication noise in uniform avalanche diodes". In: *IEEE Transactions on Electron Devices* ED-13.1 (1966), pp. 164–168. ISSN: 0018-9383. DOI: 10.1109/T-ED.1966.15651.

[44] Md. Mottaleb Hossain, John P. R. David, and Majeed M. Hayat. "Exact Analytical Formula for the Excess Noise Factor for Mixed Carrier Injection Avalanche Photodiodes". In: *Journal of Lightwave Technology* 37.13 (2019), pp. 3315–3323. ISSN: 0733-8724. DOI: 10.1109/JLT.2019.2914443.

[45] Hamamatsu Photonics. "Characteristics and use of Si APD". In: *Technical Information* SD-28 (2004).

[46] M. Moll. "Radiation Damage to Silicon Sensors". In: *AIDA2020* (2016). URL: `https://indico.cern.ch/event/468478/contributions/2135148/attachments/1290271/1921271/1600613-RD50-AIDA2020.pdf`.

[47] M. Mandurrino, N. Cartiglia, A. Staiano, R. Arcidiacono, M. M. Obertino, M. Ferrero, F. Cenna, V. Sola, M. Boscardin, G. Paternoster, F. Ficorella, L. Pancheri and G. F. Dalla Betta. *Numerical Simulation of Charge Multiplication in Ultra-Fast Silicon Detectors (UFSD) and Comparison with Experimental Data: Conference proceedings*. Piscataway, NJ: IEEE, 2017. ISBN: 9781538622834. URL: `http://ieeexplore.ieee.org/servlet/opac?punumber=8508871`.

[48] M. Ferrero a, R. Arcidiacono a,b, M. Barozzi c,e, M. Boscardin c,e, N. Cartiglia a,∗, G.F. Dalla Betta d,e, Z. Galloway g, M. Mandurrino a, S. Mazza g, G. Paternoster c,e, F. Ficorella c,e, L. Pancheri d,e, H-F W. Sadrozinski g, F. Siviero a,f, V. Sola a,f, A. Staiano a, A. Seiden g, M. Tornago a,f, Y. Zhao g. "Radiation resistant LGAD design". In: (2019).

[49] G. Kramberger et al. "Radiation hardness of thin Low Gain Avalanche Detectors". In: *Nuclear Instruments and Methods in Physics Research Section A: Accelerators, Spectrometers, Detectors and Associated Equipment* 891 (2018), pp. 68–77. ISSN: 01689002. DOI: `10.1016/j.nima.2018.02.018`.

[50] G. Kramberger et al. "Radiation effects in Low Gain Avalanche Detectors after hadron irradiations". In: *Journal of Instrumentation* 10.07 (2015), P07006–P07006. ISSN: 1748-0221. DOI: `10.1088/1748-0221/10/07/P07006`.

[51] M. Moll, E. Fretwurst, and G. Lindström. "Leakage current of hadron irradiated silicon detectors – material dependence". In: *Nuclear Instruments and Methods in Physics Research Section A: Accelerators, Spectrometers, Detectors and Associated Equipment* 426.1 (1999), pp. 87–93. ISSN: 0168-9002. DOI: `https://doi.org/10.1016/S0168-9002(98)01475-2`. URL: `http://www.sciencedirect.com/science/article/pii/S0168900298014752`.

[52] G. Kramberger et al. "Radiation hardness of gallium doped low gain avalanche detectors". In: *Nuclear Instruments and Methods in Physics Research Section A: Accelerators, Spectrometers, Detectors and Associated Equipment* 898 (2018), pp. 53–59. ISSN: 01689002. DOI: `10.1016/j.nima.2018.04.060`.

[53] R. Padilla et al. *Effect of deep gain layer and Carbon infusion on LGAD radiation hardness*. URL: `http://arxiv.org/pdf/2004.05260v4`.

[54] Z. Galloway et al. "Properties of HPK UFSD after neutron irradiation up to 6e15 n/cm 2". In: *Nuclear Instruments and Methods in Physics Research Section A: Accelerators, Spectrometers, Detectors and Associated Equipment* 940 (2019), pp. 19–29. ISSN: 01689002. DOI: `10.1016/j.nima.2019.05.017`.

[55] J. Adamczewski-Musch, H. G. Essel, and S. Linev. "Online Object Monitoring With Go4 V4.4". In: *IEEE Transactions on Nuclear Science* 58.4 (2011), pp. 1477–1481. DOI: `10.1109/TNS.2011.2149541`.

[56] R. Brun and F. Rademakers. "ROOT: An object oriented data analysis framework". In: *Nucl. Instrum. Meth. A* 389 (1997). Ed. by M. Werlen and D. Perret-Gallix, pp. 81–86. DOI: `10.1016/S0168-9002(97)00048-X`.

[57] Marie Andrä et al. "Development of low-energy X-ray detectors using LGAD sensors". In: *Journal of Synchrotron Radiation* 26.Pt 4 (2019), pp. 1226–1237. DOI: `10.1107/S1600577519005393`.

[58] F. Anghinolfi et al. "NINO: an ultra-fast and low-power front-end amplifier/discriminator ASIC designed for the multigap resistive plate chamber". In: *Nuclear Instruments and Methods in Physics Research Section A: Accelerators, Spectrometers, Detectors and Associated Equipment* 533.1-2 (2004), pp. 183–187. ISSN: 01689002. DOI: `10.1016/j.nima.2004.07.024`.

[59] GSI Helmholtzzentrum für Schwerionenforschung GmbH. *TRB3 web page @ONLINE*. 2020. URL: `http://trb.gsi.de/`.

[60] A. Neiser et al. "TRB3: a 264 channel high precision TDC platform and its applications". In: *Journal of Instrumentation* 8.12 (2013), pp. C12043–C12043. ISSN: 1748-0221. DOI: `10.1088/1748-0221/8/12/C12043`.

[61] F. Gonnella, V. Kozhuharov, and M. Raggi. "Time over threshold in the presence of noise". In: *Nuclear Instruments and Methods in Physics Research Section A: Accelerators, Spectrometers, Detectors and Associated Equipment* 791 (2015), pp. 16–21. ISSN: 01689002. DOI: `10.1016/j.nima.2015.04.028`.

List of Figures

List of Tables